SYNTHESIS AND CHARACTERIZATION OF INORGANIC NANOSTRUCTURED MATERIALS FOR ADVANCED ENERGY STORAGE

Author: Jin Xie

Persistent link: http://hdl.handle.net/2345/bc-ir:104493

This work is posted on eScholarship@BC,
Boston College University Libraries.

Boston College Electronic Thesis or Dissertation, 2015

Copyright is held by the author, with all rights reserved, unless otherwise noted.

Boston College

The Graduate School of Arts and Sciences

Department of Chemistry

SYNTHESIS AND CHARACTERIZATION OF INORGANIC NANOSTRUCTURED MATERIALS FOR ADVANCED ENERGY STORAGE

a dissertation

by

JIN XIE

submitted in partial fulfillment of the requirements

for the degree of

Doctor of Philosophy

August 2015

© copyright by JIN XIE

2015

Abstract

SYNTHESIS AND CHARACTERIZATION OF

INORGANIC NANOSTRUCTURED MATERIALS

FOR ADVANCED ENERGY STORAGE

A Dissertation by Jin Xie

Dissertation Advisor: Prof. Dunwei Wang

The performance of advanced energy storage devices is intimately connected to the designs of electrodes. To enable significant developments in this research field, we need detailed information and knowledge about how the functions and performances of the electrodes depend on their chemical compositions, dimensions, morphologies, and surface properties. This thesis presents my successes in synthesizing and characterizing electrode materials for advanced electrochemical energy storage devices, with much attention given to understanding the operation and fading mechanism of battery electrodes, as well as methods to improve their performances and stabilities.

This dissertation is presented within the framework of two energy storage technologies: lithium ion batteries and lithium oxygen batteries. The energy density of lithium ion batteries is determined by the density of electrode materials and their lithium storage capabilities. To improve the overall energy densities of lithium ion batteries, silicon has

been proposed to replace lithium intercalation compounds in the battery anodes. However, with a ~400% volume expansion upon fully lithiation, silicon-based anodes face serious capacity degradation in battery operation. To overcome this challenge, heteronanostructure-based Si/$TiSi_2$ were designed and synthesized as anode materials for lithium ion batteries with long cycling life. The performance and morphology relationship was also carefully studied through comparing one-dimensional and two-dimensional heteronanostructure-based silicon anodes.

Lithium oxygen batteries, on the other hand, are devices based on lithium conversion chemistries and they offer higher energy densities compared to lithium ion batteries. However, existing carbon based electrodes in lithium oxygen batteries only allow for battery operation with limited capacity, poor stability and low round-trip efficiency. The degradation of electrolytes and carbon electrodes have been found to both contribute to the challenges. The understanding of the synergistic effect between electrolyte decomposition and electrode decomposition, nevertheless, is conspicuously lacking. To better understand the reaction chemistries in lithium oxygen batteries, I designed, synthesized, and studied heteronanostructure-based carbon-free inorganic electrodes, as well as carbon electrodes whose surfaces protected by metal oxide thin films. The new types of electrodes prove to be highly effective in minimizing parasitic reactions, reducing operation overpotentials and boosting battery lifetimes. The improved stability and well-defined electrode morphology also enabled detailed studies on the formation and decomposition of Li_2O_2.

To summarize, this dissertation presented the synthesis and characterization of inorganic nanostructured materials for advanced energy storage. On a practical level, the new types of materials allow for the immediate advancement of the energy storage technology. On a fundamental level, it helped to better understand reaction chemistries and fading mechanisms of battery electrodes.

Table of Contents

Chapter 1 Introduction 1

1.1 Electrochemical Energy Storage 1

1.2 Lithium Ion Batteries 4

1.3 Lithium Oxygen Batteries 6

1.4 References 11

Chapter 2 High Capacity Si/$TiSi_2$ Lithium Battery Anode 15

2.1 Growth Mechanism of $TiSi_2$ Nanostructures 15

2.1.1 Experimental Details 17

2.1.2 Results and Discussion 18

2.1.3 Conclusions 26

2.2 Si/$TiSi_2$ Heteronanostructure Anode for Lithium Ion Batteries 27

2.2.1 Experimental Details 29

2.2.2 Results and Discussion 30

2.2.3 Conclusions 40

2.3 References 40

Chapter 3 Synthesis of Pt/$TiSi_2$ Heteronanostructures 47

3.1 Experimental Details 47

3.2 Results and Discussion 50

3.3 Supplementary Information 62

3.4 Conclusions 64

3.5 References 64

Chapter 4 Ru/$TiSi_2$: A Non-carbon Electrode for Lithium Oxygen Batteries 69

4.1 Experimental Details 69

4.2 Results and Discussions 74

4.3 Supplementary Information 83

4.4 Conclusions 90

4.5 References 91

Chapter 5 Protected 3DOm Carbon for Lithium Oxygen Batteries 96

5.1 Experimental Details 96

5.2 Results and Discussions 100

5.3 Supplementary Information 108

5.4 Conclusions 120

5.5 References 120

Acknowledgements

I want to express my deepest appreciation to all my family and friends to make my journey at Boston College wonderful and memorable.

First of all, I would like to thank my advisor, Prof. Dunwei Wang, whose dedication to pursue scientific research has been really inspiring. I am indebted to him for his support, patience, guidance, challenges and understanding in the past six years. His passion for science and hardworking attitude have really changed me and made me realize how much I want to pursue a career in scientific research, as he does.

I would like to thank my committee advisor, Prof. Frank Tsung, for being a teacher and a friend. Thanks for being supportive for the DEMS experiment and encouraging me to keep doing research in academia. Thank Prof. Udayan Mohanty for being my defense committee member, who helped me tremendously throughout my graduate research and postdoc searching. Thank Prof. Paul Davidovits for reading and helping me in writing this dissertation. Being the teaching assistant for you in the general chemistry class thought me how to become a good teacher.

I would like to acknowledge Prof. Yang Shao-Horn, Prof. Wei Fan, Prof Frank Tsung, Prof. De-en Jiang and members in their groups for all the help in our collaborative projects. I also thank Harvard CNS and MIT CMSE for providing shared facilities.

Thanks to Steve Shepard and Dr. Greg McMahon in Boston College cleanroom, and Dr. Dezhi Wang, Richard Pijar and Paul Dee for their continuous technical support. And thank all the staff in the chemistry department for keeping Merkert running and keeping us safe.

I want to thank all the Wang lab members over the years: especially Dr. Sa Zhou and Dr. Xiaogang Yang, from whom I learned so much; Xiahui Yao, Qingmei Cheng, Qi Dong and Ian Madden, who made great contributions to move the lithium oxygen battery project forward; James Thorne, who helped me read and correct my thesis; Dr. Rui Liu, Dr. Pengcheng Dai, Dr. Yongjing Lin, Dr. Guangbi Yuan, Dr. Matthew Mayer, Dr. Xiaohua Liu, Dr. Ji-Wook Jang, Zachary Simpson, Stafford Sheehan and Yumin He, for their help and insightful discussions. To all past and current group members, I am so happy to be a member of our big family.

Thanks to all my friends I met here in the wonderful city of Boston and all my old friends for their support and friendship. Thank Anna Shan, Donny Wang, and Crystal Zhuang for igniting my passion of life. To my dearest friends and partners at Neostellen: Yue Zhao, Dr. Qingyi Yu, Dr. Zhao Qin and Max Meng, thank you for your warm help in my darkest time and let us hope the best for Neostellen. I would like to thank Dr. Hong Zheng, Hao Wu, Dr. Zhiyong Yu, Dr. Tianyi Sun, Yani Zhou, Angel Chen and Youyou Yu for the great time we have spent together. In particular, many thanks go to my old fiends Dr. Zhongwei Zhu, Dr. Jia Liu, Dr. Chong Liu, Chun Cao and Qimin Gu for their constant help and encouragement.

I owe my deepest thanks to my family, especially my parents. I would be nothing without your love and help. I feel so sorry that I couldn’t be with you as much as I should be. Thanks for loving me and always be there for me.

Dedication

The author wishes to dedicate this dissertation to his parents and grandparents

List of Publications:

(1) **Xie, J.**; Yao, X.; Cheng, Q.; Madden, I. P.; Dornath, P.; Chang, C.-C.; Fan, W.; Wang, D. Three Dimensionally Ordered Mesoporous Carbon as a Stable, High-Performance Li-O_2 Battery Cathode. *Angew. Chem. Int. Ed.* **2015**, *127*, 4373-4377.

(2) **Xie, J.**; Yao, X.; Madden, I. P.; Jiang, D.-E.; Chou, L.-Y.; Tsung, C.-K.; Wang, D. Selective Deposition of Ru Nanoparticles on $TiSi_2$ Nanonet and Its Utilization for Li_2O_2 Formation and Decomposition. *J. Am. Chem. Soc.* **2014**, *136*, 8903-8906.

(3) Dai, P. C.; Li, W.; **Xie, J.**; He, Y. M.; Thorne, J.; McMahon, G.; Zhan, J. H.; Wang, D. W. Forming Buried Junctions to Enhance the Photovoltage Generated by Cuprous Oxide in Aqueous Solutions. *Angew. Chem. Int. Ed.* **2014**, *53*, 13493-13497.

(4) Zhou, S.; Yang, X.; **Xie, J.**; Simpson, Z. I.; Wang, D. Titanium Silicide Nanonet as a New Material Platform for Advanced Lithium-Ion Battery Applications. *Chem. Commun.* **2013**, *49*, 6470-6476.

(5) Yang, X. G.; Du, C.; Liu, R.; **Xie, J.**; Wang, D. W. Balancing Photovoltage Generation and Charge-Transfer Enhancement for Catalyst-Decorated Photoelectrochemical Water Splitting: A Case Study of the Hematite/MnO_x Combination. *J. Catal.* **2013**, *304*, 86-91.

(6) **Xie, J.**; Yang, X.; Han, B.; Shao-Horn, Y.; Wang, D. Site-Selective Deposition of Twinned Platinum Nanoparticles on $TiSi_2$ Nanonets by Atomic Layer Deposition and Their Oxygen Reduction Activities. *ACS Nano* **2013**, *7*, 6337-6345.

(7) Du, C.; Yang, X.; Mayer, M. T.; Hoyt, H.; **Xie, J.**; McMahon, G.; Bischoping, G.; Wang, D. Hematite-Based Water Splitting with Low Turn-On Voltages. *Angew. Chem. Int. Ed.* **2013**, *52*, 12692-12695.

(8) Dai, P. C.; **Xie, J.**; Mayer, M. T.; Yang, X. G.; Zhan, J. H.; Wang, D. W. Solar Hydrogen Generation by Silicon Nanowires Modified with Platinum Nanoparticle Catalysts by Atomic Layer Deposition. *Angew. Chem. Int. Ed.* **2013**, *52*, 11119-11123.

(9) Zhou, S.; Yang, X. G.; Lin, Y. J.; **Xie, J.**; Wang, D. W. A Nanonet-Enabled Li Ion Battery Cathode Material with High Power Rate, High Capacity, and Long Cycle Lifetime. *ACS Nano* **2012**, *6*, 919-924.

(10) Zhou, S.; **Xie, J.**; Wang, D. W. Understanding the Growth Mechanism of Titanium Disilicide Nanonets. *ACS Nano* **2011**, *5*, 4205-4210.

(11) Yuan, G.; Aruda, K.; Zhou, S.; Levine, A.; **Xie, J.**; Wang, D. Understanding the Origin of the Low Performance of Chemically Grown Silicon Nanowires for Solar Energy Conversion. *Angew. Chem. Int. Ed.* **2011**, *50*, 2334-2338.

(12) **Xie, J.**; Yang, X. G.; Zhou, S.; Wang, D. W. Comparing One- and Two-Dimensional Heteronanostructures As Silicon-Based Lithium Ion Battery Anode Materials. *ACS Nano* **2011**, *5*, 9225-9231.

(13) Levine, A.; Yuan, G. B.; **Xie, J.**; Wang, D. W. Preparations and Energetic Applications of Si Nanowires. *Science of Advanced Materials* **2010**, *2*, 463-473.

Chapter 1 Introduction

1.1 Electrochemical Energy Storage

By definition, electrochemical energy storage (EES) devices are systems which can convert stored chemical energy into electrical energy. Three major types of EES devices are batteries, fuel cells and electrochemical capacitors.[1]

Figure 1.1a shows the basic operation mechanism of the battery system. Batteries can be categorized into primary batteries and secondary batteries. In a primary battery, electrical energy is generated by conversion of chemical energy via redox reactions at both anode and cathode. In a secondary battery, redox reactions at both anode and cathode can proceed in either direction. Electrical energy can be stored as chemical energy during charging and then released during discharging.

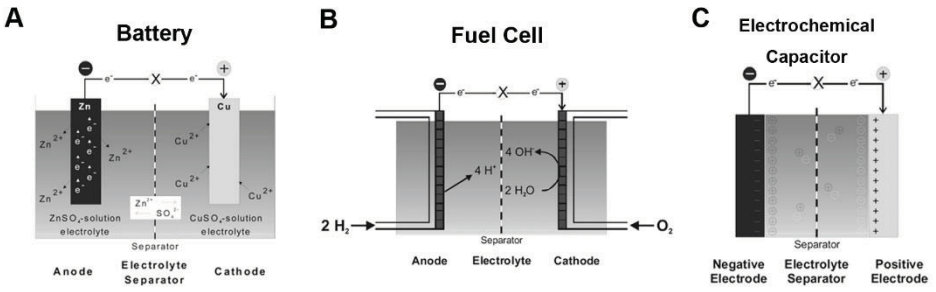

(**Figure 1.1** Operation mechanisms of batteries, fuel cells and electrochemical capacitors. [Ref 1] - Reproduced by permission of ACS)

Figure 1.1b shows the basic operation mechanism of fuel cells. In contrast to batteries' close systems, fuel cells are open systems where both electrodes are just charge transfer media and active materials undergoing the redox reactions are delivered from outside.

Figure 1.1c shows the basic operation mechanism of electrochemical capacitors. In electrochemical capacitors, charges are often stored and released at the interface of electrode and electrolyte, the so called electrical double layers. Electrochemical capacitors are also called supercapacitors.

The performance of EES can be characterized by several key parameters[2]:

- Specific capacity (C, mAh/g): $C=\int_0^t Idt/m$
- Coulombic efficiency (η, %): $\eta=\frac{C_{discharge}}{C_{charge}}$
- Cycle life: It presents the number of cycles that a battery maintains certain percentage of its initial capacity during cycling process.
- Specific Energy density (Em, Wh/kg): $E_m=\int_0^t IVdt/m$
- Specific Power density (Pm, W/kg): $P_m=IV/m$

Among them, two most important key characteristics of EES devices including energy density and power density are plotted as Ragone plots in Figure 1.2.

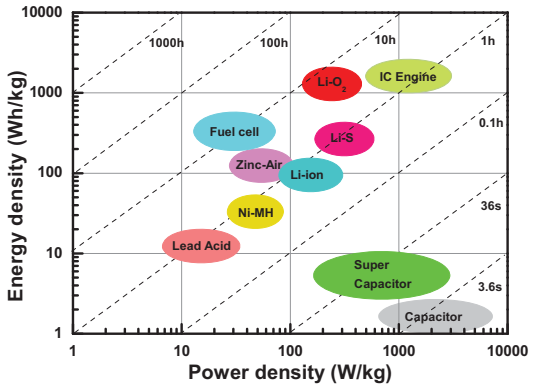

(**Figure 1.2** Ragone plots of batteries, fuel cells, electrochemical capacitors and internal combustion engines)

Societal needs for electrical energy storage at many levels, from portable electronics to electrical plug-in vehicles[3] and grid-scale applications[4], are growing at a fast pace. As the requirements for energy densities, power rates, and safety concerns, among other things, vary widely depending on the applications, and many available options have been pursued simultaneously. One of the promising routes is to replace the existing intercalation chemistry based lithium ion batteries with the conversion chemistry based advanced lithium batteries.

In this dissertation, I will focus my discussion on two types of devices. The first one is advanced lithium ion battery with Silicon conversion anode. The second one is a lithium oxygen battery with Oxygen conversion cathode. Despite the apparent differences in their chemistries and engineering designs, the development of these technologies depends on advances in materials research. This study will illustrate how the performance of an energy storage device is closely connected to surface properties and materials designs of the electrode.

1.2 Lithium Ion Batteries

Lithium ion batteries have been under consistent researching and development for the past a few decades.[1, 2, 5] Many of today's real world applications are powered by lithium ion batteries, including but not limited to consumer electronics and electric vehicles. The operation of commercial lithium ion batteries is based on the intercalation chemistry.[5] Its operation mechanism is illustrated in Figure 1.3. It is composed of a graphite anode (also called negative electrode), a non-aqueous liquid electrolyte and a $LiCoO_2$ cathode (also called positive electrode). On charging, Li^+ are transported from $LiCoO_2$ to graphite, and back in discharging. Due to the difference of chemical energy at the anode and cathode, energy can be converted in between the form of chemical energy and electrical energy.

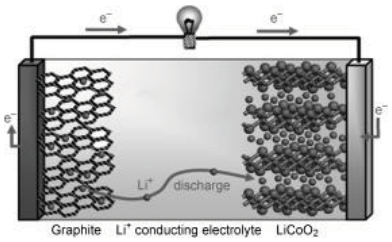

(**Figure 1.3** Operation mechanism of a commercial lithium ion battery. [Ref 5] - Reproduced by permission of WILEY-VCH)

Different applications require batteries with different characteristics. In general, batteries with high capacity, high energy density, high power density, close to 100% Coulombic efficiency and long cycle life are desired. Due to the complexity of battery design, all these above mentioned parameters are dependent on each single component of the battery. For instance, the capacity of the battery is determined by both electrodes (anode and cathode) and other cell components (electrolyte, membrane and package etc.). The overall cell capacity can be understood as the following equation:

$\frac{1}{C}=\frac{1}{C_a}+\frac{1}{C_c}+\frac{1}{C_m}$, where C_a and C_c are the capacity of anode and the capacity cathode respectively. The capacities of electrodes (C_a and C_c) are determined by the nature of the active materials in the electrodes and their abilities to accommodate Li ions. $1/C_m$ is the contribution from other cell components, which is often neglected due to its small contribution to the overall capacity.

Active materials in commercial electrodes, such as $LiCoO_2$ and graphite, have layered crystal structures to store Li ions. Although such a storage mechanism offers high stability to enable cells stable for hundreds of cycles, it suffers from low theoretical capacity. To achieve higher capacity, lithium storage materials based on a conversion chemistry have been purposed to replace lithium intercalation compounds. Taking silicon as an example, one Si atom could react with 4.4 Li ions when fully converted, offering a theoretical capacity as high as 4200 mAh/g (vs. 372 mAh/g, theoretical capacity of graphite). However, unlike the lithium intercalation compounds, the stability of silicon remains a challenge because of its ~400% volume expansion when fully converted.[6]

This dissertation is focused on how the performances of silicon based anodes are connected to their electrode design at nanoscale. With the concept of heteronanostructure (e.g. $Si/TiSi_2$) design, significant improvements has been achieved in advanced lithium ion battery applications.

1.3 Lithium Oxygen Batteries

The technology of lithium oxygen batteries has attracted intense research activities in the past several years owing to its high theoretical energy density.[7] The operation mechanism of lithium oxygen battery is shown in Figure 1.4. They are hybrids of lithium batteries and fuel cells. The reversible conversion between O_2 and Li_2O_2 in an aprotic solution ($2Li^+ + O_2 + 2e^- \leftrightarrow Li_2O_2$, E_0=2.96 V vs. Li^+/Li) is the chemical basis for Li-O_2 batteries.[8] In principle, O_2 can be directly drawn from and disposed into air and, as such, the theoretical capacity can comparable to gasoline, if one only considers Li anode as the active component (Figure 1.4). In practice, the mass of Li_2O_2, the supporting electrode (as well as catalysts used on the cathode), and electrolyte must be taken into account when calculating the specific energy. Even by the more conservative estimate, Li-O_2 batteries are of 2-3 times higher specific energy density (>2,000 Wh/kg) than Li-ion batteries,[7] which represent the state of the art for commercially successful electrochemical energy storage technologies. If their potential were fully realized, Li-O_2 batteries will enable a driving range of electrical cars comparable to those powered by internal combustion engines (300 miles or longer per refuel).[9]

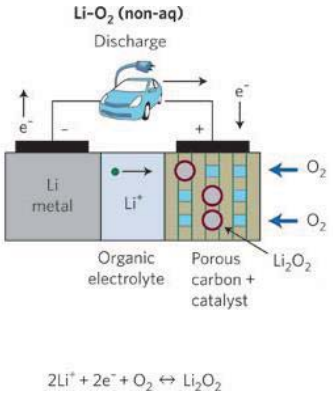

(**Figure 1.4** Operation mechanism of lithium oxygen battery. [Ref 7] - Reproduced by permission of NPG)

While progress has been made, the instability of electrode, electrolyte and their interface has been discovered as one of the key challenges impeding the development of the lithium oxygen battery technology.[10] The instability leads to significant parasitic reactions taking place during both cell discharge and charge. Byproducts including insoluble Li_2CO_3, LiOH and organic carbonates cause battery operation overpotentials to increase and the chemistry in the battery difficult to comprehend.[11] As a result, cells that can be cycled for more than 100 cycles without dramatic capacity drop are rare.

To help address the issue, much research has been designed and carried out to understand the detailed reaction mechanism of the oxygen reduction reaction (ORR),[12-14] during which step Li_2O_2 is formed, and the oxygen evolution reaction (OER),[15, 16] during which Li_2O_2 is decomposed to reproduce O_2 and Li^+. It was discovered that most of the electrolytes used previously, particularly the organic carbonates employed by early Li-O_2 studies, are not stable in the presence of O_2^-.[17] Because O_2^- is an important intermediate during cell operation, the reactivity between O_2^- and components of the cell is a serious issue and needs to be addressed. While some solvents (e.g., dimethoxyethane (DME),[17] dimethyl sulfoxide (DMSO)[18]) were found more stable than others, an ideal electrolyte that supports good O_2 solubility, allows for fast O_2 and Li^+ diffusion, and is stable against oxidation under cell operation conditions remains elusive. To further complicate the issue, it is recently reported that the carbon support popularly used in nearly all Li-O_2 studies is also not inert.[19] For instance, studies by Shao-Horn et al. revealed that the corrosion of carbon nanotube electrodes was severe under Li-O_2 cell operation conditions.[20] Bruce et al. observed that the extent of electrolyte decomposition depended on the type of substrates (different carbon substrates and Au),[21] and the electrolyte appeared far less stable when carbon was used.[22] The understanding that

carbon may promote electrolyte decomposition is also supported by density function theory (DFT) calculations.[23] When the carbon support is protected with Al_2O_3 prepared by atomic layer deposition (ALD), the decomposition of tetraethylene glycol dimethyl ether (TEGDME) is dramatically suppressed.[23] Most recently, Kang et al. reported that when $LiNO_3$ was added to the electrolyte (DME based), significantly lower amount of CO_2 was detected than without $LiNO_3$, and the authors understood the result as the deactivation of carbon support.[24] These recent results raise an important question: are there synergistic effects between the decomposition of carbon support and the electrolyte?

The second question is: to what extent can we narrow the discharge/charge potential gap with catalysts? While the nominal redox potential of $2Li^+ + O_2 \leftrightarrow Li_2O_2$ is 2.96 V (vs. Li^+/Li), the discharge potential is often <2.7 V and the recharge potential is >3.7 V at even relatively low current densities (100 mA/g_{carbon}), yielding round-trip efficiencies of <70%. The operation potentials of the discharge and recharge reactions are dependent on the detailed mechanisms[12, 25-27] and are sensitive to many other factors, including the morphology of Li_2O_2, the surface composition, the available cations in the solution, among others.[28-30] Without catalysts, the exchange current density of OER on carbon support is small (on the order of 10^{-9} A/cm^2),[15] meaning that large overpotentials are necessary to sustain a reasonable current density. In addition, the poor conductivity and low ionic diffusivity of Li_2O_2 increases electronic and ionic polarization within Li_2O_2.[31-33] Collectively they drive up the recharge potential, further increasing the potential gap and decreasing the round-trip efficiency. Although the application of OER catalysts has been shown to increase the exchange current density and, hence, the round trip efficiency,[34] how the usage of carbon contributes to the low round-trip efficiency has not been discussed in the literature.

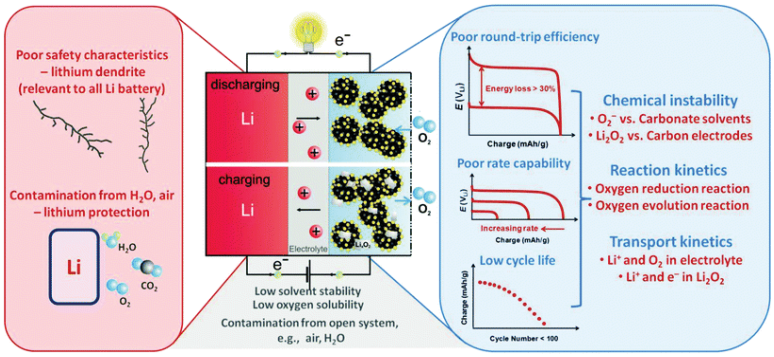

(**Figure 1.5** Challenges in lithium oxygen batteries. [Ref 11] - Reproduced by permission of The Royal Society of Chemistry)

To help answer these questions, the study of the formation and decomposition of Li_2O_2 on a carbon-free surface (Figure 1.6) has been proposed. In the first approach, carbon was replaced by a non-carbon material, the $TiSi_2$ nanonet; in the second approach, carbon surface was fully protected with a conformal coating of metal oxides. Both can eliminate potential reactions between carbon and O_2^- or Li_2O_2, as well as those between electrolytes and various intermediates that arise from carbon instability. So long as the support is of high surface area to allow for high Li_2O_2 loading, and good electrical conductivity to minimize electronic polarization, it will provide functionalities similar to what is offered by a porous carbon support. As such, the utilization of a cathode with carbon-free surfaces will allow us to understand Li_2O_2 formation and decomposition in a highly controlled environment, and the knowledge generated will help us discriminate to what extent the system degradation during Li-O_2 operation is caused by true electrolyte decomposition. For instance, when by-products such as carbonates and/or carboxylates are indeed observed on a carbon-free surface during discharge, we are confident that they are a result of electrolyte decomposition. The amount of by-products gives us a direct, quantitative measure of the instability of the electrolyte, with which we can now benchmark various electrolytes without being confounded by the influence of carbon

support. The study contributes to the fundamental understanding on the reversibility of Li oxygen batteries and design principles of Li oxygen batteries.

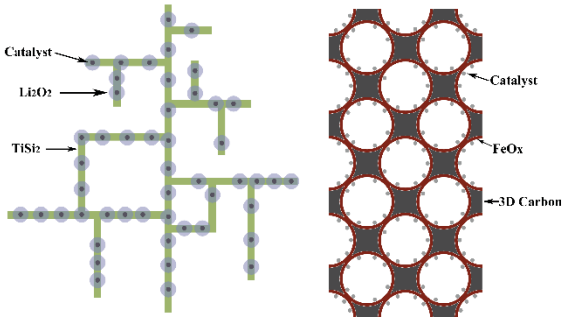

(**Figure 1.6** Schematic drawings of the chosen material platforms.)

1.4 References

(1) Winter, M.; Brodd, R. J. What Are Batteries, Fuel Cells, and Supercapacitors? *Chem. Rev.* **2004**, *104*, 4245-4269.

(2) Goodenough, J. B.; Kim, Y. Challenges for Rechargeable Batteries. *J. Power Sources* **2011**, *196*, 6688-6694.

(3) Tran, M.; Banister, D.; Bishop, J. D. K.; McCulloch, M. D. Realizing the Electric-Vehicle Revolution. *Nature Clim. Change* **2012**, *2*, 328-333.

(4) Dunn, B.; Kamath, H.; Tarascon, J. M. Electrical Energy Storage for the Grid: A Battery of Choices. *Science* **2011**, *334*, 928-935.

(5) Bruce, P. G.; Scrosati, B.; Tarascon, J.-M. Nanomaterials for Rechargeable Lithium Batteries. *Angew. Chem. Int. Ed.* **2008**, *47*, 2930-2946.

(6) Boukamp, B. A.; Lesh, G. C.; Huggins, R. A. All-Solid Lithium Electrodes with Mixed-Conductor Matrix. *J. Electrochem. Soc.* **1981**, *128*, 725-729.

(7) Bruce, P. G.; Freunberger, S. A.; Hardwick, L. J.; Tarascon, J. M. Li-O_2 and Li-S Batteries with High Energy Storage. *Nature Mater.* **2012**, *11*, 19-29.

(8) Abraham, K. M.; Jiang, Z. A Polymer Electrolyte-Based Rechargeable Lithium/Oxygen Battery. *J. Electrochem. Soc.* **1996**, *143*, 1-5.

(9) Thackeray, M. M.; Wolverton, C.; Isaacs, E. D. Electrical Energy Storage for Transportation-Approaching the Limits of, and Going Beyond, Lithium-Ion Batteries. *Energy Environ. Sci.* **2012**, *5*, 7854-7863.

(10) Lu, Y. C.; Gallant, B. M.; Kwabi, D. G.; Harding, J. R.; Mitchell, R. R.; Whittingham, M. S.; Shao-Horn, Y. Lithium-Oxygen Batteries: Bridging Mechanistic Understanding and Battery Performance. *Energy Environ. Sci.* **2013**, *6*, 750-768.

(11) McCloskey, B. D.; Valery, A.; Luntz, A. C.; Gowda, S. R.; Wallraff, G. M.; Garcia, J. M.; Mori, T.; Krupp, L. E. Combining Accurate O_2 and Li_2O_2 Assays to Separate Discharge and Charge Stability Limitations in Nonaqueous Li-O_2 Batteries. *J. Phys. Chem. Lett.* **2013**, *4*, 2989-2993.

(12) Zhai, D.; Wang, H.-H.; Yang, J.; Lau, K. C.; Li, K.; Amine, K.; Curtiss, L. A. Disproportionation in Li-O_2 Batteries Based on a Large Surface Area Carbon Cathode. *J. Am. Chem. Soc.* **2013**, *135*, 15364-15372.

(13) Yang, J.; Zhai, D.; Wang, H.-H.; Lau, K. C.; Schlueter, J. A.; Du, P.; Myers, D. J.; Sun, Y.-K.; Curtiss, L. A.; Amine, K. Evidence for Lithium Superoxide-Like Species in the Discharge Product of a Li-O_2 Battery. *Phys. Chem. Chem. Phys.* **2013**, *15*, 3764-3771.

(14) Lu, Y. C.; Crumlin, E. J.; Veith, G. M.; Harding, J. R.; Mutoro, E.; Baggetto, L.; Dudney, N. J.; Liu, Z.; Shao-Horn, Y. In Situ Ambient Pressure X-ray Photoelectron Spectroscopy Studies of Lithium-Oxygen Redox Reactions. *Sci. Rep.* **2012**, *2*, 715.

(15) Harding, J. R.; Lu, Y.-C.; Tsukada, Y.; Yang, S.-H. Evidence of Catalyzed Oxidation of Li_2O_2 for Rechargeable Li-Air Battery Applications. *Phys. Chem. Chem. Phys.* **2012**, *14*, 10540-10546.

(16) Zhong, L.; Mitchell, R. R.; Liu, Y.; Gallant, B. M.; Thompson, C. V.; Huang, J. Y.; Mao, S. X.; Shao-Horn, Y. In Situ Transmission Electron Microscopy Observations of Electrochemical Oxidation of Li_2O_2. *Nano Lett.* **2013**, *13*, 2209-2214.

(17) McCloskey, B. D.; Bethune, D. S.; Shelby, R. M.; Girishkumar, G.; Luntz, A. C. Solvents' Critical Role in Nonaqueous Lithium-Oxygen Battery Electrochemistry. *J. Phys. Chem. Lett.* **2011**, *2*, 1161-1166.

(18) Peng, Z.; Freunberger, S. A.; Chen, Y.; Bruce, P. G. A Reversible and Higher-Rate Li-O_2 Battery. *Science* **2012**, *337*, 563-566.

(19) Itkis, D. M.; Semenenko, D. A.; Kataev, E. Y.; Belova, A. I.; Neudachina, V. S.; Sirotina, A. P.; Havecker, M.; Teschner, D.; Knop-Gericke, A.; Dudin, P.; Barinov, A.; Goodilin, E. A.; Shao-

Horn, Y.; Yashina, L. V. Reactivity of Carbon in Lithium-Oxygen Battery Positive Electrodes. *Nano Lett.* **2013**, *13*, 4697-4701.

(20) Gallant, B. M.; Mitchell, R. R.; Kwabi, D. G.; Zhou, J.; Zuin, L.; Thompson, C. V.; Shao-Horn, Y. Chemical and Morphological Changes of Li-O_2 Battery Electrodes upon Cycling. *J. Phys. Chem. C* **2012**, *116*, 20800-20805.

(21) Freunberger, S. A.; Chen, Y.; Drewett, N. E.; Hardwick, L. J.; Barde, F.; Bruce, P. G. The Lithium-Oxygen Battery with Ether-Based Electrolytes. *Angew. Chem. Int. Ed.* **2011**, *50*, 8609-8613.

(22) Ottakam Thotiyl, M. M.; Freunberger, S. A.; Peng, Z.; Bruce, P. G. The Carbon Electrode in Nonaqueous Li-O_2 Cells. *J. Am. Chem. Soc.* **2013**, *135*, 494-500.

(23) Lu, J.; Lei, Y.; Lau, K. C.; Luo, X. Y.; Du, P.; Wen, J. G.; Assary, R. S.; Das, U.; Miller, D. J.; Elam, J. W.; Albishri, H. M.; Abd El-Hady, D.; Sun, Y. K.; Curtiss, L. A.; Amine, K. A Nanostructured Cathode Architecture for Low Charge Overpotential in Lithium-Oxygen Batteries. *Nat. Commun.* **2013**, *4*, 2383.

(24) Kang, S. J.; Mori, T.; Narizuka, S.; Wilcke, W.; Kim, H.-C. Deactivation of Carbon Electrode for Elimination of Carbon Dioxide Evolution from Rechargeable Lithium-Oxygen Cells. *Nat. Commun.* **2014**, *5*, 3937.

(25) McCloskey, B. D.; Scheffler, R.; Speidel, A.; Girishkumar, G.; Luntz, A. C. On the Mechanism of Nonaqueous Li-O_2 Electrochemistry on C and Its Kinetic Overpotentials: Some Implications for Li-Air Batteries. *J. Phys. Chem. C* **2012**, *116*, 23897-23905.

(26) Kang, S. Y.; Mo, Y. F.; Ong, S. P.; Ceder, G. A Facile Mechanism for Recharging Li_2O_2 in Li-O_2 Batteries. *Chem. Mater.* **2013**, *25*, 3328-3336.

(27) Laoire, C. O.; Mukerjee, S.; Abraham, K. M.; Plichta, E. J.; Hendrickson, M. A. Elucidating the Mechanism of Oxygen Reduction for Lithium-Air Battery Applications. *J. Phys. Chem. C* **2009**, *113*, 20127-20134.

(28) Horstmann, B.; Gallant, B.; Mitchell, R.; Bessler, W. G.; Shao-Horn, Y.; Bazant, M. Z. Rate-Dependent Morphology of Li_2O_2 Growth in Li-O_2 Batteries. *J. Phys. Chem. Lett.* **2013**, *4*, 4217-4222.

(29) Adams, B. D.; Radtke, C.; Black, R.; Trudeau, M. L.; Zaghib, K.; Nazar, L. F. Current Density Dependence of Peroxide Formation in the Li-O_2 Battery and Its Effect on Charge. *Energy Environ. Sci.* **2013**, *6*, 1772-1778.

(30) Mitchell, R. R.; Gallant, B. M.; Shao-Horn, Y.; Thompson, C. V. Mechanisms of Morphological Evolution of Li_2O_2 Particles During Electrochemical Growth. *J. Phys. Chem. Lett.* **2013**, *4*, 1060-1064.

(31) Varley, J. B.; Viswanathan, V.; Norskov, J. K.; Luntz, A. C. Lithium and Oxygen Vacancies and Their Role in Li_2O_2 Charge Transport in Li-O_2 Batteries. *Energy Environ. Sci.* **2014**, *7*, 720-727.

(32) Geng, W. T.; He, B. L.; Ohno, T. Grain Boundary Induced Conductivity in Li_2O_2. *J. Phys. Chem. C* **2013**, *117*, 25222-25228.

(33) Gerbig, O.; Merkle, R.; Maier, J. Electron and Ion Transport in Li_2O_2. *Adv. Mater.* **2013**, *25*, 3129-3133.

(34) Cao, R.; Lee, J. S.; Liu, M. L.; Cho, J. Recent Progress in Non-Precious Catalysts for Metal-Air Batteries. *Adv. Energy Mater.* **2012**, *2*, 816-829.

Chapter 2 High Capacity Si/$TiSi_2$ Lithium Battery Anode

This chapter is adapted from: (1) Zhou, S.; Xie, J.; Wang, D. W. Understanding the Growth Mechanism of Titanium Disilicide Nanonets. *ACS Nano* **2011**, *5*, 4205-4210. (2) Xie, J.; Yang, X. G.; Zhou, S.; Wang, D. W. Comparing One- and Two-Dimensional Heteronanostructures As Silicon-Based Lithium Ion Battery Anode Materials. *ACS Nano* **2011**, *5*, 9225-9231.

2.1 Growth Mechanism of $TiSi_2$ Nanostructures

The titanium disicilicate ($TiSi_2$) nanonet is a material with a unique two-dimensional morphology and has proven beneficial for energy conversion and storage applications. Detailed knowledge about how the nanonet grows may have important implications for understanding seedless nanostructure synthesis, in general, but is presently missing. Here, we report our recent efforts toward correcting this deficiency. We show that the $TiSi_2$ nanonet growth is sensitive to the nature of the receiving substrates. High-yield nanonets are only obtained on those exhibiting no or low reactivities with Si. This result indicates that Si-containing clusters deposited on the substrate surfaces play an important role in the nanonet synthesis, and we suggest they serve to initiate the growth. The morphological complexity of the nanonet depends on the precursor concentrations but not on the growth durations. More $TiCl_4$ results in nanonets with more complex structures. We understand that once a beam of a $TiSi_2$ nanonet is formed, its sidewalls are resistant to branch formation. Instead, the tip of a beam is where a branch forms. This process is driven by the reactions between Ti- and Si-containing species. Building on this understanding, we demonstrate the creation of second-generation nanonets.

When their electrodes are made of nanomaterials or materials with nanoscale features, energy conversion and storage devices, such as solar cells and rechargeable batteries, often exhibit new and improved properties.[1-6] Depending on the detailed processes involved, different devices benefit from the electrode innovations at the nanoscale differently. For instance, better light absorption or improved charge collection or both have been shown by solar cells containing nanowires;[7-10] faster charge and discharge rate or prolonged cycling lifetime or both have been reported when nanostructures are used for Li-ion batteries.[2, 11-13] A key factor that enables these encouraging results is our ability to design and synthesize materials at the nanoscale. To advance research in these areas further, we need detailed understandings about how various chemical processes produce these nanostructures. Despite intense research efforts, however, this knowledge is limited.[5, 6, 14-18] The limitation is exemplified in the unique two-dimensional (2D) nanonet system that we recently studied.[19, 20] Different from other hierarchical or branched nanowires (or nanorods), the structural complexity of the nanonet is confined within a flat sheet. We have demonstrated that this novel material is a promising platform for a number of applications, including solar water splitting[21-24] and Li-ion batteries.[12, 13] Although our initial results suggest that the nanonet growth is governed by the nature of $TiSi_2$ crystal structures, and that higher Si-to-Ti ratios favor the 2D nanonet morphology,[19, 20] a number of important questions remain unanswered. For instance, how do the initial nuclei form? What is the driving force for the branch formation? Can we control the degree of the complexity? These questions are of fundamental importance to the revelation of the detailed processes involved in the nanonet synthesis and will likely contribute to the understanding of nanostructure synthesis in general. Answers to these questions may eventually enable the development of chemistries that can produce nanomaterials with desired morphologies and properties -- a grand challenge in materials chemistry -- and therefore will have a profound impact

on research in this field. Here, we report results that may help answer these questions. Our results show that the initiation of the nanonet growth is dependent on the type of substrates used and that the branch formation is driven by the reactions of the precursors at the growth tips. Using this understanding, we demonstrate that the complexity of the 2D structure can indeed be controlled and present the formation of second-generation nanonets.

2.1.1 Experimental Details

Material Preparation: Following the procedures reported before,[19, 20] we grew $TiSi_2$ nanostructures in a home-built chemical vapor deposition (CVD) system. Note: the system is configured such that the time required for a pressure change from the base level (0.5 Torr) to 5 Torr is generally less than 15 s. For a typical growth, the reaction chamber was heated to 675 °C, and 50 sccm SiH_4 (10% in He, Voltaix) and 2 sccm $TiCl_4$ (carried by 100 sccm H_2) were delivered into the chamber. The pressure was maintained constant at 5 Torr during the growth. The duration of a typical growth was 6 min.

For the production of more complex nanonets, the reaction chamber was evacuated to the base pressure (0.5 Torr) after a growth of $TiSi_2$ nanonets. During the process, all precursor and carrier gases were kept flowing at constant rates. Shortly after the pressure reached the base level (e.g., 15 s), the pressure was allowed to increase to 5 Torr again. The growth was maintained for 4 min before the system was evacuated again without precursor gases flowing. Afterward, the system was brought to room temperature for sample extractions.

The nanonet growth was also carried out on various substrates. They included Si (Wafernet, San Jose, CA), Si with thermally grown oxides (100 nm SiO_2; Wafernet), Si with Ni coating (100 nm,

prepared in a sputtering system; AJA international Orion-8), stainless steel (McMaster-Carr, 0.05 mm), Ti foil (Sigma, 0.127 mm), Ti foil with Pt coating (100 nm, prepared in an e-beam evaporation system; Lesker PVD 75), quartz (Chemglass, New Jersey). The Si coating on Ti foil was achieved by exposing a Ti foil in the same CVD system used for the nanonet growth. The deposition was carried out at 675 °C for 5 min with 50 sccm SiH_4 (10% in He) and 100 sccm H_2 flowing (P_{total} = 5 Torr). The resulting Si coating was estimated to be approximately 20 nm by SEM (JEOL, JSM6340F).

Nanonet Yield Quantification: Once synthesized, the nanonets on a given supporting substrate were surveyed by the SEM. The yield was quantified by counting how many nanonets were observed in a 24 × 18 μm^2 area. For a typical experiment, more than 15 frames of SEM pictures were examined to obtain an accurate measure of the average yield. The density of nanonets on Si substrates was set as 100% for the normalized yield.

Structural Characterizations: A scanning electron microscope (JEOL, JSM6340F) and a transmission electron microscope (JEOL, JEM2010F), operating at 5 and 200 kV, respectively, were used for structural characterizations. An energy-dispersive X-ray spectroscopy (EDS) attachment to the TEM was used to measure the chemical compositions.

2.1.2 Results and Discussion

To elucidate how the initial nucleation process takes place, we first carried out a series of growths on different substrates, including Si, Si with thermally grown oxides, quartz, Ti foil, Ti foil with a Pt coating, Ti foil with a Si coating, Si with a Ni coating, and stainless steel foil. A clear trend was observed when the nanonet yields on these substrates were directly compared. Generally, low yields

were obtained on substrates that can react with Si at elevated temperatures, as shown in Figure 2.1. For example, scarce $TiSi_2$ nanonets were found on Ni-coated substrates. The majority of the products were sheets that could be identified as $NiSi_x$.[25, 26] Given that the growth parameters, including the pressure (P), the temperature (T), the precursor flow rates (SiH_4 and $TiCl_4$, respectively), and the growth durations (t) were identical for all samples examined, we concluded that the different yields result from the differences in the nucleation processes on various substrates. We suggest that the initial nuclei leading to the production of $TiSi_2$ nanonets are made of Si, which form as a result of the SiH_4 thermal decomposition under the growth conditions. If the substrate onto which the nanonets are grown reacts with Si, the nuclei will fail to form, resulting in low or no yield of nanonets. That the yields on Si-based and Si-covered substrates (including those of amorphous and crystalline SiO_2) are comparable also supports this hypothesis because Si deposition on these surfaces is expected to be comparable. Note that the yield on Pt-coated substrates was lower than those on Si-based substrates by 30% presumably because of relatively poor adhesion of Si onto Pt surfaces.

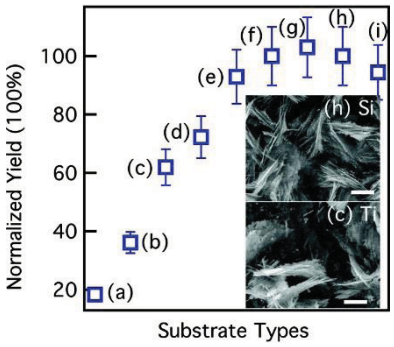

(**Figure 2.1** Comparison of $TiSi_2$ nanonet yields on different substrates. (a) Ni-coating on Si; (b) stainless steel; (c) Ti foil; (d) Ti foil with Pt coating; (e) Ti foil with Si deposition; (f) Si with thermally grown oxide; (g) quartz; (h) Si; (i) the backside of Si. The yield for each sample was normalized relative to that on the Si substrate. Two representative top-view scanning electron

micrographs (SEM) of $TiSi_2$ nanonets grown on Si and Ti, respectively, are included as insets. Scale bars: 1 μm.)

In addition, we suggest that the growth of $TiSi_2$ nanonet is a surface process but not a gas-phase one. This means the nanostructures are not formed in the gas phase and then deposited onto the receiving substrate. Instead, they directly grow on the surface. Two pieces of evidence support this conclusion. First, no measurable differences in the yield were observed on the front side (facing up) or the back side (facing down) of a Si substrate. Second, we did not observe any nanonets downstream away from the heated (i.e., the growth) region in the growth chamber. Once produced, the nanonets were typically affixed to the substrate and could survive harsh treatments such as pressurized gas blowing or rinsing. Our previous results indicated that the nanonets form a good electrical contact to the supporting substrate with negligible resistance.[12, 21, 23] This means the interface between the initial growth nuclei and the substrate surface is of high quality. The property is an added benefit if the nanonets are to be used for energy-related applications, where low impedance charge transport is desired.

We next sought to examine how the nanonets form the 2D complexity by observing the different stages of a nanonet growth, at 75 s, 90 s, 120 s, and 6 min, respectively (Figure 2.2). According to the existing literature, at least two competing mechanisms can be used to explain the formation of a complex nanostructure. The first one involves the formation of a trunk first, from which branches grow.[16, 17, 27-30] parts of a complex nanostructure can grow at the same time, creating the final product in a one-step reaction.[5, 19, 20, 30, 31] Our experimental observations indicated that the nanonet growth is likely governed by the second mechanism. As can be seen in Figure 2.2, the 2D nature of the nanonet was apparent 90 s after the growth was initiated. Throughout the growth, no branch-

free trunks dominate the morphology. It suggests that all branches within a nanonet are of similar chemical reactivities. We also note the growth progresses at a relatively rapid pace. The size of a nanonet typically reaches >2 μm in 6 min. This is consistent with the report by Kim et al. that silicide nanowires and nanotubes grow rapidly on the surface.[32]

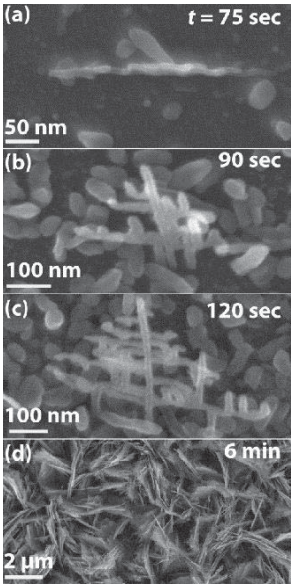

(**Figure 2.2** Evolution of $TiSi_2$ nanonets at different growth stages, varying from (a) 75 s, (b) 90 s, (c) 120 s, and (d) 6 min.)

Another important fact was revealed by Figure 2.2. Although the size of a nanonet increased as the growth continued, the complexity remained unchanged. The complexity can be quasi-quantitatively defined as the ratio between the areas covered by $TiSi_2$ branches and those by the voids if a nanonet were laid flat on a surface. It was approximately 1:2 for the nanonets shown in Figure 2.2 and was increased to 1:1 for those shown in Figure 2.3a, 4:1 in Figure 2.3b, and higher than 9:1 in Figure 2.3c when different growth conditions were applied. While the SiH_4 flow rate was fixed at 50 sccm, the $TiCl_4$ flow rates varied from 1.9, 2.3, to 3.0 sccm for those in Figure 2.3a-c, respectively. Indeed,

the nanonets shown in Figure 2.3c are so complex that they appear as continuous sheets, although voids as a result of the growth mechanism are still distinguishable. Significant to our discussions, the 2D nature of the highly complex nanonets remains unchanged.

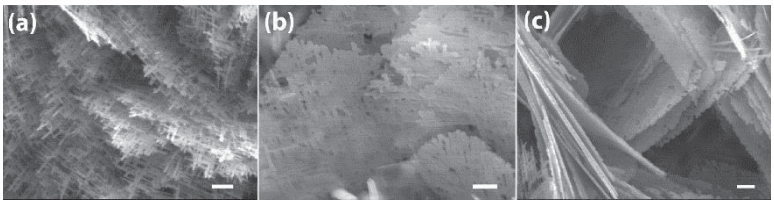

(**Figure 2.3** $TiSi_2$ nanonets of different complexities were produced under different $TiCl_4$ feeding rates: (a) 1.9 sccm, (b) 2.3 sccm, and (c) 3.0 sccm. The flow rate of SiH_4 was fixed at 50 sccm. Scale bars: 200 nm.)

We understand the result as follows. At the initial stage of the growth, nuclei mainly consisting of Si are formed. Subsequent co-deposition of Ti and Si to the nuclei leads to the formation of anisotropic $TiSi_2$ beams in a form similar to nanorods or short nanowires. Due to the passivation effect of Si on the (010) planes as a result of relatively high concentrations of SiH_4, the preferred crystal structure is C49 under the growth conditions (SiH_4 flow rate 50 sccm). As a C49 $TiSi_2$ beam continues to elongate, Ti-rich clusters occasionally break the Si passivation and lead to the formation of a branch perpendicular to the original beam. We hypothesize that the branching effect predominantly takes place at the growth front. That is, once a beam is formed, its sidewalls are passivated by Si; further deposition of Ti or Si or both onto the sidewalls is unlikely. The hypothesis is supported by the observation that the beams of a nanonet did not increase in diameters as the growth progressed. As a result of this branching mechanism, the complexity of a nanonet is determined by the growth condition (more specifically, the availability of Ti clusters). We believe Ti is the key reason for the branch formation because higher Ti concentrations produce more

complex nanonets. Alternatively, one may argue that Cl in $TiCl_4$ could be the reason for the greater complexities observed when higher flow rates of $TiCl_4$ were used. This possibility was ruled out by control experiments where HCl was intentionally added, which resulted in extremely low yield of nanonets. A summary of the understanding is schematically illustrated in Figure 2.4.

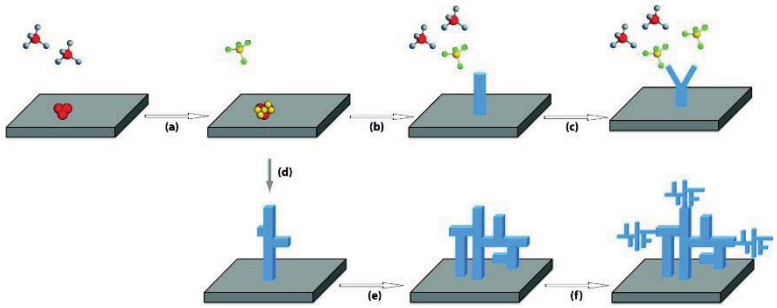

(**Figure 2.4** Schematics of the proposed mechanism governing the $TiSi_2$ nanonstructure growth. The chemistry starts with nucleus formation (a), followed by the elongation of C54 (b) and C49 (d) rods. The branching is caused by the breaking of side passivations at the growth front by Ti-containing clusters (c and e). Second-generation (2G) nanonets can be produced when the conditions change to suppress the continued growth of the original nanonets and to favor the initiation of new ones (f). Legends of color-coded balls in this schematic: red is Si; yellow is Ti; gray is H; and green is Cl.)

The key new information reported here is that Ti plays an important role in producing branched nanostructures. This conclusion is further supported by the following experimental observations. As we have previously reported, the products are predominantly $TiSi_2$ nanowires (of C54 crystal structure) when SiH_4 flow rate falls below 20 sccm.[20] Under the low flow rates of SiH_4, nanowires with branches were observed when relatively high $TiCl_4$ flow rates (e.g., >3.0 sccm) were used (Figure 2.5a-c). Several important features can be identified by examining the transmission electron microscopy (TEM) data in Figure 2.5c. We first direct the readers' attention to the splitting

phenomenon as highlighted by the yellow arrows. That the joints appear more than once indicates the splitting is not a random process. Next we used high-resolution TEM (HRTEM) and elemental analysis (energy-dispersive spectroscopy, EDS; also see Experimental Section) to study the joint areas and measured higher Ti-to-Si ratios (0.43:1) here than other areas (0.38:1; Figure 2.5). Note that the ratios were lower than the stoichiometric 0.5:1 as derived from the chemical formula ($TiSi_2$) because of the surface passivation by Si. This point has been previously discussed by us.[20] Despite the differences in the Ti/Si ratios, the crystal structure of the stem and the branches was C54 without observable defects. In other words, each wire, regardless of how many times it has split, is a monolithic piece.

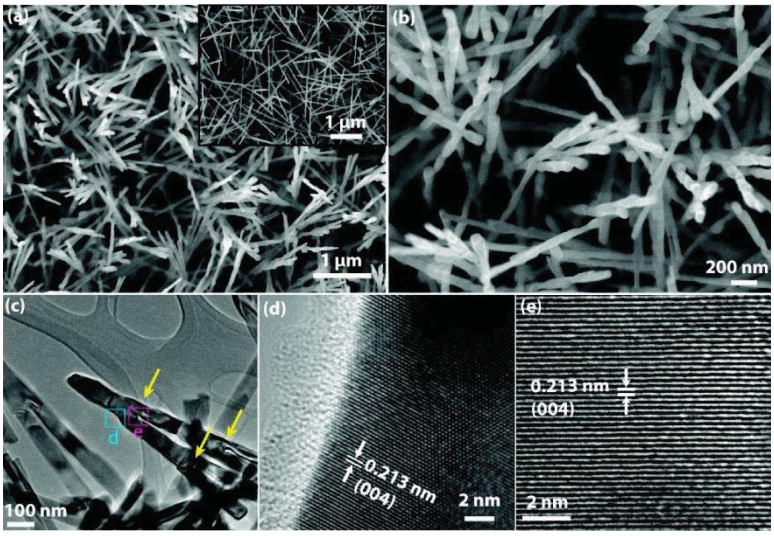

(**Figure 2.5** Splitting of $TiSi_2$ nanowires under high $TiCl_4$ flow rates. (a) Overview of nanowires with split tips by SEM. For a comparison, those without the splitting effect are shown in the inset. (b) Higher resolution SEM images reveal more details of how the nanowire tips split. (c) Further details are revealed in the TEM data. Yellow arrows point to the joints where the nanowire is split once (left arrow) and twice (right two arrows). The areas in the light blue and the purple squares are viewed under HRTEM mode, and the data are shown in (d) and (e).)

Presently, it is not clear why higher Ti concentration leads to the splitting of nanowires or the branching of nanonets. We hypothesize that the detailed processes may involve the breaking of Si passivation by the reaction between Ti and Si.[19, 20] The intricate balance between Si depositions that are inert (on the sidewalls) and those that react with Ti (on the growth fronts) may be critical to the unique seedless growth. It is also intriguing that once the sidewalls (passivated by Si) are formed, they are resistant to further reactions, which we believe is due to the existence of Cl in the synthesis system. It is important to note that the condition windows for the various nanostructures' growths are relatively narrow, beyond which the main products are generally featureless particles made of Ti and Si.

Lastly, we show the understanding that Si-containing clusters initiate the growth and that Ti-containing ones produce complexity can help us create more complex nanostructures. After a typical nanonet growth lasting 15 min, the pressure of the reaction chamber was brought to the base level (0.5 Torr), which caused the nanonets to stop growing. Shortly afterward (15 s), the precursors (SiH_4 and $TiCl_4$) were introduced to raise the pressure to 5 Torr again. Instead of observing the previously produced nanonet continue to grow, we found new nanonets formed from the beam tips (and from the tips only), creating second-generation (2G) nanonets (Figure 2.6). This phenomenon may be explained as follows. After the growth was stopped, the growth tips remained active. However, when the reactants were reintroduced, the previous balance between the tip growth and the side passivation no longer existed. Instead, a new balance was established, leading to the production of new nanonets. Because the tips of the previously grown nanonets were the most active, new nanonets tended to grow from there. We later discovered that the production of 2G nanonets was highly reproducible and that relatively mild changes of pressures (e.g., from 5 to 4

Torr during the growth) accompanied by disruptions of the continuous feeding of the precursors could yield similar results, although the effect was less pronounced. These highly complex nanostructures are of higher surface areas than simple nanonets or nanowires and therefore may be of interest for energy-related applications.

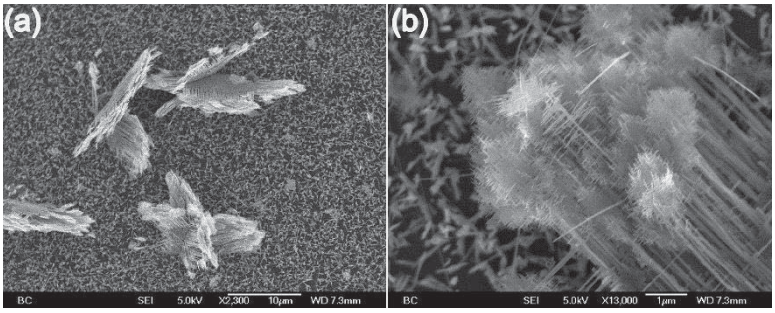

(**Figure 2.6** Creation of more complex nanonets. When the growth of nanonets was perturbed and then resumed, 2G nanonets were produced at the tips of the previously grown ones. The structures are shown under different magnifications in (a) and (b) by SEM.)

2.1.3 Conclusions

Many studies on nanostructure synthesis are driven by how the resulting materials may be used for various applications. A critical challenge in this area is to produce materials with controlled compositions, crystal structures, morphologies, and properties. Seemingly elusive, this goal might be eventually achieved if we gain enough understanding on the chemistries that produce various nanostructures. Reported here were our efforts toward this goal. In line with other literature reports, we discovered that the yield of $TiSi_2$ nanonets depended on the type of substrates they were grown on, from which we concluded the growth was initiated by the formation of Si-containing clusters. We found the complexity of $TiSi_2$ nanonets did not change as a function of growth time but was only sensitive to the precursor concentrations. This observation led us to uncover the role played

by Ti-containing clusters, which was to split the growth fronts. We demonstrated that this understanding could be used to produce second generation nanonets on the tips of existing ones. The resulting materials may be useful for energy related research owing to their unique morphological complexities and their physical and chemical properties.

2.2 Si/$TiSi_2$ Heteronanostructure Anode for Lithium Ion Batteries

The performance of advanced energy conversion and storage devices, such as solar cells, supercapacitors, and lithium (Li) ion batteries, is intimately connected to the electrode design at the nanoscale. To enable significant developments in these research fields, we need detailed information about how the properties of the electrode materials depend on their dimensions and morphologies. This information is currently unavailable, as previous studies have mostly focused on understanding one type of morphology at a time. Here, we report a systematic study to compare the performance of nanostructures enabled by two platforms, one-dimensional nanowires and two-dimensional nanonets. The nanowires and nanonets shared the same composition (titanium disilicide) and similar sizes. Within the framework of Li ion battery applications, they exhibited different stabilities upon lithiation and delithiation (at a rate of 6 A/g), the nanonets-based nanostructures maintaining 90% and the nanowires-based ones 80% of their initial stable capacities after 100 cycles of repeated charge and discharge. The superior stability of the nanonets was ascribed to the two-dimensional connectivity, which afforded better structural stability than nanowires. Information generated by this study should contribute to the design of electrode materials and thereby enable broader applications of complex nanostructures for energy conversion and storage.

Being able to design, synthesize, and understand electrode materials with desired chemical, electronic, ionic, and physical properties plays a critical role in the development of advanced energy conversion and storage technologies, such as solar cells, rechargeable batteries, and supercapacitors. We consider the Li ion battery as an example. Despite its many advantages over other competing energy storage technologies, there is plenty of room for improvements in terms of power rate, cycle lifetime, and safety.[33-37] Among various considerations, that concerning power rate is worth particular research attention because solutions to this problem will involve the creation of materials with both high ionic and high electronic conductivity, a fundamental challenge in materials science.[38] Achieving high power rate is also of great practical implications, as it will greatly broaden where and how Li ion batteries can be used. Indeed, a great deal of research has been attracted to solving this challenge, including efforts to discover new compounds, new crystal structures, or both.[33, 39] Because the properties of materials are intimately connected to the designs at the nanoscale, considerable attention has been paid to using nanostructures as Li ion battery electrodes.[11, 36] For instance, nanoparticles,[40] nanowires,[2] and three-dimensional (3D) complex nanostructures[37] have been widely reported to exhibit new and improved performance on this front.

More recently, approaches to using multiple nanoscale components to form heteronanostructures have been proposed and reported by others and us.[12, 41-47] In a heteronanostructure, nanowires,[43] nanotubes,[44] nanonets,[12] graphene,[47] or 3D nanostructures[48] serve as structural support and charge transporter. On them are active material coatings, in the form of thin films or nanoparticles. With the fine features of the active materials at the nanoscale, the total time required for ionic diffusion is short; with the overall morphology at the micrometer scale, electronic charge transport is fast. As such this strategy allows for the measurement of combined large capacity, high power rate, and long cycle lifetime that cannot be measured on single-component materials and therefore has great

potential to dramatically advance Li ion battery research. To materialize these potentials, we need a detailed understanding of how the performance of the resulting heteronanostructures depends on the fine features. This requires systematic studies to compare the properties of heteronanostructures of similar compositions and comparable sizes but different morphologies. Due to the diversity of materials studied, however, little has been done to this end. In this article, we take the initiative to compare Si-based anode materials that involve two-dimensional (2D) and one-dimensional (1D) nanostructures and show that the morphology indeed influences the properties of the heteronanostructures to a measurable extent.

Our study is enabled by the unique $TiSi_2$ system, where we can produce either 2D nanonets or 1D nanowires of the same composition and similar sizes by adjusting the synthesis chemistry.[13, 19, 20, 49] They both can be interfaced with Si to act as structural supports, which will solve the poor stability issue, and charge transporters, which will meet the low conductivity challenge of Si. Although of similar sizes to 1D nanowires, the fine structures of the 2D nanonets are interconnected, providing a suitable platform to study how the complexity of the morphology influences the electrode materials' properties. Our results show that when the $TiSi_2$ is protected from reactions with Li^+, the nanonets exhibit better stability than the nanowires do. The difference is attributed to the multiconnectivity of the nanonets, which reduces failures due to the mechanical breakdown of individual $TiSi_2$ beams.

2.2.1 Experimental Details

Synthesis of $TiSi_2$/Si Heteronanostructure: $TiSi_2$ nanonets were synthesized using a chemical vapor deposition method as reported by us previously.[19, 49] Briefly, a Ti foil (Sigma, 0.127 mm thick, purity: 99.7%) coated with 100 nm W as the current collector was placed in a home-built reaction

chamber that was heated to 675 °C, and SiH_4 (10% in He, Voltaix; 50 sccm, standard cubic centimeter per minute), $TiCl_4$ (98%, Sigma-Aldrich; 2 sccm), and H_2 (Industrial grade, Airgas; 100 sccm) flew past the surface of the Ti foil at 5 Torr. A typical growth duration was 15 min. Afterward, SiH_4 and $TiCl_4$ were stopped, and the temperature was decreased to 650 °C, after which SiH_4 (80 sccm) was introduced again for Si coating. The reaction was carried out at 15 Torr for 12min. This process produced a particulate Si coating on the $TiSi_2$ nanowire or nanonet surfaces.

Material Characterizations: The samples before and after lithiation and delithiation processes were imaged using a transmission electron microscope (JEOL 2010F) and a scanning electron microscope (JEOL 6340F). The TEM was operated at an acceleration voltage of 200 kV, and the SEM was working at 10 kV. Elemental analysis was conducted using an energy dispersive spectroscopy attachment to the TEM.

Coin Cell Fabrication: After growth, the samples were transferred into an Ar-filled glove box (oxygen level <1 ppm). The $TiSi_2$/Si electrodes were assembled into coin cells (CR2032-type) with Li foils as the counter electrodes, 1 M $LiPF_6$ in ethylene carbonate and diethyl carbonate (1:1, Novolyte Technologies) as the electrolyte, and two layers of polypropylene separator (25 μm, Celgard 2500).

Electrochemical Measurements: The coin cells were characterized by an eight-channel battery analyzer with a battery test system (Shenzhen Neware, China) at 30 °C.

2.2.2 Results and Discussion

Design Considerations: The basis for our study is illustrated schematically in Figure 2.7. The design has two parts: $TiSi_2$ nanowires or nanonets and Si nanoparticles. Our previous study reveals that having Si in the particulate form (Figure 2.7a, c) is advantageous because the space between adjacent particles allows for volume expansion and reduction during lithiation (charge) and delithiation (discharge) of Si, respectively, thereby minimizing stress buildup during the processes.[12] Under idealized operating conditions, the $TiSi_2$ support remains intact during repeated charge and discharge processes, and the eventual degradation of Si would be the main failing mechanism. In practice, however, a number of processes can cause failures of the $TiSi_2$ nanowires and nanonets, consequently the failures of the electrode materials. The present study concerns one of these failing mechanisms, the mechanical breakdown of the nanowires and nanonets (Figure 2.7b, d). Factors that can contribute to this mechanism include lithiation-induced stress on the surfaces, unwanted chemical reactions of $TiSi_2$ with the electrolyte, and overheating, among others. The advantage of the nanonets-based design is obvious when such breakdown happens. In the case of nanowires, due to the loss of electrical contact with the current collector, the portion of the heteronanostructure beyond the cracking point will become inaccessible, as shown in Figure 2.7b, reducing the overall capacity. In the case of nanonets, such breakdown will have relatively limited influence on the overall capacity since the portions beyond the breaking point can still be connected to the current collector through other routes, as shown in Figure 2.7d. The overall capacity will fade at a comparatively slower pace than that of the nanowires-based nanostructures.

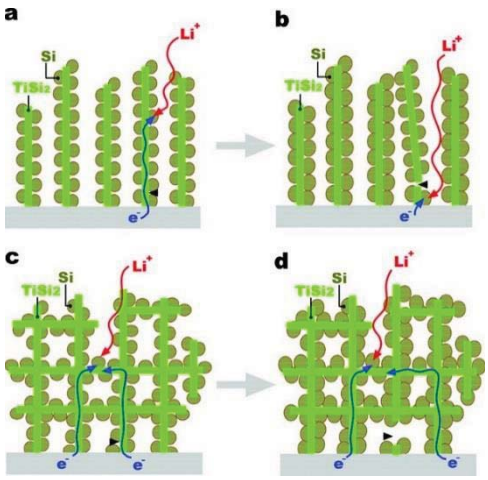

(**Figure 2.7** Schematic comparison of the nanowires- and nanonets-based systems. The basis for the designs is identical, i.e., to form Si nanoparticles on the nanowires (a) or the nanonets (c). In both cases, the nanowires or the nanonets serve as structural supports and charge transporters. The ionic and electronic pathways are illustrated by red and blue arrows, respectively. The difference is manifested when a mechanical breakdown occurs. (b) The portions of the nanowire beyond the breaking point will be inaccessible because of the loss of electrical contact. (d) Owing to the existence of other charge transport pathways within the nanonets, the breakdown of a single beam will have limited impact on the overall capacity.)

Structural Characterizations: The synthesis of $TiSi_2$ nanonets/Si heteronanostructures has been reported previously by us.[12] That of $TiSi_2$ nanowires/Si nanostructures is a new development, as our previous study concerned only the $TiSi_2$ nanowires without intentional Si deposition.[13] The parameters to deposit Si nanoparticles onto nanowires and nanonets were the same as detailed in the Experimental Section. The resulting nanostructures were characterized by a scanning electron microscope (SEM) and a transmission electron microscope (TEM). As can be seen in Figure 2.8, the fine features of the nanowires (Figure 2.8a, b) and the nanonets (Figure 2.8c, d) were of comparable sizes (diameters∼15-20 nm; lengths ∼1-5 μm). The as-deposited Si nanoparticles were

uniform and approximately 20-30 nm in diameter. Elemental analysis by energy dispersive spectroscopy (EDS) showed that the overall Si content (including that from $TiSi_2$) accounted for ca. 90% (wt %).

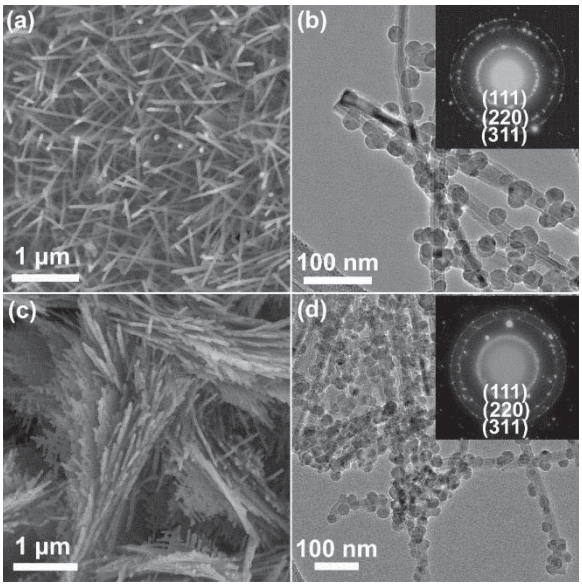

(**Figure 2.8** Structural characterizations of $TiSi_2$ nanowires- and nanonets-based heteronanostructures. (a and b) SEM and TEM micrographs of the nanowires-based nanostructures. (c and d) SEM and TEM micrographs of the nanonets-based nanostructures. Insets in (b) and (d) are selected area electron diffraction patterns, where the diffraction spots due to crystalline Si are characteristic of polycrystalline materials (highlighted by gray rings) because the data were collected on multiple Si particles.)

Comparison of Stabilities upon Repeated Charge/Discharge: To study the stabilities of $TiSi_2$ nanonets/Si and $TiSi_2$ nanowires/Si nanostructures, we assembled coin cells with the as-made materials as anodes. Li foils were chosen as the cathode electrode for the ease in accurately measuring the anode potentials relative to the Li/Lit standard. These coin cells were then connected

to a battery analyzer (more details in the Experimental Section), which passed a constant current through the cells and recorded the anode potentials as a function of time. The specific capacity was calculated by normalizing the number of charges (in units of mAh) against the total mass of the anode (in units of g). The mass of both $TiSi_2$ and Si was taken into account for the capacity calculations.

$TiSi_2$ Nanonets/Si Nanostructures: As shown in Figure 2.9a, the capacity increased from 2670 mAh/g to 2700 mAh/g during the first 5 cycles when tested within the potential window of 0.09-2 V (all potentials used in this article are relative to Li^+/Li unless noted). The Coulombic efficiency (CE) was 70% for the first cycle, which increased to 95.5% for the second cycle and then to 97.5% for the fifth cycle. We found it was important to carry out the first few cycles at a relatively slow rate (0.6 A/g, 0.2C, with 1C = 3000 mA/g). Otherwise, more rapid capacity fade and poorer performance than what is reported here would be measured. It has been suggested that during the first few cycles, together with other irreversible processes, the solid-electrolyte-interface (SEI) layer forms.[50] Nevertheless, we note that more research is needed to fully understand what role these initial lithiation/delithiation processes play. For the next five cycles, the operating potential window was further narrowed to within 0.15-2 V because our previous study shows that $TiSi_2$ nanonets react with Li^+ at approximately 0.09 V, and prolonged reactions at this potential will cause failures of the nanonets.[13] More on this point will be discussed later in this article. At a rate of 2.4 A/g (0.8C), the capacity changed from 1807 (6th cycle) to 1740 (10th cycle) mAh/g. In the meantime, the CE increased from 98.3% to 98.9%, suggesting that the lithiation/delithiation becomes more reversible after the initial charge/discharge. Afterward, the rate was changed to 6 A/g (2C). A trend of slightly increasing capacity with more charge/discharge cycles was observed until the 31st cycle, where a peak value of 1540 mAh/g was observed. Similar phenomena of

capacity increase during the initial lithiation/delithiation processes have been reported before,[43] and the reason was attributed to gradually more complete lithiation of Si.[51] Significantly, 1310 mAh/g was measured after 100 cycles of test, corresponding to 90% capacity retention from the 11th cycle. The CE varied between 97.9% and 99.3%, suggesting there were still irreversible processes to contribute to the capacity loss.

$TiSi_2$ Nanowires/Si Nanostructures: Compared with the nanonets-based nanostructures, the nanowires-based one showed at least two distinct characteristics. First, despite the similarities of sizes and amount of Si loading as evidenced by the structural studies, the initial and stable capacity of the nanowire system was lower. For example, the peak specific capacity measured at 6 A/g rate was 1335 mAh/g, 13% lower than that of the nanonets-based nanostructures. At the present stage, we do not fully understand the origin of this difference but suggest that the 2D nature and the unique surface properties of the nanonets may be important factors. Second, the capacity fade from the 11th cycle to the 100th one was more obvious, from 1263 to 1008 mAh/g, ~20%.

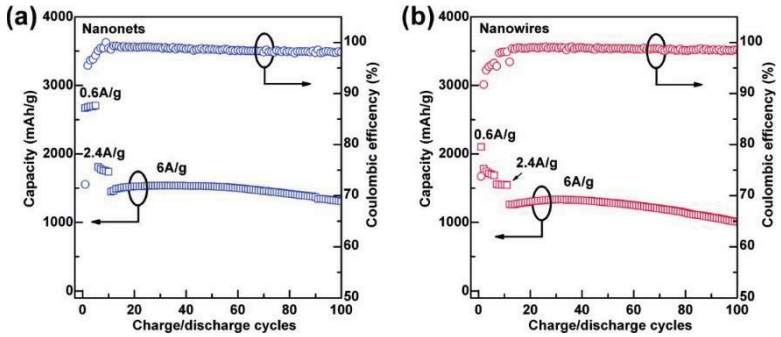

(**Figure 2.9** Cycling stability comparison of the nanonets- (a) and nanowires-based heteronanostructures (b). For clarity, only delithiation capacity is shown. The potential window for the first 5 cycles was 0.09-2 V, and that for the following tests was 0.15-2 V. The rates at which the performance was measured are labeled in the plots.)

Comparison of Stabilities under Different Operating Conditions: Our previous research has shown that $TiSi_2$ nanowires and nanonets react with Li^+ differently, the nanonets exhibiting appreciable lithiation at 0.09 V and the nanowires displaying no significant reactions down to 0.05 V.[13] With this information in mind, we next sought to examine how the operating potential windows influence the stability of the corresponding nanostructures. As can be seen in Figure 2.10 and similar to that in Figure 2.9, the nanonets-based samples showed higher capacities than the nanowire-based ones. Different from that in Figure 2.9, however, the capacities of the nanonets-based samples decreased more rapidly when measured at 0.05-2 V (from 2279 mAh/g at 31st cycle to 1449 mAh/g at 100th cycle) and 0.09-2 V (from 1949 mAh/g at 31st cycle to 1276 mAh/g at 100th cycle). An important reason for the more rapid capacity fade was the more complete lithiation of Si within these potential windows than that at 0.15-2V. As such, the fading mechanism specific to Si-related reactions plays an important role here. Although secondary, the reactions between the nanonets and Li^+ at or below 0.09 V should also contribute to the relatively more rapid capacity fade for the nanonets-based materials.[13]

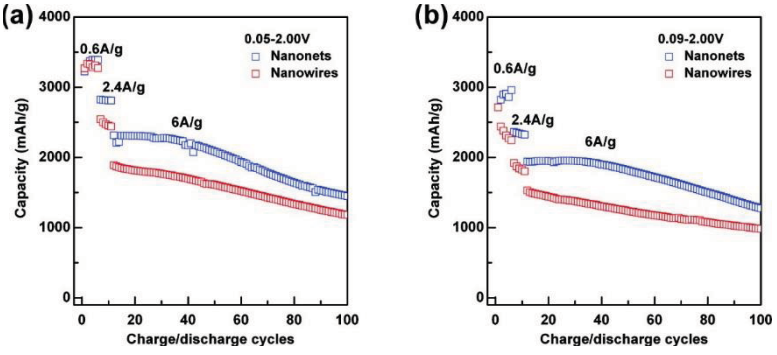

(**Figure 2.10** Stability comparison of the nanonets- and nanowires-based nanostructures. The cutoff potentials were 0.05 V (a) and 0.09 V (b). Note that the cutoff potential for data shown in Figure 2.9 was 0.15 V.)

Structural Studies after Repeated Charge/Discharge: To understand the stability differences between the nanowires- and nanonets-based nanostructures, we examined their morphologies after 100 cycles of tests; representative SEM micrographs are shown in Figure 2.11. These data are to be compared with those in Figure 2.8. Characteristic to the Si lithiation and delithiation processes, the crystalline and particulate Si coating was transformed into amorphous, accompanied by obvious volume expansion. However, there were also nanowires whose Si coating's transformation was less profound, such as those circled by ellipses in Figure 2.11a, b. It is conceivable that these nanowires did not undergo the same number of lithiation and delithiation processes as their neighboring ones did probably because they were separated from the current collector after the initial reactions. Indeed, both ends of these nanowires were visible within the viewing field. Nanowires like these would not contribute to the overall capacity and thus lead to capacity fade as shown in Figures 2.9 and 2.10. From Figure 2.11a, we can also find a considerable number of other nanowires where both ends are visible (highlighted by arrows), indicating that they were separated from the current collector and therefore would not contribute to the overall capacity should the sample be cycled further. Few such segments were found in Figure 2.8a, supporting that as-grown nanowires are connected to the current collector, a feature desired for Li ion battery applications. In contrast, uniform volume expansion of Si coating was observed on nanonets-based samples, and few broken nanonets were observed, Figure 2.11d, e. Although more detailed studies would be needed to fully understand in which mechanism the lithiation/delithiation of Si influences the stability of the $TiSi_2$/Si systems, we emphasize that the reactions between Li^+ and the $TiSi_2$-based nanostructures

are mainly limited to those with Si coatings. This point has been previously discussed by us[12, 13] and is further supported by Figure 2.11c, f, where the $TiSi_2$ core remains unchanged after repeated charge/discharge.

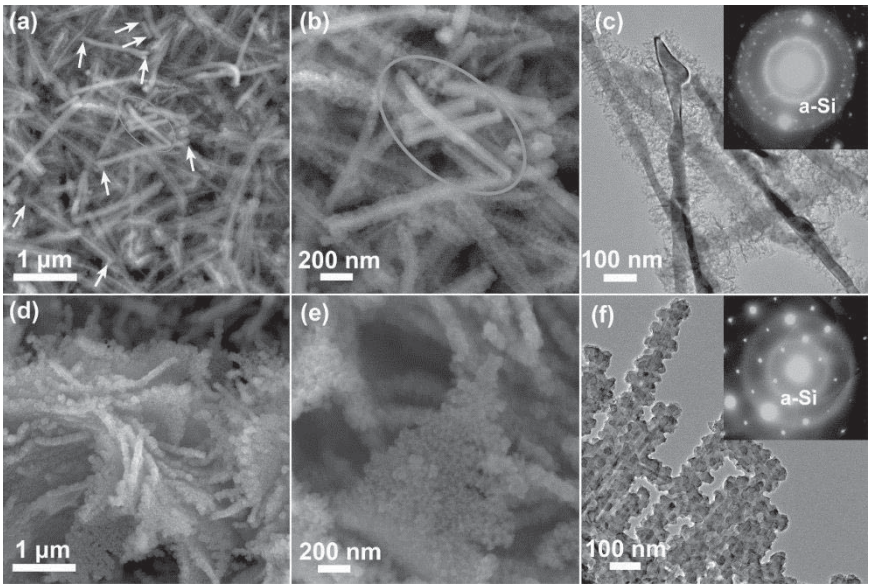

(**Figure 2.11** SEM micrographs of $TiSi_2$ nanowires- (a and b) and nanonets-based nanostructures (d and e) after 100 cycles of repeated lithiation/delithiation processes. (c and f) TEM micrographs of the same samples as in (a) and (d), respectively. The diffraction patterns (insets in c and f) indicate Si has turned amorphous during the lithiation/delithiation processes. The diffraction spots in the inset of (f) are from C49 $TiSi_2$.)

Comparison of Performance at Different Charge/Discharge Rates: One key advantage of the heteronanostructure design is that it may enable high capacity and high power on one material at the same time. To examine this potential, we compared the nanowires- and nanonets-based nanostructures at different charge/discharge rates. As can be seen in Figure 2.12, the general trend was that lower capacity was measured at higher rates. For instance, a capacity of >2000 mAh/g was

measured on the nanonets-based nanostructures at 0.6 A/g (0.2C); the same sample showed a capacity of ca. 800 mAh/g when measured at 15 A/g (5C). Once the rate was reduced to 3 and 0.6 A/g, the capacity increased to 1602 and 1798 mAh/g, respectively, corresponding to 75% and 85% of its original values. This trend is consistent with other literature reports of Si-based anode materials.[2, 44] Slow Li^+ diffusion within Si, which results in incomplete lithiation/delithiation at high rates, is an important reason for this observation.

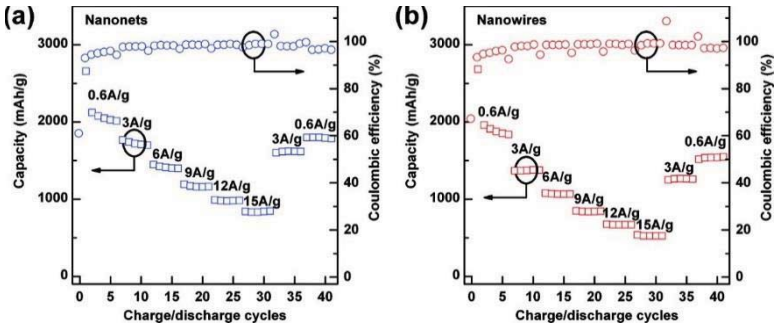

(**Figure 2.12** Comparison of nanonets- (a) and nanowires-based (b) materials at different charge/discharge rates. Because the Coulombic efficiencies were calculated by dividing the discharge capacity with the charge capacity, and these values changed dramatically when the rate was altered, we see noticeable changes of these values where the rates were varied.)

Although following the same general trend, the nanowires-based nanostructures exhibited noticeably poorer rate performance because the capacity dropped more quickly as the charge rate was increased, from ca. 1900 mAh/g at 0.6 A/g to ca. 530 mAh/g at 15 A/g. It increased further to 1518 mAh/g when measured again at 0.6 A/g, corresponding to 77% of its original capacity. We note the differences between nanowires- and nanonets-based materials in their performance under different rates are quasi-quantitative and as such are not sufficient for us to draw meaningful conclusions. This result nonetheless proves that the heteronanostructure design may indeed enable

the measurement of high power rate because it can be charged at rates up to 15 A/g. Previously, similarly high capacities have been measured on thin films albeit at much lower rates (~2000 mAh/g on 100 nm Si thin film at C/4).[50] The loading of active materials in the heteronanostructure design can be significantly higher than that in thin films owing to the surface roughening effect. The rate performance achieved here is comparable to the reported values of 1387 mAh/g at 14 A/g for Si hollow nanosphere by Cui et al.[52] or 900 mAh/g at 2.5C for Si and carbon nanotube combinations by Kumta et al.[44]

2.2.3 Conclusions

In summary, we carried out a systematic study to compare how $TiSi_2$ nanowires- and nanonets-based Si nanostructures perform as anode electrode materials for Li ion batteries. Grown by similar chemistries and sharing comparable sizes, the $TiSi_2$ system offered us a unique platform to focus on how the morphology influences the properties without being confounded by factors such as composition or dimensions. Our results showed that 2D nanonets exhibited better capacity retention than 1D nanowires when measured between 0.15 and 2 V. The reason was ascribed to better structural integrity of the nanonets. We suggest that because complex nanostructures bridge length scales from angstroms to micrometers, a range highly relevant to processes fundamentally important to energy conversion and storage applications, they have great potentials as electrode materials to significantly advance research in this field.

2.3 References

(1) Hochbaum, A. I.; Yang, P. D. Semiconductor Nanowires for Energy Conversion. *Chem. Rev.* **2010**, *110*, 527-546.

(2) Chan, C. K.; Peng, H. L.; Liu, G.; McIlwrath, K.; Zhang, X. F.; Huggins, R. A.; Cui, Y. High-Performance Lithium Battery Anodes Using Silicon Nanowires. *Nature Nanotech.* **2008**, *3*, 31-35.

(3) Huynh, W. U.; Dittmer, J. J.; Alivisatos, A. P. Hybrid Nanorod-Polymer Solar Cells. *Science* **2002**, *295*, 2425-2427.

(4) Tian, B.; Zheng, X.; Kempa, T. J.; Fang, Y.; Yu, N.; Yu, G.; Huang, J.; Lieber, C. M. Coaxial Silicon Nanowires as Solar Cells and Nanoelectronic Power Sources. *Nature* **2007**, *449*, 885-889.

(5) Liu, X.; Lin, Y.; Zhou, S.; Sheehan, S.; Wang, D. Complex Nanostructures: Synthesis and Energetic Applications. *Energies* **2010**, *3*, 285-300.

(6) Bierman, M. J.; Jin, S. Potential Applications of Hierarchical Branching Nanowires in Solar Energy Conversion. *Energy Environ. Sci.* **2009**, *2*, 1050-1059.

(7) Kayes, B. M.; Atwater, H. A.; Lewis, N. S. Comparison of the Device Physics Principles of Planar and Radial P-N Junction Nanorod Solar Cells. *J. Appl. Phys.* **2005**, *97*, 114302.

(8) Kelzenberg, M. D.; Boettcher, S. W.; Petykiewicz, J. A.; Turner-Evans, D. B.; Putnam, M. C.; Warren, E. L.; Spurgeon, J. M.; Briggs, R. M.; Lewis, N. S.; Atwater, H. A. Enhanced Absorption and Carrier Collection in Si Wire Arrays for Photovoltaic Applications. *Nature Mater.* **2010**, *9*, 239-244.

(9) Yuan, G.; Zhao, H.; Liu, X.; Hasanali, Z. S.; Zou, Y.; Levine, A.; Wang, D. Synthesis and Photoelectrochemical Study of Vertically Aligned Silicon Nanowire Arrays. *Angew. Chem. Int. Ed.* **2009**, *48*, 9680-9684.

(10) Yuan, G.; Aruda, K.; Zhou, S.; Levine, A.; Xie, J.; Wang, D. Understanding the Origin of the Low Performance of Chemically Grown Silicon Nanowires for Solar Energy Conversion. *Angew. Chem. Int. Ed.* **2011**, *50*, 2334-2338.

(11) Bruce, P. G.; Scrosati, B.; Tarascon, J.-M. Nanomaterials for Rechargeable Lithium Batteries. *Angew. Chem. Int. Ed.* **2008**, *47*, 2930-2946.

(12) Zhou, S.; Liu, X.; Wang, D. Si/$TiSi_2$ Heteronanostructures as High-Capacity Anode Material for Li Ion Batteries. *Nano Lett.* **2010**, *10*, 860-863.

(13) Zhou, S.; Wang, D. Unique Lithiation and Delithiation Processes of Nanostructured Metal Silicides. *ACS Nano* **2010**, *4*, 7014-7020.

(14) Lieber, C. M. Nanoscale Science and Technology: Building a Big Future from Small Things. *MRS Bull.* **2003**, *28*, 486-491.

(15) Xia, Y.; Yang, P.; Sun, Y.; Wu, Y.; Mayers, B.; Gates, B.; Yin, Y.; Kim, F.; Yan, H. One-Dimensional Nanostructures: Synthesis, Characterization, and Applications. *Adv. Mater.* **2003**, *15*, 353-389.

(16) Manna, L.; Milliron, D. J.; Meisel, A.; Scher, E. C.; Alivisatos, A. P. Controlled Growth of Tetrapod-Branched Inorganic Nanocrystals. *Nature Mater.* **2003**, *2*, 382-385.

(17) Wang, D.; Qian, F.; Yang, C.; Zhong, Z.; Lieber, C. M. Rational Growth of Branched and Hyperbranched Nanowire Structures. *Nano Lett.* **2004**, *4*, 871-874.

(18) Kanaras, A. G.; Soennichsen, C.; Liu, H.; Alivisatos, A. P. Controlled Synthesis of Hyperbranched Inorganic Nanocrystals with Rich Three-Dimensional Structures. *Nano Lett.* **2005**, *5*, 2164-2167.

(19) Zhou, S.; Liu, X.; Lin, Y.; Wang, D. Spontaneous Growth of Highly Conductive Two-Dimensional Single-Crystalline $TiSi_2$ Nanonets. *Angew. Chem. Int. Ed.* **2008**, *47*, 7681-7684.

(20) Zhou, S.; Liu, X.; Lin, Y.; Wang, D. Rational Synthesis and Structural Characterizations of Complex $TiSi_2$ Nanostructures. *Chem. Mater.* **2009**, *21*, 1023-1027.

(21) Lin, Y.; Zhou, S.; Liu, X.; Sheehan, S.; Wang, D. TiO_2/$TiSi_2$ Heterostructures for High-Efficiency Photoelectrochemical H_2O Splitting. *J. Am. Chem. Soc.* **2009**, *131*, 2772-2773.

(22) Liu, R.; Lin, Y.; Chou, L.-Y.; Sheehan, S. W.; He, W.; Zhang, F.; Hou, H. J. M.; Wang, D. Water Splitting by Tungsten Oxide Prepared by Atomic Layer Deposition and Decorated with an Oxygen-Evolving Catalyst. *Angew. Chem. Int. Ed.* **2011**, *50*, 499-502.

(23) Lin, Y.; Zhou, S.; Sheehan, S. W.; Wang, D. Nanonet-Based Hematite Heteronanostructures for Efficient Solar Water Splitting. *J. Am. Chem. Soc.* **2011**, *133*, 2398-2401.

(24) Lin, Y.; Yuan, G.; Liu, R.; Zhou, S.; Sheehan, S. W.; Wang, D. Semiconductor Nanostructure-Based Photoelectrochemical Water Splitting: A Brief Review. *Chem. Phys. Lett.* **2011**, *507*, 209-215.

(25) Decker, C. A.; Solanki, R.; Freeouf, J. L.; Carruthers, J. R.; Evans, D. R. Directed Growth of Nickel Silicide Nanowires. *Appl. Phys. Lett.* **2004**, *84*, 1389-1391.

(26) Kim, C.-J.; Kang, K.; Woo, Y. S.; Ryu, K.-G.; Moon, H.; Kim, J.-M.; Zang, D.-S.; Jo, M.-H. Spontaneous Chemical Vapor Growth of NiSi Nanowires and Their Metallic Properties. *Adv. Mater.* **2007**, *19*, 3637-3642.

(27) Lao, J. Y.; Wen, J. G.; Ren, Z. F. Hierarchical ZnO Nanostructures. *Nano Lett.* **2002**, *2*, 1287-1291.

(28) Bierman, M. J.; Lau, Y. K. A.; Jin, S. Hyperbranched PbS and PbSe Nanowires and the Effect of Hydrogen Gas on Their Synthesis. *Nano Lett.* **2007**, *7*, 2907-2912.

(29) Bierman, M. J.; Lau, Y. K. A.; Kvit, A. V.; Schmitt, A. L.; Jin, S. Dislocation-Driven Nanowire Growth and Eshelby Twist. *Science* **2008**, *320*, 1060-1063.

(30) Schmitt, A. L.; Higgins, J. M.; Szczech, J. R.; Jin, S. Synthesis and Applications of Metal Silicide Nanowires. *J. Mater. Chem.* **2010**, *20*, 223-235.

(31) Szczech, J. R.; Jin, S. Epitaxially-Hyperbranched FeSi Nanowires Exhibiting Merohedral Twinning. *J. Mater. Chem.* **2010**, *20*, 1375-1382.

(32) In, J.; Seo, K.; Lee, S.; Yoon, H.; Park, J.; Lee, G.; Kim, B. Morphology-Tuned Synthesis of Single-Crystalline V_5Si_3 Nanotubes and Nanowires. *J. Phys. Chem. C* **2009**, *113*, 12996-13001.

(33) Tarascon, J. M.; Armand, M. Issues and Challenges Facing Rechargeable Lithium Batteries. *Nature* **2001**, *414*, 359-367.

(34) Goodenough, J. B.; Kim, Y. Challenges for Rechargeable Li Batteries. *Chem. Mater.* **2010**, *22*, 587-603.

(35) Park, M.; Zhang, X. C.; Chung, M. D.; Less, G. B.; Sastry, A. M. A Review of Conduction Phenomena in Li-Ion Batteries. *J. Power Sources* **2010**, *195*, 7904-7929.

(36) Arico, A. S.; Bruce, P.; Scrosati, B.; Tarascon, J. M.; Van Schalkwijk, W. Nanostructured Materials for Advanced Energy Conversion and Storage Devices. *Nature Mater.* **2005**, *4*, 366-377.

(37) Long, J. W.; Dunn, B.; Rolison, D. R.; White, H. S. Three-Dimensional Battery Architectures. *Chem. Rev.* **2004**, *104*, 4463-4492.

(38) Kang, B.; Ceder, G. Battery Materials for Ultrafast Charging and Discharging. *Nature* **2009**, *458*, 190-193.

(39) Hautier, G.; Fischer, C. C.; Jain, A.; Mueller, T.; Ceder, G. Finding Nature's Missing Ternary Oxide Compounds Using Machine Learning and Density Functional Theory. *Chem. Mater.* **2010**, *22*, 3762-3767.

(40) Poizot, P.; Laruelle, S.; Grugeon, S.; Dupont, L.; Tarascon, J. M. Nano-Sized Transition-Metaloxides as Negative-Electrode Materials for Lithium-Ion Batteries. *Nature* **2000**, *407*, 496-499.

(41) Scrosati, B.; Garche, J. Lithium Batteries: Status, Prospects and Future. *J. Power Sources* **2010**, *195*, 2419-2430.

(42) Liu, R.; Duay, J.; Lee, S. B. Heterogeneous Nanostructured Electrode Materials for Electrochemical Energy Storage. *Chem. Commun.* **2011**, *47*, 1384-1404.

(43) Cui, L. F.; Ruffo, R.; Chan, C. K.; Peng, H. L.; Cui, Y. Crystalline-Amorphous Core-Shell Silicon Nanowires for High Capacity and High Current Battery Electrodes. *Nano Lett.* **2009**, *9*, 491-495.

(44) Wang, W.; Kumta, P. N. Nanostructured Hybrid Silicon/Carbon Nanotube Heterostructures: Reversible High-Capacity Lithium-Ion Anodes. *ACS Nano* **2010**, *4*, 2233-2241.

(45) Cui, L. F.; Yang, Y.; Hsu, C. M.; Cui, Y. Carbon-Silicon Core-Shell Nanowires as High Capacity Electrode for Lithium Ion Batteries. *Nano Lett.* **2009**, *9*, 3370-3374.

(46) Wang, H. L.; Cui, L. F.; Yang, Y. A.; Casalongue, H. S.; Robinson, J. T.; Liang, Y. Y.; Cui, Y.; Dai, H. J. Mn_3O_4-Graphene Hybrid as a High-Capacity Anode Material for Lithium Ion Batteries. *J. Am. Chem. Soc.* **2010**, *132*, 13978-13980.

(47) Wang, H. L.; Yang, Y.; Liang, Y. Y.; Cui, L. F.; Casalongue, H. S.; Li, Y. G.; Hong, G. S.; Cui, Y.; Dai, H. J. $LiMn_{1-x}Fe_xPO_4$ Nanorods Grown on Graphene Sheets for Ultrahigh-Rate-Performance Lithium Ion Batteries. *Angew. Chem. Int. Ed.* **2011**, *50*, 7364-7368.

(48) Rolison, D. R.; Long, J. W.; Lytle, J. C.; Fischer, A. E.; Rhodes, C. P.; McEvoy, T. M.; Bourga, M. E.; Lubers, A. M. Multifunctional 3D Nanoarchitectures for Energy Storage and Conversion. *Chem. Soc. Rev.* **2009**, *38*, 226-252.

(49) Zhou, S.; Xie, J.; Wang, D. W. Understanding the Growth Mechanism of Titanium Disilicide Nanonets. *ACS Nano* **2011**, *5*, 4205-4210.

(50) Graetz, J.; Ahn, C. C.; Yazami, R.; Fultz, B. Highly Reversible Lithium Storage in Nanostructured Silicon. *Electrochem. Solid State Lett.* **2003**, *6*, A194-A197.

(51) Krishnan, R.; Lu, T. M.; Koratkar, N. Functionally Strain-Graded Nanoscoops for High Power Li-Ion Battery Anodes. *Nano Lett.* **2011**, *11*, 377-384.

(52) Yao, Y.; McDowell, M. T.; Ryu, I.; Wu, H.; Liu, N. A.; Hu, L. B.; Nix, W. D.; Cui, Y. Interconnected Silicon Hollow Nanospheres for Lithium-Ion Battery Anodes with Long Cycle Life. *Nano Lett.* **2011**, *11*, 2949-2954.

Chapter 3 Synthesis of Pt/$TiSi_2$ Heteronanostructures

This chapter is adapted from: Xie, J.; Yang, X.; Han, B.; Shao-Horn, Y.; Wang, D. Site-Selective Deposition of Twinned Platinum Nanoparticles on $TiSi_2$ Nanonets by Atomic Layer Deposition and Their Oxygen Reduction Activities. *ACS Nano* **2013**, *7*, 6337-6345.

For many electrochemical reactions such as oxygen reduction, catalysts are of critical importance, as they are often necessary to reduce reaction overpotentials. To fulfill the promises held by catalysts, a well-defined charge transport pathway is indispensable. Presently, porous carbon is most commonly used for this purpose, the application of which has been recently recognized to be a potential source of concern. To meet this challenge, here we present the development of a catalyst system without the need for carbon. Instead, we focused on a conductive, two-dimensional material of a $TiSi_2$ nanonet, which is also of high surface area. As a proof-of-concept, we grew Pt nanoparticles onto $TiSi_2$ by atomic layer deposition. Surprisingly, the growth exhibited a unique selectivity, with Pt deposited only on the top/bottom surfaces of the nanonets at the nanoscale without mask or patterning. Pt (111) surfaces are preferably exposed as a result of a multiple-twinning effect. The materials showed great promise in catalyzing oxygen reduction reactions, which is one of the key challenges in both fuel cells and metal air batteries.

3.1 Experimental Details

$TiSi_2$ Nanonet Synthesis: $TiSi_2$ nanonets were synthesized by a chemical vapor deposition method. A Ti foil (Sigma-Aldrich, 0.127 mm thick, purity 99.7%) was placed in a home-built reaction

chamber and heated to 675 °C. Then, SiH_4 (10% in He, Voltaix; at 50 standard cubic centimeters per minute, or sccm), $TiCl_4$ (98%, Sigma-Aldrich; 2 sccm), and H_2 (industrial grade, Airgas; 60 sccm) were introduced to the chamber, and the pressure was maintained constant at 5 Torr. The growth duration was typically 10-120 min for varying sizes and densities of nanonets.

TiO_2-Coated $TiSi_2$ Nanonets: TiO_2 was deposited in a Cambridge Nanotech (Savannah 100) ALD system following procedures we previously reported.[1] In brief, the reaction took place at 275 °C with a constant flow of N_2 at 20 sccm. Titanium(IV) isopropoxide ($Ti(iPrO)_4$, heated to 75 °C) and deionized H_2O (room temperature) were used as reaction precursors. The pulse and purge times for $Ti(iPrO)_4$ and H_2O were 50ms and 10 s, 15ms and 10 s, respectively. A 10-cycle growth of TiO_2 (estimated thickness 0.5 nm) was applied to the $TiSi_2$ nanonets to modify the surface.

Si Nanowires: The preparation of Si NWs was reported previously.[2] Briefly, the Si (100) substrate (Wafernet) was cleaned with acetone, methanol, and 2-propanol sequentially. The substrate was then oxidized in H_2O_2/H_2SO_4 (1:3 vol/vol) solution at 90 °C for 10 min to remove heavy metals and organic residue and then rinsed by deionized water. Finally, the cleaned substrate was immersed into an $HF/AgNO_3$ solution (4 M HF and 0.02 M $AgNO_3$) for 30 min at 50 °C to produce Si NWs.

Atomic Layer Deposition of Pt: Pt nanoparticles were deposited in an Arradiance (Gemstar) atomic layer deposition system. The growth temperature was 250 °C, with trimethyl-methylcyclopentadienyl platinum(IV) ($MeCpPtMe_3$, heated to 75 °C) and compressed air (room temperature) as reaction precursors. Each cycle consisted of four repeated pulse/purges of

$MeCpPtMe_3$ for sufficient surface adsorption and one pulse/purge of O_2 to decompose $MeCpPtMe_3$. The purge gas was N_2, and its flow rate was 90 sccm.

Material Characterizations: As-grown samples were imaged using a transmission electron microscope (JEOL 2010F) and a scanning electron microscope (JEOL 6340F). The TEM was operated at an acceleration voltage of 200 kV, and the SEM was at 10 kV. Elemental analysis was conducted using an EDS attachment to the TEM.

Electrochemical Characterizations: $Pt/TiSi_2$ on flat Ti foil was attached onto the rotating disk electrode (glassy carbon electrode, 5 mm in diameter, Pine Instrument Co.) for electrochemical measurements. The Pt/C electrode in the control experiment was prepared by first ultrasonicating the Pt/C nanoparticles (46 wt% supported by Vulcan carbon, Tanaka Kikinzoku, average diameter of Pt nanoparticles is 3.5 nm) in deionized water (Millipore, 18.2MΩ) for 1 h to make the ink and then dropcasting the catalyst ink onto the same type of rotating disk electrode. The loading of nanoparticles was 50 $\mu g_{Pt}/cm^2_{disk}$.

Measurement of Effective Surface Area: Cyclic voltammograms were collected in 0.1 M KOH solutions at a temperature maintained at 25 °C. A Pt wire sealed in glass tubing and an Ag/AgCl electrode (4 M KCl, Pine Instrument Co.) were used as counter and reference electrode, respectively. The electrolyte was purged with N_2 (ultrahigh purity, Airgas) for 30 min before measurements. CVs were recorded at a scan rate of 50 mV s^{-1} between 0.05 and 1.10 V vs RHE until they were stabilized. CVs were then recorded and presented at a scan rate of 10 mV s^{-1} in the same voltage range for ESA measurements.

Characterization of Oxygen Reduction Activities: After ESA measurements, electrolyte was purged with O_2 (ultrahigh purity, Airgas) for 30 min before evaluating ORR activities of $Pt/TiSi_2$ and Pt/C samples. Polarization curves were recorded at various rotating rates (2500, 1600, 900, 400, 100 rpm) at a scan rate of 10 mV s^{-1} between 0.05 and 1.10 V vs RHE. To correct for capacitance contribution, oxygen reduction currents were obtained by subtracting the polarization curve in N_2 from the corresponding curve in O_2.

3.2 Results and Discussion

The discovery of materials with new compositions or novel morphologies or both has played an important role in advancing modern technologies such as those for electrical energy storage applications.[3-5] Conversely, the key challenges encountered in the development of these technologies are often connected to the material design, particularly that at the nanoscale. To illustrate this point, let us consider issues related to electrode design for proton exchange membrane fuel cells as an example.[6-10] To afford high current density, conductive frameworks with high surface area are desired for the electrode's construction. Porous carbon, especially those with nanoscale pores, is popularly used as a scaffold, onto which catalysts for ORR (oxygen reduction reaction) and/or HOR (hydrogen oxidation reaction) are dispersed. It has been realized that the choice of porous carbon presents issues that may limit the performance of fuel cells, including poor stability and reduced catalytic activities.[11] Indeed, poorer activities of ORR catalysts have been observed on a carbon support than on metal or metal alloy electrodes,[12-14] although in these examples carbon additives were still used to provide electrical transport pathways. To enable significant advances in the field of electrical energy storage, it is important to develop a conductive, porous material that is carbon free. On a fundamental level, this material may enable mechanistic studies to help understand what role a carbon support plays in degrading the performance of fuel

cell electrodes. On a practical level, the new material may serve as a replacement for carbon in future devices. To date, examples of low-cost, non-carbon-based porous conductive frameworks remain rare other than those involving precious metals.[15, 16] Here we examine whether $TiSi_2$ nanonets, which are inexpensive in nature and easy to prepare,[17-19] are suitable for this purpose. Intriguingly, when used to grow Pt, a highly unusual selective deposition was obtained, resulting in 5-fold twinned Pt nanoparticles whose (111) planes are preferably exposed. The $Pt/TiSi_2$ combination exhibits ORR activities in aqueous solutions comparable to that of an optimized commercial Pt/C catalyst, establishing that the nanonet is in fact a promising candidate for air electrode design and construction.

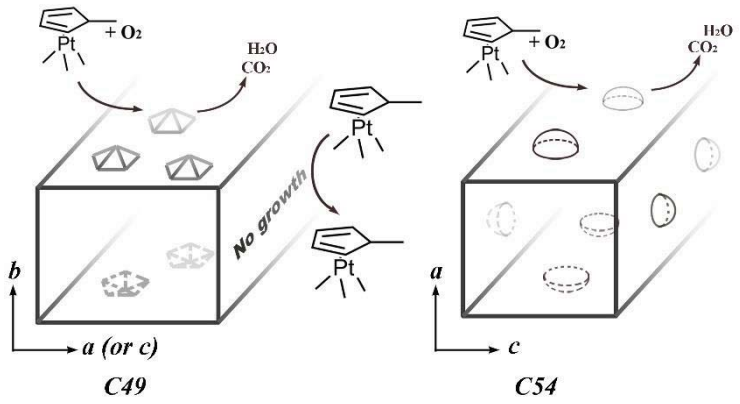

(**Figure 3.1** Schematics of Pt nanoparticle deposition on different $TiSi_2$ nanostructures. (Left) Selective deposition is achieved on the layered C49 $TiSi_2$, whose b planes consist of alternate layers of a Ti-Si mixture and Si-only atoms. Because the unit cell of C49 $TiSi_2$ is highly anisotropic (with a b lattice nearly four times that of a and c), its bulk form was known as metastable, and the only stable C49 $TiSi_2$ was found in nanonet morphology.[17, 18] Pt nanoparticles grow on the top and bottom surfaces, which are the b planes terminated by Si. For clarity, only one beam is shown here. (Right) Pt nanoparticles grow nonselectively on all surfaces on C54 $TiSi_2$ nanowires that are

identical in composition and similar in size to the nanonets. The main difference of C54 $TiSi_2$ from the C49 one is the lack of Si-only layers on its surface and, hence, the lack of layered, anisotropic structures.)

For this proof-of-concept work, we chose to interface Pt with $TiSi_2$ because it is a well-known ORR catalyst in aqueous systems.[20, 21] The wealth of prior knowledge about Pt catalytic behavior makes it easy to compare the performance of the Pt/$TiSi_2$ nanonet combination with that based on Pt/C. To obtain uniform coverage of Pt nanoparticles on the surface of $TiSi_2$ nanonets, which is important for electrochemical ORR reactions, atomic layer deposition (ALD) was used as the preparation method.[22] To our surprise and delight, a highly selective deposition was obtained, with Pt nanoparticles growing only on the (020) planes of $TiSi_2$ nanonets (see schematic illustration in Figure 3.1). Transmission electron micrographs (TEM) of top and side views (Figure 3.2a and b, respectively) confirmed that the deposition was indeed only on the top and bottom, but not on the side surfaces of $TiSi_2$ nanonets. For a total of more than 200 samples out of 30 batches of growth studied, all of them exhibited the same selectivity, thereby ruling out that the observation was a phenomenological effect. Although selective growth of nanoparticles such as Ag and Pt on the tips of ZnO[23] and CdS nanorods,[24, 25] respectively, has been reported, similar selectivity of gas-phase deposited nanoparticles on a nanostructured substrate has not been observed previously, to the best of our knowledge. We are therefore intrigued to study the possible causes for this unusual phenomenon.

Different from its bulk and nanowire counterparts, the nanonet form of $TiSi_2$ is of a layered structure known as C49. Our previous research revealed that the top and bottom surfaces of $TiSi_2$ nanonets are the b planes, which are made of only Si atoms.[17] We hypothesize that the unique crystal structure is the key reason for the selective deposition as described above. To prove the

growth is indeed specific to $TiSi_2$ nanonets, the following control experiments were carried out. First, Pt deposition on $TiSi_2$ nanowires was studied. As shown in Figure 3.1b schematically, and in Figure 3.3a and b, Pt nanoparticles of sizes comparable to those grown on $TiSi_2$ nanonets were obtained, but without obvious selectivity in their deposition sites, meaning that Pt nanoparticles were evenly distributed on all surfaces of the $TiSi_2$ nanowires. Given that $TiSi_2$ nanowires are of similar sizes and identical chemical compositions to $TiSi_2$ nanonets, it is understood that the small sizes (ca. ~20 nm in diameters) and chemical compositions ($TiSi_2$) are not the causes for the selective deposition. Second, to understand whether the nanonet morphology played a role in the selective deposition, we first grew a thin layer (10 ALD cycles) of TiO_2 by ALD on $TiSi_2$ nanonets, converting the surfaces (top, bottom, and sides) to a nondistinguishable TiO_2 coverage.[1] Subsequent ALD growth resulted in a uniform deposition of Pt nanoparticles (in Figure 3.3c and d). This result suggests the morphology alone is not the reason for the selective growth. Taken as a whole, we concluded that the selective deposition of Pt nanoparticles was specific to $TiSi_2$ nanonets, and the surfaces are the key reason for the selectivity. For the completeness of discussions about the uniqueness of $TiSi_2$ nanonets and important to electrocatalytic applications, it is worth noting that $TiSi_2$ nanonets exhibit a resistivity of ca. ~10 μΩ cm, which is approximately 10 times better than bulk C49 $TiSi_2$ and comparable to the more conductive C54. Our earlier work suggests that the improved conductivity is due to the lack of stacking faults along the b direction in the nanonets.[17]

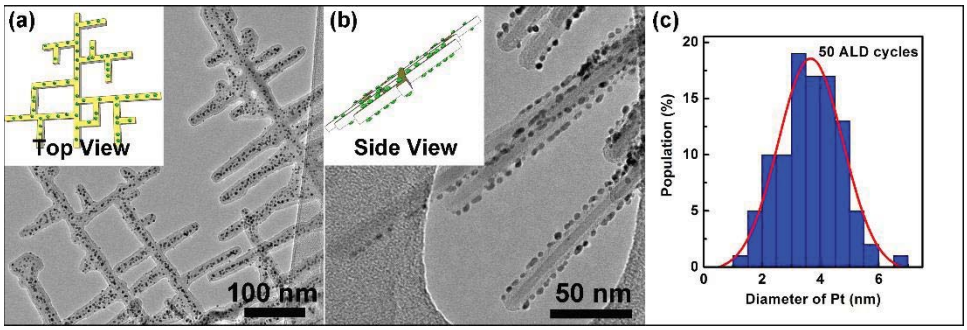

(**Figure 3.2** Microstructures of Pt/$TiSi_2$ heteronanostructures by a typical 50-cycle ALD growth. (a) When viewed from the top, a uniform distribution of Pt nanoparticles is observed. (b) When viewed from the side, Pt nanoparticles are seen only on the top and bottom surfaces of $TiSi_2$. The relationship is schematically illustrated in the insets. (c) The size distribution of Pt nanoparticles.)

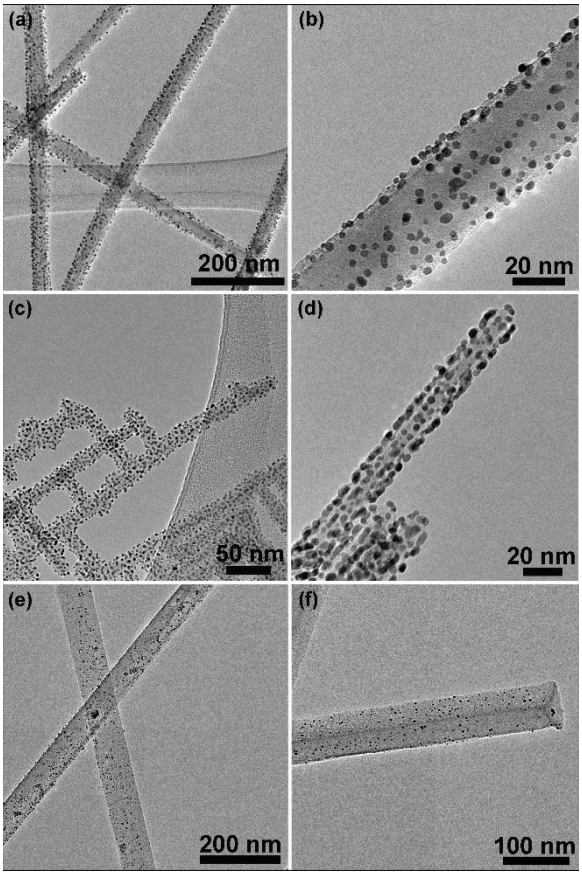

(**Figure 3.3** Transmission electron micrographs of Pt nanoparticles on various substrates by the ALD method. (a, b) C54 $TiSi_2$ nanowires; (c, d) TiO_2-coated C49 $TiSi_2$ nanonets; (e, f) Si nanowires.)

Previous research suggests that ALD growth of Pt with trimethyl(methylcyclopentadienyl) platinum(IV)($MeCpPtMe_3$) as a precursor starts with chemisorption of $MeCpPtMe_2$, followed by

oxidation of the remaining ligands to yield elemental Pt.[22] When the interface energy between Pt and the supporting substrate is relatively high, the deposition proceeds *via* a Volmer-Weber island mechanism, where nanoparticles instead of uniform films are produced. With this background information in mind, we see that the deposition of Pt should favor surfaces with low energies. For C49 $TiSi_2$, theoretical studies show that b planes are more stable than a and c planes by up to 20% in surface energies; the difference between various planes of C54 $TiSi_2$ is much less pronounced.[26] The surface energy difference may be an important factor that governs the selective growth. It is noted that although Si-termination on the top and bottom (020) surfaces of $TiSi_2$ nanonets has been unambiguously confirmed, further research is needed to understand why no Pt particles grow on the side surfaces at all. We nonetheless emphasize that the selective deposition is highly reproducible. Moreover, it is important to note that the selectivity appears specific to Pt deposition only. For instance, ALD growth of TiO_2,[1] WO_3,[27] and Fe_2O_3[28] on $TiSi_2$ nanonets all resulted in uniform coating with no measurable dependences on the crystal planes of C49 $TiSi_2$. Lastly, we note that Pt deposition on Si nanowires was also uniform but nonselective (Figure 3.3e and f), ruling out the possibility that Si-termination on the $TiSi_2$ nanonet is the sole reason for the observed selectivity.

The size of Pt nanoparticles and their mass loading density were found to depend on the ALD cycles following a pseudolinear relation (Figures 3.4 and 2c). There was an induction time (ca. 10 cycles) for Pt deposition with an island nucleation on the $TiSi_2$ nanonet substrate. The sizes and mass loading of Pt increased with increasing ALD Pt cycle numbers. For 30, 50, 70, and 100 cycles of ALD Pt deposition, the mean particle sizes were 2.6 ± 0.6, 3.6 ± 1.0, 6.4 ± 0.9, and 11.2 ± 1.1 nm, respectively, and their mass loadings as determined by energy dispersive spectroscopy (EDS) were 8.2 ± 2.3%, 29.2 ± 1.3%, 59.2 ± 3.2%, and 75.8 ± 3.9%, respectively. The quantification of

Pt loading was confirmed by ICP-OES (Perkin-Elmer Optima 3000 xl ICP-OES spectrometer) measurements, too.

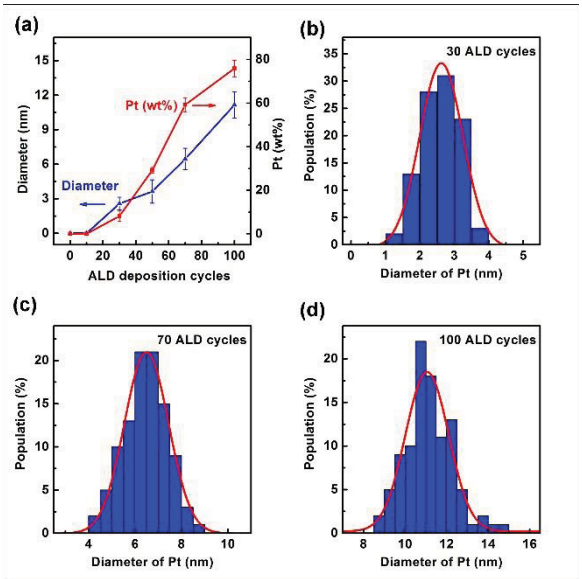

(**Figure 3.4** (a) Dependence of Pt nanoparticle sizes and mass loading (relative to the total mass of Pt and $TiSi_2$ nanonet support) on ALD cycle numbers. (b, c, d) Histograms of Pt nanoparticle diameters for 30, 70, and 100 ALD cycles of Pt deposition on $TiSi_2$ nanonets, respectively.)

The resulting Pt nanoparticles are crystalline in nature, as shown in Figure 3.5. Significantly, high resolution TEM (HRTEM) studies revealed that more than 90% of the Pt nanoparticles grown on $TiSi_2$ nanonets exhibited a multitwinned structure. A representative example with zone axis <110> is shown in Figure 3.5a. The angles between the twin planes range from 70° to 74°, in close resemblance to other 5-fold-twinned metal nanoparticles such as Ag[29] and Au[30]. Because such twinning effect exposes Pt (111) surfaces, which are believed to be catalytically more active, research efforts have been attracted to emulate the effect by, for example, growing a Pt epitaxial overlayer[31] on multiple-twinned nanoparticle cores or alloying with Pd[32]. High yields of pure Pt

nanoparticles that are 5-fold twinned have not been reported previously, to the best of our knowledge. The nanonet substrate was of critical importance to the high yield of the twinned Pt nanoparticles. When the nanonet was replaced by $TiSi_2$ nanowires or TiO_2-coated nanonets, the yield of twinned Pt nanoparticles dropped dramatically to <5%, although the total number of particles deposited remained comparable. We suggest that the interaction between Pt and the $TiSi_2$ nanonet b planes may be the key to the formation of twinned Pt nanoparticles. Lastly, it is noted that, probably due to their small sizes, no twinned particles were observed for Pt nanoparticles smaller than 2 nm.

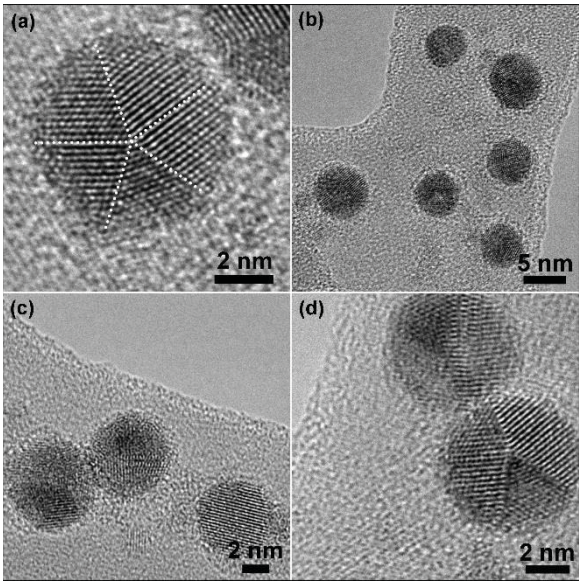

(**Figure 3.5** Representative high-magnification TEM images of multiple-twinned Pt nanoparticles deposited on $TiSi_2$ by ALD. (a) An unusual 5-fold twinning effect is observed in the high-resolution TEM image with zone axis <110>. (b-d) High yield of multiple-twinned Pt nanoparticles.)

In an effort to benchmark the performance of the unique $TiSi_2$ nanonet-Pt nanoparticle combination, we next studied its catalytic activity for ORR in aqueous solution, in Figure 3.6. For comparison,

electrodes of both Pt/$TiSi_2$ heteronanostructures and commercially obtained Pt/C (46 wt % supported by Vulcan carbon, Tanaka Kikinzoku) are shown in Figure 3.6a and b, respectively. Since the average diameter of Pt nanoparticles in the Pt/C catalyst was ~3.5 nm measured from TEM images (3-4 nm provided by vendor), we chose to test Pt nanoparticles of similar sizes, which were produced by a 50-cycle ALD growth. When $TiSi_2$ on Ti foil was used as a substrate (see Experimental Section for more details), an areal density of 50 $\mu g_{Pt}\ cm_{disk}^{-2}$ was obtained. Note that this loading density is modest and can be readily improved if needed for future work. For example, we see much room for improvement in terms of $TiSi_2$ density and the ALD growth of Pt. Nevertheless, as a proof-of-concept and to provide a direct comparison with the Pt/$TiSi_2$ sample, the Pt/C electrode was prepared such that a comparable areal density of Pt (50 $\mu g_{Pt}\ cm_{disk}^{-2}$) was achieved.

Cyclic voltammetry (CV) of both $TiSi_2$/Pt and Pt/C was first obtained in 0.1 M KOH at 25 °C, and the purpose was to measure their electrochemically active surface area (ESA). We note that this group of data was collected in alkaline solutions because our later characterizations were performed in solutions of the same conditions. As shown in Figure 3.6c, Pt/$TiSi_2$ heteronanostructures showed CV features characteristic of Pt (111) surfaces (more detailed analysis and discussion are available in the Supporting Information), which is in excellent agreement with our HRTEM characterizations. By comparison, the CV features of Pt/C were consistent with those of Pt (110) and (100) surfaces. From this group of data, a Pt ESA of 27.9$m^2\ g^{-1}$ was obtained on Pt/C, while Pt/$TiSi_2$ exhibited a slightly higher value of 35.1 $m^2\ g^{-1}$. Note that the areal densities in terms of Pt mass loading for both were comparable (ca. 50 $\mu g_{Pt}\ cm_{disk}^{-2}$). As such, the ESA difference is significant. One cause contributing to this difference may come from the multiple-twinned nature of Pt in Pt/$TiSi_2$, which exposes more (111) surface atoms.[31] Another reason may be found in the relatively simple interface

between $Pt/TiSi_2$, which ensures more Pt exposure; by comparison, in the Pt/C mixture, carbon may wrap around Pt to reduce the effective surface areas.

To study the ORR catalytic activity, we carried out the measurements in O_2-saturated alkaline solution (0.1 M KOH, 25 °C) by the rotating disk electrode technique. ORR polarization curves of both $Pt/TiSi_2$ and Pt/C at all rotating rates showed a diffusion- or mass-transfer controlled region at voltages below 0.6-0.7 V vs RHE (reversible hydrogen electrode) and diffusion-kinetic combined region above 0.7-0.8 V vs RHE. The limiting currents at the diffusion-controlled region are well defined as the current densities increase with $\omega^{1/2}$. As we clearly observe from Figure 3.6a and b, the polarization curves of $Pt/TiSi_2$ showed slight anodic shifts and more steep slopes than those of Pt/C, which indicated a better catalytic activity. The true kinetic current densities shown in Figure 3.6d were calculated according to the Koutecky-Levich equation (see Supporting Information). A nonoptimized $Pt/TiSi_2$ combination already exhibited superior performance when compared with the optimized commercial Pt/C. At 0.9 V vs RHE, the corrected kinetic current density of the $Pt/TiSi_2$ heteronanostructure was 160 $\mu A\ cm^2_{Pt}$, which is considerably higher than 90 $\mu A\ cm^2_{Pt}$ of Pt/C, indicating much higher ORR activity for the selectively grown Pt on $TiSi_2$ nanonets (see Supporting Information for discussions about how these values compare with literature reports). We suggest that the 5-fold twinned nature of the Pt nanoparticles is an important reason for the performance difference. We also noticed that $Pt/TiSi_2$ and Pt/C samples had slightly different slopes of 80.2 and 110.9mV/decade, respectively, which is again in good agreement with literature reports of pure Pt (111) and Pt (100) surfaces in 0.1 M KOH.[33]

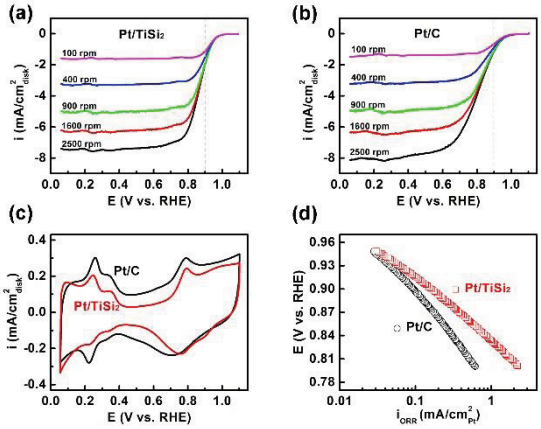

(**Figure 3.6** ORR catalytic activities of $Pt/TiSi_2$ and Pt/C in 0.1 M KOH electrolyte. (a) Polarization curves of $Pt/TiSi_2$ at a scan rate of 10 mV s^{-1} at varying rotation rates. (b) Polarization curves of Pt/C at a scan rate of 10 mV s^{-1} at various rotation rates. (c) The resulting $Pt/TiSi_2$ heteronanostructures exhibit different cyclic voltammetry characteristics (red trace) from that of a commercial Pt/C catalyst (black trace) when measured in O_2-free environments. (d) Tafel plots of the specific ORR activity of $Pt/TiSi_2$ and Pt/C based on $1/i = 1/i_k + 1/i_D$ at a rotation rate of 1600 rpm and a scan rate of 10 mV s^{-1}.)

To optimize the properties of $Pt/TiSi_2$ for further improvement of the catalytic activities as shown in Figure 3.6, we envision that the charge transfer kinetics may be increased by further optimizing the ALD process. In addition, we also predict that if the gas diffusion is improved, the saturation current should increase, as well. To reduce the limitation of mass transfer, we next show a set of experiments we carried out on porous supporting charge collectors of Ti mesh. Since $TiSi_2$ nanonets can be synthesized on a variety of different substrates,[19] this idea was readily tested. As a proof-of-concept, we chose to grow $TiSi_2$ nanonets on Ti mesh (wire diameter 250 μm; pore size 200 μm; Cleveland Wire Cloth), followed by ALD deposition of Pt nanoparticles. Structural studies by scanning electron microscopy (SEM) revealed that $TiSi_2$ nanonets grew uniformly on Ti mesh

(Figure 3.7a), including the junction areas of the interwoven wires (Figure 3.7b). A higher magnification scanning electron micrograph as shown in Figure 3.7c confirmed that $TiSi_2$ nanonets were of high density and purity. A significant advantage of the $TiSi_2$ nanonet synthesis is that the growth does not require growth catalysts, which greatly simplifies the electrode fabrication process and avoids producing unnecessary impurities to undermine the catalytic activities.

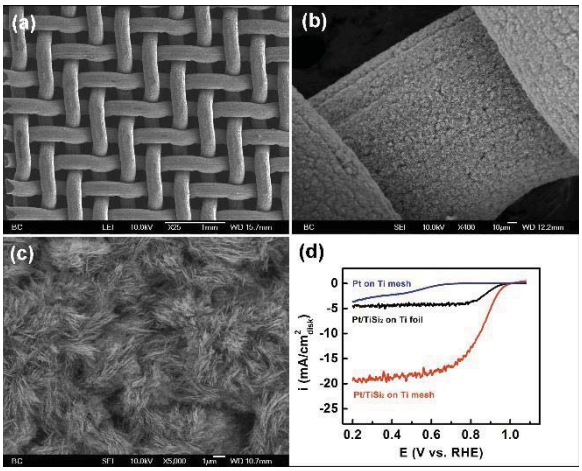

(**Figure 3.7** Structures of $Pt/TiSi_2$ heteronanostructures prepared on Ti mesh and their catalytic activities. (a-c) Low-, medium-, and high-magnification SEM images of $Pt/TiSi_2$ grown on Ti mesh. Inset in (c): a 50000× magnified view to reveal the two-dimensional nature of the nanonet morphology. (d) Polarization curve for ORR of $Pt/TiSi_2$ on mesh in 0.1 M KOH at a scan rate of 20 mV s^{-1} at 25 °C. As a comparison, the performances of Pt on Ti mesh in the absence of $TiSi_2$ nanonets (blue trace) and $Pt/TiSi_2$ on Ti foil (black trace) are shown. The Pt loading on $TiSi_2$ coated Ti foil and Ti mesh sample are 50 and 99 μg_{Pt} cm_{disk}^{-2}, respectively.)

Importantly, a saturation current density of 19.3 mA cm_{geo}^{-2} was measured (Figure 3.7d), which represents an almost 3-fold increase as compared with $TiSi_2$ on planar Ti foil. Note that the Pt loading per unit geometric area increased only from 50 to 99 μg_{Pt} cm_{geo}^{-2}, corresponding to an

increase of only 1-fold. We therefore understand the greater current density of Ti mesh samples as a result of better O_2 diffusion but not a simple increase of Pt loading. In general, the saturation current density in an ORR reaction is limited by three factors: the resistance in charge transfer, the resistance in charge transport, and the limitation of mass transport. Because the nature of Pt nanoparticles grown on $TiSi_2$/Ti mesh is identical to that of Pt nanoparticles prepared on $TiSi_2$/Ti foil, the differences in charge transfer and transport are expected to be negligible. As such, the change in mass transfer is the most plausible reason to explain the observed enhancement of saturation current densities. Similar results have been observed on traditional carbon paper when acting as a gas diffusion layer to enhance the mass transfer of O_2.[34] In addition, metal foams and meshes have been applied as Pt supports as well, especially in the case of direct methanol fuel cells.[35, 36]

3.3 Supplementary Information

Effective surface area measurements

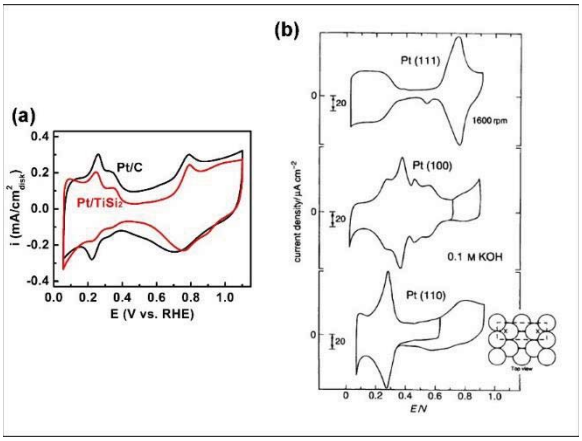

(**Figure 3.8** (a) CVs of $Pt/TiSi_2$ sample (red) and Pt/C sample (black) in 0.1 M KOH at 25°C; (b) CVs of Pt low-index single-crystal surfaces (Pt(111), Pt(100) and Pt(110)) in 0.1 M KOH. Adapted from Markovic *et al.*, *J. Chem. Soc., Faraday Trans.*, 1996 (ref. 37).[37])

ESA was determined from Pt-H adsorption/desorption region between 0.05-0.45 V *vs.* RHE. A surface charge density of 210 μC/cm^2 Pt for a monolayer adsorption/desorption of hydrogen on Pt surface was employed for estimation. For similar sizes of Pt particles on $TiSi_2$ nanonets and Vulcan carbon, the calculated surface areas normalized to per gram of Pt were 35.1 m^2 g^{-1} and 27.9 m^2 g^{-1}, respectively.

The CV of Pt/C sample in 0.1 M KOH has been reported by some of our previous papers.[38] Briefly, it showed the typical Pt-H underpotential deposition region, double-layer region, and Pt-oxide region. The Pt-H peaks at 0.2-0.3 V and 0.3-0.4 V can be attributed to the Pt-H interaction on Pt (110) and Pt (100) planes, respectively, based on the CVs of Pt single-crystal surfaces. However, the CV recorded on Pt/$TiSi_2$ showed a dramatically different pattern, with suppressed peaks from Pt-H interaction on Pt (110) and Pt (100) surfaces. Combining with the structure characterization data and the factor of low growth kinetics of ALD process, we suggested that Pt on $TiSi_2$ has a higher Pt (111) surface concentration than Pt on C.

ORR activities in this study and among literature reports

The kinetic current density in this study was calculated by Koutecky-Levich equation[39]

$1/i = 1/i_k + i/i_D$ Equation (1)

where i is the measured current density, i_k is the kinetic current density, and i_D is the diffusion limited current density. The specific activity or mass activity of Pt on carbon showed in Figure 3.3d in the main text was determined to be 90 μA/cm$^2_{Pt}$ or 26.4 mA/mg$_{Pt}$. It is noted that it may not be fair to directly compare these values with the best reported ones in the literature[40] as they are sensitive to measurement conditions (*e.g.*, types of electrolyte, impurity, temperature, O_2 partial

pressure, scan rates, etc.) and different types of Pt/C been measured (types of carbon, sizes/morphology of Pt NPs etc.), resulting in widely varying data from reports to reports.[7] For instance, it has been reported that the corrosion of glass flasks in the alkaline electrolyte may result in relatively low activities of the catalysts.[41] Nonetheless, it is important to note that under identical test conditions, an improved performance by Pt/$TiSi_2$ as compared with commercial Pt/C is unambiguous.

3.4 Conclusions

In conclusion, we have demonstrated a highly selective Pt growth on the b planes of $TiSi_2$ nanonets by atomic layer deposition. As-grown Pt nanoparticles exhibited an unusual 5-fold twinned structure that preferably exposes (111) surfaces of Pt. Because the resulting material showed high activity toward ORR reactions, it has great potential as a promising air cathode for applications such as proton exchange membrane fuel cells. The availability of non-carbon electrode construction, such as the Pt/$TiSi_2$ combination reported here, adds value in that it permits fundamental studies to discern what role carbon support plays in existing devices. In addition, these open structures may prove effective in enabling high current densities, which is a highly coveted feature for applications such as electric transportation.

3.5 References

(1) Lin, Y.; Zhou, S.; Liu, X.; Sheehan, S.; Wang, D. TiO_2/$TiSi_2$ Heterostructures for High-Efficiency Photoelectrochemical H_2O Splitting. *J. Am. Chem. Soc.* **2009**, *131*, 2772-2773.

(2) Yuan, G.; Aruda, K.; Zhou, S.; Levine, A.; Xie, J.; Wang, D. Understanding the Origin of the Low Performance of Chemically Grown Silicon Nanowires for Solar Energy Conversion. *Angew. Chem. Int. Ed.* **2011**, *50*, 2334-2338.

(3) Bruce, P. G.; Scrosati, B.; Tarascon, J.-M. Nanomaterials for Rechargeable Lithium Batteries. *Angew. Chem. Int. Ed.* **2008**, *47*, 2930-2946.

(4) Goodenough, J. B.; Kim, Y. Challenges for Rechargeable Li Batteries. *Chem. Mater.* **2010**, *22*, 587-603.

(5) Yang, P. D.; Tarascon, J. M. Towards Systems Materials Engineering. *Nature Mater.* **2012**, *11*, 560-563.

(6) Markovic, N. M.; Schmidt, T. J.; Stamenkovic, V.; Ross, P. N. Oxygen Reduction Reaction on Pt and Pt Bimetallic Surfaces: A Selective Review. *Fuel Cells* **2001**, *1*, 105-116.

(7) Gasteiger, H. A.; Kocha, S. S.; Sompalli, B.; Wagner, F. T. Activity Benchmarks and Requirements for Pt, Pt-Alloy, and Non-Pt Oxygen Reduction Catalysts for PEMFCs. *Appl. Catal., B* **2005**, *56*, 9-35.

(8) Stamenkovic, V. R.; Fowler, B.; Mun, B. S.; Wang, G. F.; Ross, P. N.; Lucas, C. A.; Markovic, N. M. Improved Oxygen Reduction Activity on $Pt_3Ni(111)$ via Increased Surface Site Availability. *Science* **2007**, *315*, 493-497.

(9) Gasteiger, H. A.; Markovic, N. M. Just a Dream-or Future Reality? *Science* **2009**, *324*, 48-49.

(10) Stephens, I. E. L.; Bondarenko, A. S.; Perez-Alonso, F. J.; Calle-Vallejo, F.; Bech, L.; Johansson, T. P.; Jepsen, A. K.; Frydendal, R.; Knudsen, B. P.; Rossmeisl, J.; Chorkendorff, I. Tuning the Activity of Pt(111) for Oxygen Electroreduction by Subsurface Alloying. *J. Am. Chem. Soc.* **2011**, *133*, 5485-5491.

(11) Wang, J. J.; Yin, G. P.; Shao, Y. Y.; Zhang, S.; Wang, Z. B.; Gao, Y. Z. Effect of Carbon Black Support Corrosion on the Durability of Pt/C Catalyst. *J. Power Sources* **2007**, *171*, 331-339.

(12) Adzic, R. R.; Zhang, J.; Sasaki, K.; Vukmirovic, M. B.; Shao, M.; Wang, J. X.; Nilekar, A. U.; Mavrikakis, M.; Valerio, J. A.; Uribe, F. Platinum Monolayer Fuel Cell Electrocatalysts. *Top. Catal.* **2007**, *46*, 249-262.

(13) Stamenkovic, V. R.; Mun, B. S.; Arenz, M.; Mayrhofer, K. J. J.; Lucas, C. A.; Wang, G. F.; Ross, P. N.; Markovic, N. M. Trends in Electrocatalysis on Extended and Nanoscale Pt-Bimetallic Alloy Surfaces. *Nature Mater.* **2007**, *6*, 241-247.

(14) Strasser, P.; Koh, S.; Anniyev, T.; Greeley, J.; More, K.; Yu, C. F.; Liu, Z. C.; Kaya, S.; Nordlund, D.; Ogasawara, H.; Toney, M. F.; Nilsson, A. Lattice-Strain Control of the Activity in Dealloyed Core-Shell Fuel Cell Catalysts. *Nature Chem.* **2010**, *2*, 454-460.

(15) Ding, Y.; Kim, Y. J.; Erlebacher, J. Nanoporous Gold Leaf: "Ancient Technology"/Aadvanced Material. *Adv. Mater.* **2004**, *16*, 1897-1900.

(16) Peng, Z.; Freunberger, S. A.; Chen, Y.; Bruce, P. G. A Reversible and Higher-Rate Li-O_2 Battery. *Science* **2012**, *337*, 563-566.

(17) Zhou, S.; Liu, X.; Lin, Y.; Wang, D. Spontaneous Growth of Highly Conductive Two-Dimensional Single-Crystalline $TiSi_2$ Nanonets. *Angew. Chem. Int. Ed.* **2008**, *47*, 7681-7684.

(18) Zhou, S.; Liu, X.; Lin, Y.; Wang, D. Rational Synthesis and Structural Characterizations of Complex $TiSi_2$ Nanostructures. *Chem. Mater.* **2009**, *21*, 1023-1027.

(19) Zhou, S.; Xie, J.; Wang, D. W. Understanding the Growth Mechanism of Titanium Disilicide Nanonets. *ACS Nano* **2011**, *5*, 4205-4210.

(20) Bing, Y. H.; Liu, H. S.; Zhang, L.; Ghosh, D.; Zhang, J. J. Nanostructured Pt-Alloy Electrocatalysts for PEM Fuel Cell Oxygen Reduction Reaction. *Chem. Soc. Rev.* **2010**, *39*, 2184-2202.

(21) Zhou, Z. Y.; Tian, N.; Li, J. T.; Broadwell, I.; Sun, S. G. Nanomaterials of High Surface Energy with Exceptional Properties in Catalysis and Energy Storage. *Chem. Soc. Rev.* **2011**, *40*, 4167-4185.

(22) Christensen, S. T.; Elam, J. W.; Rabuffetti, F. A.; Ma, Q.; Weigand, S. J.; Lee, B.; Seifert, S.; Stair, P. C.; Poeppelmeier, K. R.; Hersam, M. C.; Bedzyk, M. J. Controlled Growth of Platinum

Nanoparticles on Strontium Titanate Nanocubes by Atomic Layer Deposition. *Small* **2009**, *5*, 750-757.

(23) Pacholski, C.; Kornowski, A.; Weller, H. Site-Specific Photodeposition of Silver on ZnO Nanorods. *Angew. Chem. Int. Ed.* **2004**, *43*, 4774-4777.

(24) Amirav, L.; Alivisatos, A. P. Photocatalytic Hydrogen Production with Tunable Nanorod Heterostructures. *J. Phys. Chem. Lett.* **2010**, *1*, 1051-1054.

(25) Habas, S. E.; Yang, P. D.; Mokari, T. Selective Growth of Metal and Binary Metal Tips on CdS Nanorods. *J. Am. Chem. Soc.* **2008**, *130*, 3294-3295.

(26) Wang, T.; Oh, S. Y.; Lee, W. J.; Kim, Y. J.; Lee, H. D. Ab Initio Comparative Study of C54 and C49 $TiSi_2$ Surfaces. *Appl. Surf. Sci.* **2006**, *252*, 4943-4950.

(27) Liu, R.; Lin, Y.; Chou, L.-Y.; Sheehan, S. W.; He, W.; Zhang, F.; Hou, H. J. M.; Wang, D. Water Splitting by Tungsten Oxide Prepared by Atomic Layer Deposition and Decorated with an Oxygen-Evolving Catalyst. *Angew. Chem. Int. Ed.* **2011**, *50*, 499-502.

(28) Lin, Y.; Zhou, S.; Sheehan, S. W.; Wang, D. Nanonet-Based Hematite Heteronanostructures for Efficient Solar Water Splitting. *J. Am. Chem. Soc.* **2011**, *133*, 2398-2401.

(29) Sun, Y. G.; Ren, Y.; Liu, Y. Z.; Wen, J. G.; Okasinski, J. S.; Miller, D. J. Ambient-Stable Tetragonal Phase in Silver Nanostructures. *Nat. Commun.* **2012**, *3*, 971.

(30) Sanchez-Iglesias, A.; Pastoriza-Santos, I.; Perez-Juste, J.; Rodriguez-Gonzalez, B.; de Abajo, F. J. G.; Liz-Marzan, L. M. Synthesis and Optical Properties of Gold Nanodecahedra with Size Control. *Adv. Mater.* **2006**, *18*, 2529-2534.

(31) Yang, J. H.; Yang, J.; Ying, J. Y. Morphology and Lateral Strain Control of Pt Nanoparticles via Core-Shell Construction Using Alloy AgPd Core Toward Oxygen Reduction Reaction. *ACS Nano* **2012**, *6*, 9373-9382.

(32) Xia, Y. N.; Xiong, Y. J.; Lim, B.; Skrabalak, S. E. Shape-Controlled Synthesis of Metal Nanocrystals: Simple Chemistry Meets Complex Physics? *Angew. Chem. Int. Ed.* **2009**, *48*, 60-103.

(33) Ross, P. N. Oxygen Reduction Reaction on Smooth Single Crystal Electrodes. In *Handbook of Fuel Cells*, John Wiley & Sons, Ltd: 2010.

(34) Liang, Y. Y.; Li, Y. G.; Wang, H. L.; Zhou, J. G.; Wang, J.; Regier, T.; Dai, H. J. Co_3O_4 Nanocrystals on Graphene as a Synergistic Catalyst for Oxygen Reduction Reaction. *Nature Mater.* **2011**, *10*, 780-786.

(35) Arisetty, S.; Prasad, A. K.; Advani, S. G. Metal Foams as Flow Field and Gas Diffusion Layer in Direct Methanol Fuel Cells. *J. Power Sources* **2007**, *165*, 49-57.

(36) Chen, R.; Zhao, T. S. A Novel Electrode Architecture for Passive Direct Methanol Fuel Cells. *Electrochem. Commun.* **2007**, *9*, 718-724.

(37) Markovic, N. M.; Sarraf, S. T.; Gasteiger, H. A.; Ross, P. N. Hydrogen Electrochemistry on Platinum Low-Index Single-Crystal Surfaces in Alkaline Solution. *J. Chem. Soc. Faraday Trans.* **1996**, *92*, 3719-3725.

(38) Sheng, W. C.; Gasteiger, H. A.; Shao-Horn, Y. Hydrogen Oxidation and Evolution Reaction Kinetics on Platinum: Acid vs Alkaline Electrolytes. *J. Electrochem. Soc.* **2010**, *157*, B1529-B1536.

(39) Bard, A. J.; Faulkner, L. R. *Electrochemical Methods: Fundamentals and Applications*. 2000.

(40) Garsany, Y.; Baturina, O. A.; Swider-Lyons, K. E.; Kocha, S. S. Experimental Methods for Quantifying the Activity of Platinum Electrocatalysts for the Oxygen Reduction Reaction. *Anal. Chem.* **2010**, *82*, 6321-6328.

(41) Mayrhofer, K. J. J.; Wiberg, G. K. H.; Arenz, M. Impact of Glass Corrosion on the Electrocatalysis on Pt Electrodes in Alkaline Electrolyte. *J. Electrochem. Soc.* **2008**, *155*, P1-P5.

Chapter 4 Ru/$TiSi_2$: A Non-carbon Electrode for Lithium Oxygen Batteries

This chapter is adapted from: Xie, J.; Yao, X.; Madden, I. P.; Jiang, D.-E.; Chou, L.-Y.; Tsung, C.-K.; Wang, D. Selective Deposition of Ru Nanoparticles on $TiSi_2$ Nanonet and Its Utilization for Li_2O_2 Formation and Decomposition. *J. Am. Chem. Soc.* **2014**, *136*, 8903-8906.

Li-O_2 battery promises high capacity to meet the need for electrochemical energy storage applications. Successful development of the technology hinges on the availability of stable cathodes. The reactivity exhibited by carbon support compromises the cyclability of Li-O_2 operation. A non-carbon cathode support has therefore become a necessity. Using $TiSi_2$ nanonet as a high surface area, conductive support, we obtained a new non-carbon cathode material that corrects the deficiency. To enable oxygen reduction and evolution, Ru nanoparticles were deposited by atomic layer deposition onto $TiSi_2$ nanonets. A surprising site-selective growth whereupon Ru nanoparticles only deposit onto the b planes of $TiSi_2$ was observed. DFT calculations show that the selectivity is a result of different interface energetics. The resulting heteronanostructure proves to be a highly effective cathode material. It enables Li-O_2 test cells that can be recharged more than 100 cycles with average round-trip efficiencies greater than 70%.

4.1 Experimental Details

$TiSi_2$ Nanonet Synthesis: $TiSi_2$ nanonets were prepared by a chemical vapor deposition (CVD) method. A Ti mesh (Cleveland Wire Cloth) was placed in the reaction chamber and heated to

675 °C. SiH_4 (10% in He, Voltaix; at 50 standard cubic centimetres per minute, or sccm), $TiCl_4$ (98%, Sigma-Aldrich; 2 sccm), and H_2 (industrial grade, Airgas; 60 sccm) were introduced to the chamber concurrently. The growth lasted typically 10 to 120 min with the pressure maintained at 5 Torr.

Atomic Layer Deposition of Ru: Ru nanoparticles were deposited on as-grown $TiSi_2$ nanonets in an Arradiance (Gemstar) ALD system. The growth temperature was 290 °C, with bis(ethylcyclopentadienyl) ruthenium(II) ($Ru(EtCp)_2$, heated to 110 °C) and compressed air (room temperature) as reaction precursors. Each cycle consisted of 4 repeated pulse/purge sub-cycles of $Ru(EtCp)_2$ for sufficient surface adsorption and 1 pulse/purge of O_2 to decompose $Ru(EtCp)_2$. The purge gas was N_2, and its flow rate was 90 sccm. The loading of Ru was quantified using inductively coupled plasma optical emission spectrometry (ICP-OES) at the MIT Center for Materials Science and Engineering (CMSE) using an ACTIVA S (Horiba) ICP-OES Spectrometer.

Material Characterizations: Samples were imaged using a transmission electron microscope (JEOL 2010F) operating at an acceleration voltage of 200 kV. Raman spectra were obtained in a customized air-tight sample holder using Horiba XploRA micro Raman system with excitation laser of 532 nm. The surface species and oxidation states were characterized by an X-ray photoelectron spectrometer (K-alpha XPS, Thermo Scientific, Al Kα=1486.7eV).

Electrochemical Characterizations: 0.1M $LiClO_4$ in dimethoxyethane (DME) with water level lower than 10 ppm was used as purchased from Novolyte (BASF). Tetraethylene glycol dimethyl ether (TEGDME, ≥ 99%, Sigma-Aldrich) was first stored over freshly activated 4 Å molecular sieves and then distilled. The distilled TEGDME was stored over molecular sieves before usage.

$LiClO_4$ (99.99%, Battery grade, Sigma-Aldrich) was further baked at 130 °C under vacuum in the heatable tray of a glove box (MBraun) and then dissolved into TEGDME to give a 1M solution. Customized Swagelok type cells were used as the electrochemistry study platform. Cells were assembled in the glove box (O_2 and H_2O levels < 0.1 ppm) with Li foil as the anode, 2 Celgard 2500 film sheets as the separator, 0.1 M $LiClO_4$ in DME or 1 M $LiClO_4$ in TEGDME as the electrolyte. Ru-decorated $TiSi_2$ nanonets on Ti mesh (1 cm^2) were used as the cathode directly without further treatment. No binder or carbon was added in our system. The mass loading of $TiSi_2$ on Ti mesh is 0.1mg/cm^2 and Ru loading on each cathode is approximately 0.1mg/cm^2. The fianl weight ratio of Ru:$TiSi_2$ was 1:1. The loading quantity of each individual sample was measured by the mass gain after ALD growth using a microbalance and also confirmed by the ICP-OES.

For comparison, carbon black cathode was prepared by dispersing carbon black (Vulcan XC72) and Polytetrafluoroethylene (PTFE, 60wt% dispersion, Sigma-Aldrich) with weight ratio of 8:2 in Isopropanol (10mg carbon/mL) then drop coated on Ni foam with the loading density of 1mg/cm^2. The cathode was further dried in the vacuum oven at 100°C overnight. The Ru decoration was performed in the same fashion by ALD as described above after the preparation of the carbon electrode, and the result loading was around 5:1 for Carbon:Ru.

After cell assembly, oxygen (Ultrahigh purity, Airgas) was purged into the cell to replace Argon and the cell was then isolated from the gas line after reaching 780 Torr. Electrochemical characterizations were carried out on an electrochemical station (Biologic, VMP3).

DFT Calculation: The Vienna ab initio simulation package (VASP)[1, 2] was used to perform periodic density functional theory calculations with planewave bases. The projector augmented wave (PAW)

method was used to describe the interaction between electrons and the nuclei;[3] standard VASP-PAW potentials were used for Ti, Si, Pt, and Ru with a recommended kinetic energy cutoff of 245 eV. The Perdew-Burke-Ernzerhof form of the generalized gradient approximation was used for electron exchange and correlation.[4] Due to the large unit cell of the simulated systems, only Γ-point was used for the k-point sampling for structural optimization with a force convergence criterion of 0.025 eV/Å. The DFT optimized lattice parameters of the $TiSi_2$ C49 structure (a=3.54 Å, b=13.54 Å, c=3.58 Å) are in excellent agreement with the experiment (a=3.56 Å, b=13.61 Å, c=3.56 Å).[5] The metal nanoparticle was modeled as a 38-atom cluster. Both the $TiSi_2$ b plane [the (010) surface] and the c plane [the (010) surface] were modeled as a six-layer slab. The nanoparticle was placed on top of the surface; the bottom three layers of the surface were fixed at their bulk positions. The adsorption energy, E_{ad}, is defined as $E_{ad} = E_{NP/TiSi2} - E_{NP} - E_{TiSi2}$, where $E_{NP/TiSi2}$, E_{NP}, and E_{TiSi2} are the energies of the adsorbed system, the isolated nanoparticle, and the clean $TiSi_2$ surface, respectively. So a negative E_{ad} indicates a favorable interaction.

DEMS Detection: For the Differential Electrochemical Mass Spec (DEMS) characterization, the cell was first discharged under 780 Torr pure O_2. The cell was then evacuated for 3 hours to remove O_2 in the chamber prior to DEMS characterization. The gas content was analyzed using a customized mass spectrometer with quadrupole rods mass analyzer (Microvision 2, MKS).

The cell was further studied in two ways – *in situ* and accumulation modes. For *in situ* analysis, the cell was connected to the Mass Spectrometer under vacuum with a dry rotary pump (nXDS 10i, Edwards) as the primary pump and a turbo pump to power the Mass Spectrometer. The cell was wired to a potentiostat (609D, CH Instruments) for galvanostatic recharging. For a typical *in situ* test, a constant current (500 mA/g_{Ru}) was applied to the cell and the gas generated was analyzed in

real time to obtain the profile of gas content at the different stages of recharge. Every MS scan was collected from 28 to 44 amu within 2s to give both the desired time resolution and accuracy.

For the Faradic efficiency test (accumulation mode), the cell was treated in the same way to generate an evacuated discharged cell as described above. The cell was then sealed and recharged (200 mA/g_{Ru}, 1000 mAh/g_{Ru}) to the capacity which matches that of the discharge. At the end of recharge, all gases generated were introduced to the MS at once with the same set up as described above, and O_2 (m/Z=32) signal was acquired and integrated to obtain the peak area. Calibration was performed by introducing a known amount of oxygen into the cell and carrying out the same data acquisition and analysis. A linear relationship between the peak area and amount of O_2 in the cell was established. The final Faradic efficiency was calculated by dividing the amount of O_2 detected in the MS by the theoretical value calculated from the charges passed to the cell.

Raman Characterization: Raman spectra were acquired using a micro-Raman system (XploRA, Horiba) with a 532nm laser excitation. Discharged/charged cell was first disassembled in an O_2 tolerated Argon filled glove box (dew point -100°C) and washed by pure anhydrous DME (Signal-Aldrich) three times. Then the cathode was assembled into a custom-made air-tight sample holder with a thin glass window. The discharged cathode was examined by Raman within the sample holder and no obvious peak of Li_2O_2 or Li_2CO_3 was detected. When the same sample was exposed to ambient air for several hours, significant Li_2CO_3 signal was observed on the same piece of sample. The fact that no Li_2O_2 signal was observed indicates that electrodeposited Li_2O_2 may be of poor crystallinity to produce significant Raman response. Once exposed to H_2O and CO_2 from ambient air, it was transformed to Li_2CO_3 that was easier to be detected.

XPS Characterization: Surface analysis was carried out using a K-Alpha XPS (Thermo Scientific) with Al K-alpha micro-focused monochromator. The beam spot size was 400μm. The sample was also washed by DME with the same procedure described above and mounted on the sample stage with minimal exposure to the ambient air before entering the load lock (on the order of minutes). The chamber was pumped down to 8×10^{-8} mbar prior to tests. Data were fitted by CasaXPS after correction by setting the internal reference C1s peak to 248.8eV. Li 1s peak of Li_2O_2 peak was assigned at 55.1 eV, that of LiOH was assigned at 54.3 eV, and that of Li_2CO_3 was assigned at 55.7 eV. The absolute values of these peaks may vary from different reports, but the relative position remained constant.

XPS was performed at the Center for Nanoscale Systems (CNS), a member of the National Nanotechnology Infrastructure Network (NNIN), which is supported by the National Science Foundation under NSF award no. ECS-0335765. CNS is part of Harvard University.

4.2 Results and Discussions

Modern technological developments have made electrical energy storage an indispensable need of the society. Existing battery technologies, Li-ion batteries being the state-of-the-art, do not meet our demands in terms of energy capacity and power density.[6] Significant research is required to bridge the gap. The capacity of batteries can be readily increased if we move away from intercalation chemistry that powers Li-ion batteries and turn to conversion reactions. Li-O_2 battery, enabled by the conversion between O_2 and Li_2O_2, is expected to offer one of the highest capacities. For this reason, it has received rapidly growing attention.[7-9] Before the potential of the Li-O_2 technology can be fully realized, however, a number of important issues must be addressed. At the center of these issues are the poor cyclability and low discharge/charge efficiency. It is recently

recognized that these issues are intimately connected to the electrode design, the choice of electrolyte, and their interactions.[10, 11] In particular, the widely used carbon support has been shown unstable under Li-O_2 operation conditions.[10, 12] Because the purported reversible Li_2O_2 formation and decomposition primarily takes place on the surface of the carbon cathode, the instability of carbon poses a significant challenge. The problem can in principle be solved by replacing carbon with other cathode materials.[13-15] Here we present $TiSi_2$ nanonet as a new, non-carbon cathode support that permits Li-O_2 operations for over 100 cycles with negligible performance degradation.

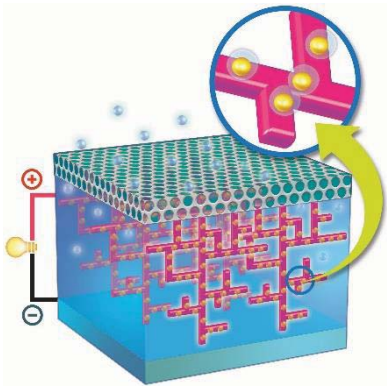

(**Figure 4.1** Schematic illustration of the overall design. Two-dimensional $TiSi_2$ nanonets are grown on a metal foam to be used directly as air cathode without binders or other additives. Ru nanoparticles (golden balls in the magnified view) preferably deposit on the b plans of $TiSi_2$. Li_2O_2 particles (semi-transparent spheres surrounding golden balls) form and decompose around Ru catalysts.)

As schematically shown in Figure 4.1, our design takes advantage of the high surface area (~100m^2/g)[16] and good conductivity (ρ~10μΩ·cm)[17] offered by the $TiSi_2$ nanonet.[18] Important to our design, the $TiSi_2$ nanonet exhibits no significant reactivity toward oxygen reduction or evolution when examined in the dimethoxyethane (DME) or tetra ethylene glycol dimethyl ether

(TEGDME) electrolyte systems (Figure 4.7 and 4.8). By comparison, many forms of carbon have proven catalytically active toward oxygen reduction reaction (ORR).[19] While the ORR reactivity may be perceived as an advantage because it helps reduce discharge overpotentials, the reactivity also creates a critical problem. For instance, on the one hand, carbon is susceptible to reactions with superoxide anion (O_2^-) that is an important intermediate during discharge,[20] leading to cathode erosion over repeated charge/discharge.[21] On the other hand, ORR activity by carbon produces Li_2O_2 products at locations away from oxygen evolution reaction (OER) catalysts, artificially increasing overpotentials necessary to decompose Li_2O_2 during recharge. This is because carbon only catalyzes ORR but not OER. As a result, high recharge potentials, especially toward the end of the recharge cycle, are required to fully decompose Li_2O_2. Electrolyte and carbon support are known to decompose at such high potentials.[10, 22] These negative influences can be mitigated by the application of a non-carbon cathode support that does not catalyze ORR. The $TiSi_2$ nanonet meets the need.

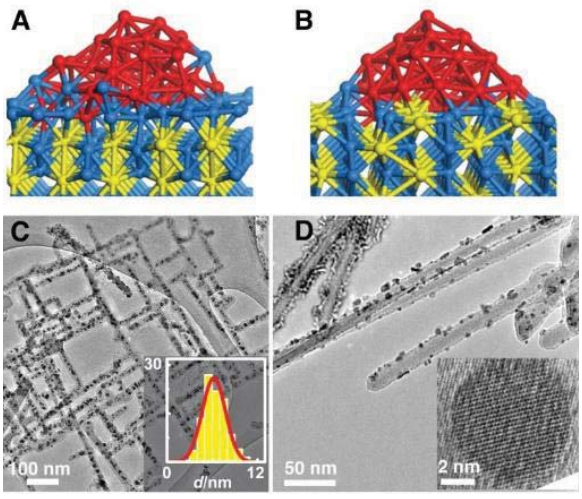

(**Figure 4.2** Site-selective growth of Ru nanoparticles on $TiSi_2$ nanonets. DFT calculations show that Ru clusters prefer the b planes (A) over the c planes of C49 $TiSi_2$ (B). The prediction is

consistent with experimental observations by TEM from the top (C), where b planes are parallel to the viewing direction. Inset: size distribution of Ru nanoparticles by a 100-cycle ALD growth. When viewed from the side (D), where b planes are perpendicular to the viewing direction, no Ru nanoparticles are seen on the c or a planes. Inset: high-resolution TEM confirming the crystalline nature of the Ru nanoparticles.)

To promote ORR, we chose to modify the surface of $TiSi_2$ with Ru nanoparticles. Less active than Pt and Pd but more so than Au in terms of ORR activities,[19] Ru costs much less than the other precious metals. Nanoparticles of Ru have been shown active toward ORR in nonaqueous systems as well.[14, 23, 24] More important, unlike Pt, Ru does not promote electrolyte decomposition.[25] For this proof-of-concept demonstration, Ru was grown on $TiSi_2$ by atomic layer deposition (ALD) to afford ligand-free surfaces for better catalytic activities. Intriguingly, site-selective growth was obtained, and Ru nanoparticles were observed only on the top and bottom surfaces of C49 $TiSi_2$ (Figure 4.2c and 4.2d), similar to our previous observations of Pt nanoparticle growth on the $TiSi_2$ nanonet.[26] To understand what governs the unique site-selectivity, we carried out density functional theory (DFT) calculations, where the metal was modeled as a 38-atom cluster and $TiSi_2$ was treated as a 6-layer slab (see Experimental Section in SI). After optimization, a strong mixing at the interface between Ru_{38} and C49 $TiSi_2$ is obvious (Figure 4.2a), suggesting greater interaction between the Ru nanoparticle and the Si layer of the b planes in $TiSi_2$. The degree of such interfacial interaction is much weaker in the a or c plane as evidenced in Figure 4.2b. The difference is quantified by the adsorption energy of the nanoparticle on the two $TiSi_2$ surfaces: -54 eV on the b-plane and -38 eV on the c-plane. The preferred adsorption of Ru onto the b-plane can also be viewed from the adhesion perspective. Using the area of the interface (ca. 110 Å), an adhesion energy of -7.8 J/m^2 is obtained for the Ru/$TiSi_2$-b-plane interface. This value is much higher than

the typical metal/silicide adhesion (e.g., -3.85 J/m^2 between Fe and $MoSi_2$).[27] Similar DFT results were obtained for the Pt/$TiSi_2$ system (Figure 4.16).[26] It is noted that the growth of Ru was not yet optimized in terms of size distribution (Figure 4.2c inset) because this proof-of-concept work is intended to examine the suitability of $TiSi_2$ nanonet as a support for Li-O_2 batter operations. Should it become necessary to achieve uniform size distribution, the system can be readily optimized by adjusting the ALD growth parameters, as has been shown in the case of bimetallic nanoparticles preparation reported by J. Elam et al.[28] It is also noted that the alloying between Ru and Si as shown in Figure 4.2 is not expected to significantly alter the electrochemical properties of the Ru catalyst as discussed next.

The activity of the Ru/$TiSi_2$ system was next characterized in DME electrolyte. For the first cycle upon discharge, a plateau at 2.65 V was obtained, corresponding to a kinetic overpotential of 0.31 V at 200mA/g_{Ru} (all capacities normalized to the mass loading of Ru, see SI for more details). When the polarity of current was switched, the recharge potential was first on a fast rising slope, reaching 3.39 V at 20% of the full discharged capacity. The potential increase slowed afterward, reaching a pseudo plateau with an average potential of 3.64 V between 20% and 100% of the full discharge capacity. At the end of the recharge cycle, a potential of 3.86 V was measured. Remarkably, the discharge plateau potential for the 100^{th} cycle was only 45 mV more negative than that of the 1^{st} cycle. The recharge plateau potential increased by 111 mV for the 100^{th} cycle when compared with the 1^{st} one. To quantify the round-trip efficiencies, the average recharge potential was divided by the average discharge one, and the data were plotted in Figure 4.3b. The round-trip efficiency was consistently greater than 70%, representing one of the highest in the literature.

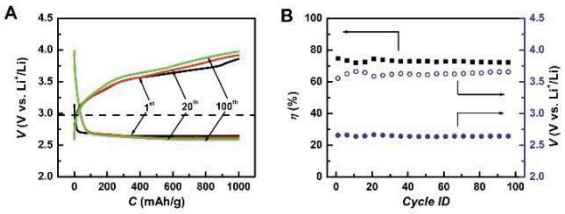

(**Figure 4.3** Electrochemical characterization of the Ru/$TiSi_2$ cathode in DME (0.1M $LiClO_4$). (A) Potential vs. Capacity plots of a cell during the 1st, 20th, and 100th cycle, respectively. The capacity was normalized to the mass of Ru catalysts. The dotted horizontal line marks the thermodynamic equilibrium potential of 2.96 V. (B) Average discharge (solid circle), recharge (hollow circle), and round-trip efficiencies over 100 cycles. For clarity, one data point for every 5 cycles is shown. (See Figure 4.17 for complete plots).)

It has been previously shown that the decomposition of the electrode or the electrolyte or both could yield discharge/charge characteristics similar to what is presented above. It is therefore of critical importance to confirm that the recorded performance was indeed a measure of the reversible conversion between O_2 and Li_2O_2. For this purpose, we next employed differential electrochemical mass spectrometry (DEMS), Raman spectroscopy, transmission electron microscopy (TEM), and X-ray photoelectron spectroscopy (XPS) to examine the products.

DEMS was set up to detect the recharge products. For a true reversible conversion of Li_2O_2, every 2 e^-'s passed would produce 1 gaseous O_2 molecule.[29] Other than O_2, CO_2 is a common by-product due to decomposition of carbonate, whose appearance would indicate undesired side reactions such as electrode or electrolyte decomposition that produce inorganic and organic carbonates. As is shown in Figure 4.4a, two O_2-production peaks were observed during recharge, one at ca. 20% of the full discharge capacity and the other at very late stage of recharge. Although the in situ O_2-

detection shown in Figure 4.4a does not take into account of the complex mass transport within the test cell and, as such, may not reflect the true instantaneous O_2 release characteristics, the two-stage decomposition of Li_2O_2 is qualitatively accurate. The characteristics are consistent with the mechanistic switch of the Li_2O_2 decomposition at different stages of recharge proposed by Shao-Horn et al.[30] The results that O_2 evolution happens at two voltages are also consistent with what has been reported by Bruce et al.[15] Important to our discussion, minimum CO_2 (the product of carbonate decomposition) was detected, supporting that carbonates formed during discharge/recharge were insignificant. The conclusion was later confirmed by Raman spectroscopy. It is noted that electrolyte (DME or TEGDME) instability is a known issue,[31] the decomposition of which produces carbonates. Because the cathode studied here is carbon free, any observed carbonate is likely a result of electrolyte decomposition.

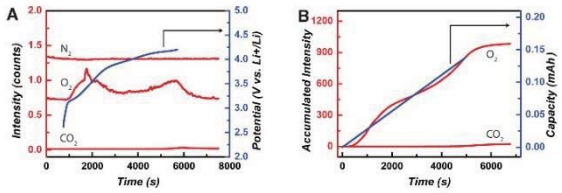

(**Figure 4.4** Detection of recharge products. (A) Real time mass spectrometry detection of gases generated at a fast 500 mA/g_{Ru} charging rate. (B) Accumulated counts of CO_2 and O_2. Data collected in 1.0M $LiClO_4$ in TEGDME.)

To ensure the measured O_2 was not a result of cell leakage from ambient air, N_2 was constantly monitored as an internal reference, which remained constant during the experiment (Figure 4.4a) supports the measured O_2 reflects Li_2O_2 decomposition. The total charge was obtained by integrating the calibrated intensity over time, and the result was plotted in Figure 4.4b. It is noted that the DEMS results were collected at a significantly higher charge rate (500 mA/g_{Ru}) than the

rate under which cyclability data were presented (200 mA/g_{Ru}). Fast rate was necessary to meet the real-time detection limit of the mass spectrometer used for this study. The actual cell used to measure the cyclability was studied at much slower discharge/charge rate. Using a separate injection method, we obtained a faradaic efficiency of 94.1% (see Experimental Section in SI). The result is quantitatively consistent with literature reports of O_2 detection by similar methods.[29] The detection establishes that the observed charge/discharge behavior was indeed a measure of Li_2O_2 formation and decomposition. By comparison, Ru/CB showed a poor rate capability. The test cell could only recover a small portion of discharged capacity during a fast recharge when the upper cut off voltage was limited to 4.2 V (used for $Ru/TiSi_2$ as shown in Figure 4.4a). When the upper cut-off voltage was increased to 4.5 V, significant CO_2 generation was detected (see SI). The comparison highlights the stability of the $Ru/TiSi_2$ system over Ru/C.

The formation of Li_2O_2 was directly observed by TEM (Figure 4.5a). Due to the known instability of Li_2O_2 under focused electron beams,[32] we were unable to study the crystallinity of the product. Nevertheless, particles of 20-30 nm in diameters were abundant (Figure 4.5a). The existence of Li_2O_2 was also confirmed by XPS. Upon recharge, the deconvoluted peak that can be assigned to Li_2O_2[33, 34] disappeared (Figure 4.5b). Because our XPS experiment involved a brief exposure of the samples to ambient air (see SI for experimental procedures), Li_2CO_3 was likely formed by reactions between Li_2O_2 and CO_2 during the exposure. Correspondingly, a Li_2CO_3 peak was persistent at all stages of the XPS characterizations (discharged and recharged, Figure 4.5b). As noted previously, the employment of a non-carbon cathode does not address instability issues of the electrolyte. Carbonate formation due to DME or TEMDME decomposition cannot be ruled out. It is another important reason why carbonates were observed in the XPS spectra.

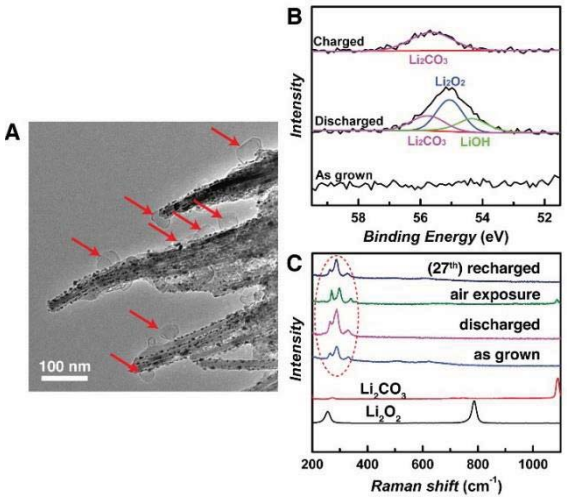

(**Figure 4.5** Product detection. (A) TEM showing the morphology of Li_2O_2 (highlighted by arrows). (B) Li 1s peaks of Ru/$TiSi_2$ cathode at different stages by XPS. (C) Raman spectra of Ru/$TiSi_2$ cathode at different stages. Reference spectra of Li_2O_2 and Li_2CO_3 of commercial samples are shown at the bottom. The peaks between 200 and 400 cm^{-1} (outlined by a dotted circle) are indicative of C49 $TiSi_2$.)

Lastly, we used Raman spectroscopy to identify the chemical nature of as-prepared, discharged, and recharged Ru/$TiSi_2$ samples, respectively. Our goal was to observe whether Li_2CO_3 formed during the reactions. As shown in Figure 4.5c, other than the sample exposed to ambient air, no Li_2CO_3 was seen, suggesting that no significant Li_2CO_3 formation or accumulation took place. We caution that the absence of Raman signals alone is inadequate to rule out the formation of Li_2CO_3. The conclusion is supported by our DEMS data presented earlier in this communication. The lack of Li_2CO_3 on the Ru/$TiSi_2$ sample is understood as a result of improved stability by the usage of a non-carbon cathode support. Our attempt to directly observe Raman signal corresponding to Li_2O_2 failed short. It is possible that the discharge products are of poor crystallinity under our test conditions (rate: 200mA/g_{Ru}). It is also possible that the electrochemically grown Li_2O_2 is

fundamentally different from the commercial Li_2O_2 reference used to generate Figure 4.5c.[35] It is noted that the lack of Li_2O_2 Raman peaks has been reported by other researchers as well and is not unique to our system.[36] The existence of Li_2O_2 may be indirectly confirmed by exposing the discharged sample to ambient air, which would produce Li_2CO_3 upon reaction with CO_2 and H_2O. This was indeed observed in our experiments (green trace in Figure 4.5c). Taken as a whole, the DEMS, TEM, XPS, and Raman characterizations collectively support that the electrochemical characteristics presented in Figure 4.3 are a reflection of reversible formation and decomposition of Li_2O_2. The long cyclability (>100 cycles) is among the best reported on any cathode materials in the literature.

4.3 Supplementary Information

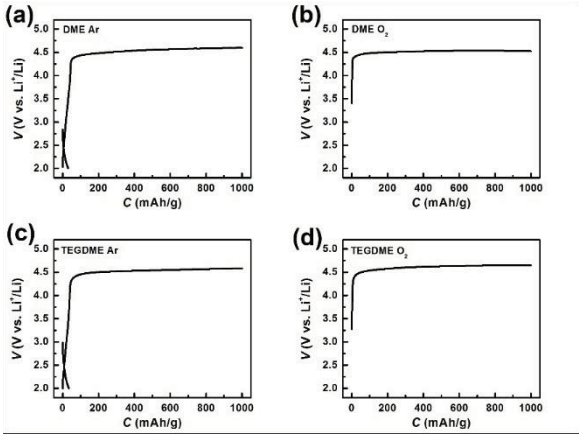

(**Figure 4.6** Stability of DME and TEGDME electrolyte. (a) Ru/$TiSi_2$ discharged and then recharged in DME, without O_2 (Ar environment); (b) Ru/$TiSi_2$ charged directly without discharge in DME O_2 environment; (c) Ru/$TiSi_2$ discharged and then recharged in TEGDME Ar environment; (b) Ru/$TiSi_2$ charged directly without discharge in TEGDME O_2 environment. Current density: 100mA/g_{Ru}. Negligible capacity was measured at potentials below 4.2 V, which is the condition

used for the characterization of $Ru/TiSi_2$ system in the main text, supporting that electrolyte decomposition should contribute little to the reported performance.)

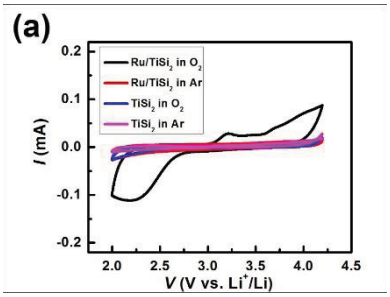

(**Figure 4.7** Cyclic Voltammetry of $TiSi_2$ and $Ru/TiSi_2$ in DME Electrolyte. Black and red curves are $Ru/TiSi_2$ in O_2 and Ar, respectively. Blue and purple curves are bare $TiSi_2$ in O_2 and Ar, respectively. It is observed from this set of data that $TiSi_2$ does not exhibit reactivity toward ORR or OER, while $Ru/TiSi_2$ are active toward both ORR and OER. We also see from this set of data that $Ru/TiSi_2$ does not induce measurable redox reactions in the absence of O_2.)

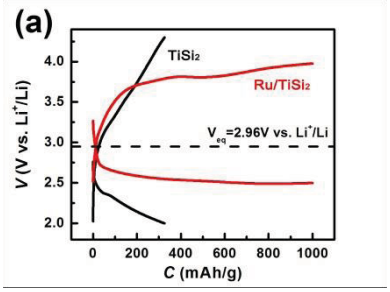

(**Figure 4.8** Electrochemical characterization of $TiSi_2$ cathode with and without Ru catalyst. Current density: $100mA/g_{TiSi2}$ and $100mA/g_{Ru}$ respectively. It can be seen that Ru as a catalyst is indispensable to the measured performance.)

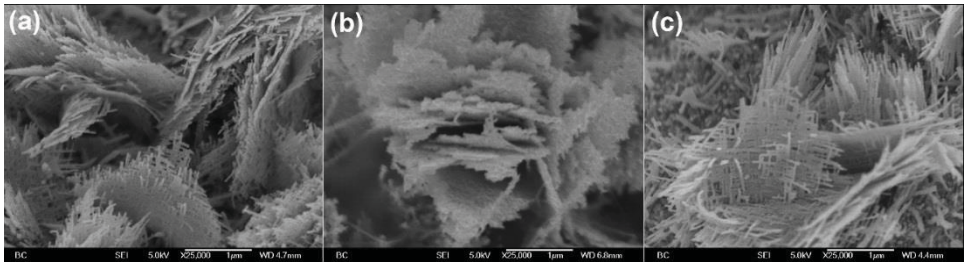

(**Figure 4.9** Structures of $Ru/TiSi_2$ heteronanostructures. (a) As-prepared $Ru/TiSi_2$; (b) $Ru/TiSi_2$ discharged for the 1st cycle; (c) $Ru/TiSi_2$ recharged for the 1st cycle)

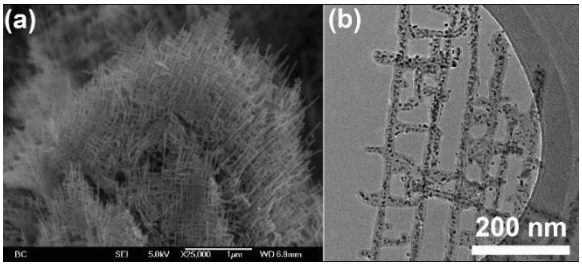

(**Figure 4.10** Structures of $Ru/TiSi_2$ heteronanostructures after 100 cycles. (a) SEM characterization; (b) TEM characterization. It can be seen that there was no observable erosion of the cathode material.)

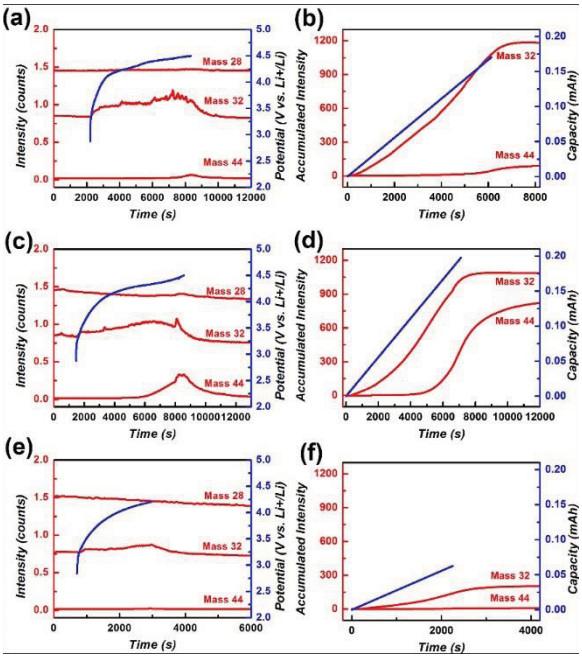

(**Figure 4.11** (a), (c), and (e) in-situ MS detection of gas generation at a fast 500mA/g charge rate for Carbon Black (up to 4.5 V vs. Li^+/Li), Ru/Carbon Black (up to 4.5 V vs. Li^+/Li), and Ru/Carbon Black (up to 4.2 V vs. Li^+/Li); (b), (d), and (f) accumulated counts of mass 32 and mass 44 species for above samples. Unless the upper cut-off voltage is set below 4.2 V, CO_2 formation is significant. This set of data supports that carbon support participates in the carbonate formation significantly.)

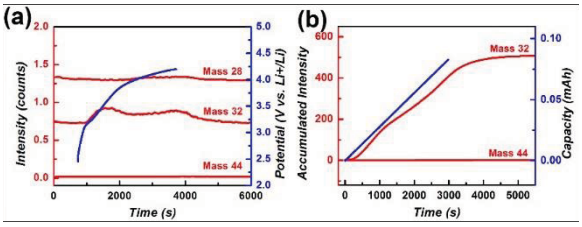

(**Figure 4.12** (a) in-situ MS detection of gas generation at a fast 500mA/g charging rate for $Ru/TiSi_2$ (up to 4.2 V vs. Li^+/Li, after 5 cycles); (b) accumulated counts of mass 32 and mass 44 species. After 5 cycles of repeated discharge/recharge, no significant CO_2 formation is measured.)

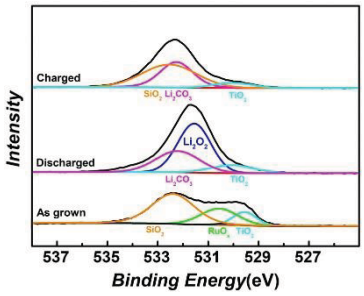

(**Figure 4.13** O 1s peak spectra of as grown, discharged and charged cathodes. The results are consistent with the Li 1s data as shown in the main text.)

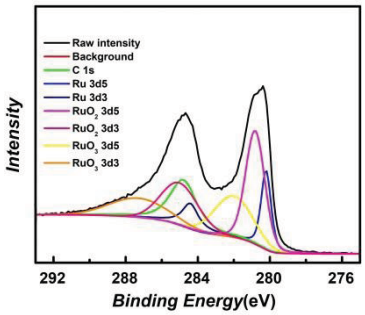

(**Figure 4.14** C 1s and Ru 3d spectra of as grown cathode.)

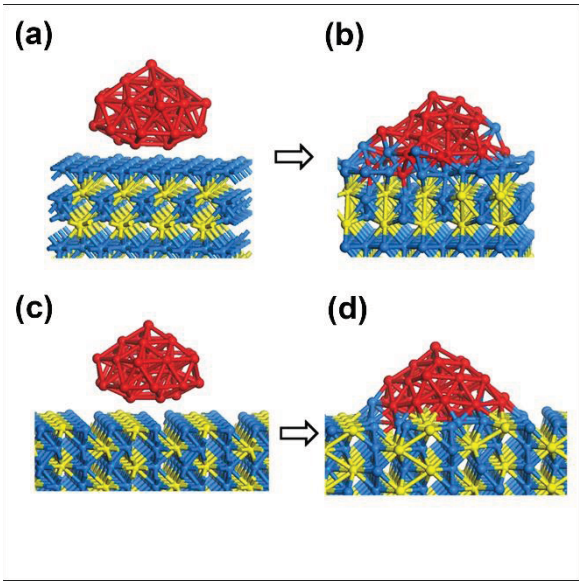

(**Figure 4.15** Initial (a) and final (b) states of the Ru38 nanoparticle on the b-plane of the $TiSi_2$ C49 structure; initial (c) and final (d) states of the Ru38 nanoparticle on the c-plane of the $TiSi_2$ C49 structure. Ru, red; Si, blue; Ti, yellow. The adsorption energy of the nanoparticle on the two $TiSi_2$ surfaces: -54 eV on the b-plane and -38 eV on the c-plane.)

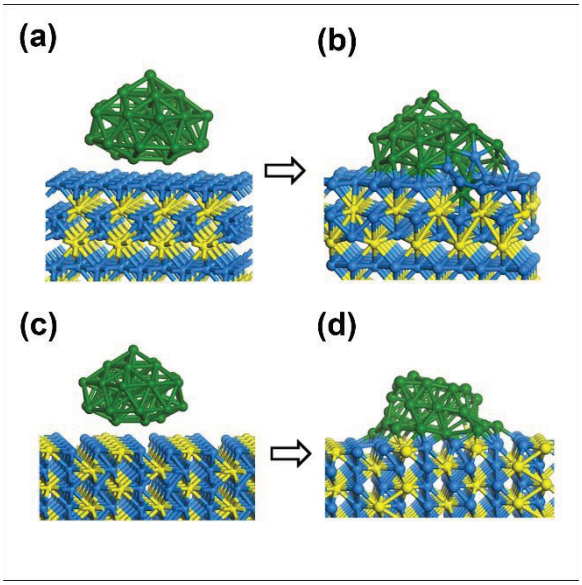

(**Figure 4.16** Initial (a) and final (b) states of the Pt38 nanoparticle on the b-plane of the $TiSi_2$ C49 structure; initial (c) and final (d) states of the Pt38 nanoparticle on the c-plane of the $TiSi_2$ C49 structure. Pt, green; Si, blue; Ti, yellow. The adsorption energy of the nanoparticle on the two $TiSi_2$ surfaces: -49 eV on the b-plane and -40 eV on the c-plane.)

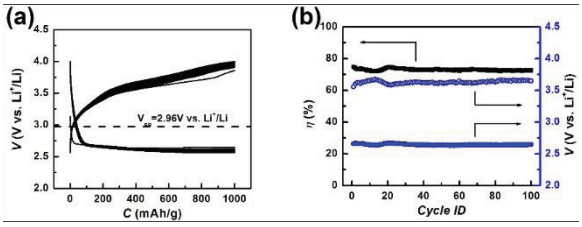

(**Figure 4.17** Electrochemical characterization of the $Ru/TiSi_2$ cathode in DME (0.1M $LiClO_4$). (A) Potential vs. Capacity plots of a cell from 1st cycle to 100th cycle. The dotted horizontal line marks the thermodynamic equilibrium potential of 2.96 V between reversible Li^+ and Li_2O_2 conversion. (B) Average discharge (solid circle), recharge (hollow circle), and round-trip efficiencies over 100 cycles.)

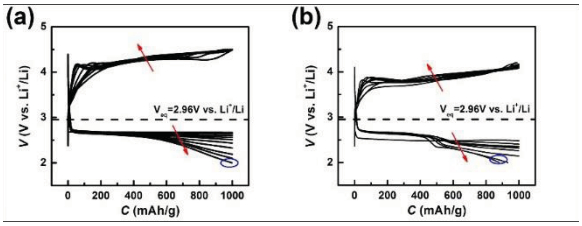

(**Figure 4.18** Electrochemical characterization of the carbon based cathode in DME (0.1M $LiClO_4$). (a) Potential vs. Capacity plots of Carbon black cathode for first 11 cycles. (b) Potential vs. Capacity plots of Ru/Carbon black cathode for first 9 cycles. All capacities were normalized to weight of Carbon black. Bare Carbon black and Ru/Carbon Black samples failed to reach the set capacity of 1000 mAh/g_C before reaching the cut off voltage of 2.0V at 11th cycles and 9th cycles,

respectively. During the initial serveral cycles, significant side reactions took place and caused the overpotnetial to increase.)

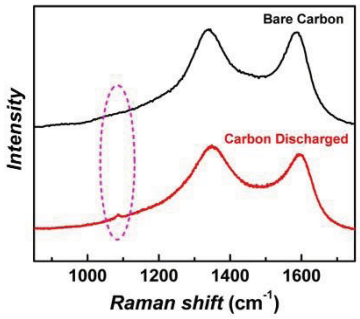

(**Figure 4.19** Raman characterizations of pristine Carbon black cathode (black) and discharge Carbon black cathode after cycles (red) within air-tight container. A small Li_2CO_3 peak was observed after discharge.)

4.4 Conclusions

Reversible formation and decomposition of Li_2O_2 is key to successful operation of a rechargeable aprotic Li-O_2 cell. As an important step toward this goal, we presented Ru nanoparticles-decorated $TiSi_2$ nanonet as a new cathode system. Compared with the popularly used carbon support, $TiSi_2$ nanonet is advantageous in that it does not show measurable reactivity toward reaction intermediates such as superoxide ions. As a result, long cyclability (>100 cycles) with confirmed Li_2O_2 formation and decomposition was obtained. The new cathode system is expected to play positive roles in fundamental understandings of electrolyte stability as well because of its inert nature.

4.5 References

(1) Kresse, G.; Furthmuller, J. Efficient Iterative Schemes for Ab Initio Total-Energy Calculations Using a Plane-Wave Basis Set. *Phys. Rev. B* **1996**, *54*, 11169-11186.

(2) Kresse, G.; Furthmuller, J. Efficiency of Ab-Initio Total Energy Calculations for Metals and Semiconductors Using a Plane-Wave Basis Set. *Comput. Mater. Sci.* **1996**, *6*, 15-50.

(3) Kresse, G.; Joubert, D. From Ultrasoft Pseudopotentials to the Projector Augmented-Wave Method. *Phys. Rev. B* **1999**, *59*, 1758-1775.

(4) Perdew, J. P.; Burke, K.; Ernzerhof, M. Generalized Gradient Approximation Made Simple. *Phys. Rev. Lett.* **1996**, *77*, 3865-3868.

(5) Beyers, R.; Sinclair, R. Metastable Phase Formation in Titanium-Silicon Thin-Films. *J. Appl. Phys.* **1985**, *57*, 5240-5245.

(6) Choi, N.-S.; Chen, Z.; Freunberger, S. A.; Ji, X.; Sun, Y.-K.; Amine, K.; Yushin, G.; Nazar, L. F.; Cho, J.; Bruce, P. G. Challenges Facing Lithium Batteries and Electrical Double-Layer Capacitors. *Angew. Chem. Int. Ed.* **2012**, *51*, 9994-10024.

(7) Girishkumar, G.; McCloskey, B.; Luntz, A. C.; Swanson, S.; Wilcke, W. Lithium-Air Battery: Promise and Challenges. *J. Phys. Chem. Lett.* **2010**, *1*, 2193-2203.

(8) Bruce, P. G.; Freunberger, S. A.; Hardwick, L. J.; Tarascon, J. M. Li-O_2 and Li-S Batteries with High Energy Storage. *Nature Mater.* **2012**, *11*, 19-29.

(9) Lu, Y. C.; Gallant, B. M.; Kwabi, D. G.; Harding, J. R.; Mitchell, R. R.; Whittingham, M. S.; Shao-Horn, Y. Lithium-Oxygen Batteries: Bridging Mechanistic Understanding and Battery Performance. *Energy Environ. Sci.* **2013**, *6*, 750-768.

(10) Ottakam Thotiyl, M. M.; Freunberger, S. A.; Peng, Z.; Bruce, P. G. The Carbon Electrode in Nonaqueous Li-O_2 Cells. *J. Am. Chem. Soc.* **2013**, *135*, 494-500.

(11) Lu, J.; Lei, Y.; Lau, K. C.; Luo, X. Y.; Du, P.; Wen, J. G.; Assary, R. S.; Das, U.; Miller, D. J.; Elam, J. W.; Albishri, H. M.; Abd El-Hady, D.; Sun, Y. K.; Curtiss, L. A.; Amine, K. A Nanostructured Cathode Architecture for Low Charge Overpotential in Lithium-Oxygen Batteries. *Nat. Commun.* **2013**, *4*, 2383.

(12) McCloskey, B. D.; Speidel, A.; Scheffler, R.; Miller, D. C.; Viswanathan, V.; Hummelshoej, J. S.; Noerskov, J. K.; Luntz, A. C. Twin Problems of Interfacial Carbonate Formation in Nonaqueous Li-O_2 Batteries. *J. Phys. Chem. Lett.* **2012**, *3*, 997-1001.

(13) Peng, Z.; Freunberger, S. A.; Chen, Y.; Bruce, P. G. A Reversible and Higher-Rate Li-O_2 Battery. *Science* **2012**, *337*, 563-566.

(14) Li, F.; Tang, D.-M.; Chen, Y.; Golberg, D.; Kitaura, H.; Zhang, T.; Yamada, A.; Zhou, H. Ru/ITO: A Carbon-Free Cathode for Non-aqueous Li-O_2 Battery. *Nano Lett.* **2013**, *13*, 4702-4707.

(15) Ottakam Thotiyl, M. M.; Freunberger, S. A.; Peng, Z.; Chen, Y.; Liu, Z.; Bruce, P. G. A Stable Cathode for the Aprotic Li-O_2 Battery. *Nature Mater.* **2013**, *12*, 1050-1056.

(16) Lin, Y.; Zhou, S.; Liu, X.; Sheehan, S.; Wang, D. TiO_2/$TiSi_2$ Heterostructures for High-Efficiency Photoelectrochemical H_2O Splitting. *J. Am. Chem. Soc.* **2009**, *131*, 2772-2773.

(17) Zhou, S.; Liu, X.; Lin, Y.; Wang, D. Spontaneous Growth of Highly Conductive Two-Dimensional Single-Crystalline $TiSi_2$ Nanonets. *Angew. Chem. Int. Ed.* **2008**, *47*, 7681-7684.

(18) Zhou, S.; Yang, X.; Xie, J.; Simpson, Z. I.; Wang, D. Titanium Silicide Nanonet as a New Material Platform for Advanced Lithium-Ion Battery Applications. *Chem. Commun.* **2013**, *49*, 6470-6476.

(19) Lu, Y.-C.; Gasteiger, H. A.; Shao-Horn, Y. Catalytic Activity Trends of Oxygen Reduction Reaction for Nonaqueous Li-Air Batteries. *J. Am. Chem. Soc.* **2011**, *133*, 19048-19051.

(20) Yang, J.; Zhai, D.; Wang, H.-H.; Lau, K. C.; Schlueter, J. A.; Du, P.; Myers, D. J.; Sun, Y.-K.; Curtiss, L. A.; Amine, K. Evidence for Lithium Superoxide-Like Species in the Discharge Product of a Li-O_2 Battery. *Phys. Chem. Chem. Phys.* **2013**, *15*, 3764-3771.

(21) Gallant, B. M.; Mitchell, R. R.; Kwabi, D. G.; Zhou, J.; Zuin, L.; Thompson, C. V.; Shao-Horn, Y. Chemical and Morphological Changes of Li-O_2 Battery Electrodes upon Cycling. *J. Phys. Chem. C* **2012**, *116*, 20800-20805.

(22) McCloskey, B. D.; Valery, A.; Luntz, A. C.; Gowda, S. R.; Wallraff, G. M.; Garcia, J. M.; Mori, T.; Krupp, L. E. Combining Accurate O_2 and Li_2O_2 Assays to Separate Discharge and Charge Stability Limitations in Nonaqueous Li-O_2 Batteries. *J. Phys. Chem. Lett.* **2013**, *4*, 2989-2993.

(23) Jung, H.-G.; Jeong, Y. S.; Park, J.-B.; Sun, Y.-K.; Scrosati, B.; Lee, Y. J. Ruthenium-Based Electrocatalysts Supported on Reduced Graphene Oxide for Lithium-Air Batteries. *ACS Nano* **2013**, *7*, 3532-3539.

(24) Li, F.; Chen, Y.; Tang, D.-M.; Jian, Z.; Liu, C.; Golberg, D.; Yamada, A.; Zhou, H. Performance-Improved Li-O_2 Battery with Ru Nanoparticles Supported on Binder-Free Multi-Walled Carbon Nanotube Paper as Cathode. *Energy Environ. Sci.* **2014**, *7*, 1648-1652.

(25) Harding, J. R.; Lu, Y.-C.; Tsukada, Y.; Yang, S.-H. Evidence of Catalyzed Oxidation of Li_2O_2 for Rechargeable Li-Air Battery Applications. *Phys. Chem. Chem. Phys.* **2012**, *14*, 10540-10546.

(26) Xie, J.; Yang, X.; Han, B.; Shao-Horn, Y.; Wang, D. Site-Selective Deposition of Twinned Platinum Nanoparticles on $TiSi_2$ Nanonets by Atomic Layer Deposition and Their Oxygen Reduction Activities. *ACS Nano* **2013**, *7*, 6337-6345.

(27) Jiang, D. E.; Carter, E. A. Prediction of Strong Adhesion at the $MoSi_2$/Fe Interface. *Acta Mater.* **2005**, *53*, 4489-4496.

(28) Lu, J. L.; Low, K. B.; Lei, Y.; Libera, J. A.; Nicholls, A.; Stair, P. C.; Elam, J. W. Toward Atomically-Precise Synthesis of Supported Bimetallic Nanoparticles Using Atomic Layer Deposition. *Nat. Commun.* **2014**, *5*, 3264.

(29) McCloskey, B. D.; Bethune, D. S.; Shelby, R. M.; Girishkumar, G.; Luntz, A. C. Solvents' Critical Role in Nonaqueous Lithium-Oxygen Battery Electrochemistry. *J. Phys. Chem. Lett.* **2011**, *2*, 1161-1166.

(30) Gallant, B. M.; Kwabi, D. G.; Mitchell, R. R.; Zhou, J.; Thompson, C. V.; Shao-Horn, Y. Influence of Li_2O_2 Morphology on Oxygen Reduction and Evolution Kinetics in Li-O_2 Batteries. *Energy Environ. Sci.* **2013**, *6*, 2518-2528.

(31) Freunberger, S. A.; Chen, Y.; Drewett, N. E.; Hardwick, L. J.; Barde, F.; Bruce, P. G. The Lithium-Oxygen Battery with Ether-Based Electrolytes. *Angew. Chem. Int. Ed.* **2011**, *50*, 8609-8613.

(32) Zhong, L.; Mitchell, R. R.; Liu, Y.; Gallant, B. M.; Thompson, C. V.; Huang, J. Y.; Mao, S. X.; Shao-Horn, Y. In Situ Transmission Electron Microscopy Observations of Electrochemical Oxidation of Li_2O_2. *Nano Lett.* **2013**, *13*, 2209-2214.

(33) Lei, Y.; Lu, J.; Luo, X.; Wu, T.; Du, P.; Zhang, X.; Ren, Y.; Wen, J.; Miller, D. J.; Miller, J. T.; Sun, Y.-K.; Elam, J. W.; Amine, K. Synthesis of Porous Carbon Supported Palladium Nanoparticle Catalysts by Atomic Layer Deposition: Application for Rechargeable Lithium-O_2 Battery. *Nano Lett.* **2013**, *13*, 4182-4189.

(34) Younesi, R.; Hahlin, M.; Bjorefors, F.; Johansson, P.; Edstrom, K. Li-O_2 Battery Degradation by Lithium Peroxide (Li_2O_2): A Model Study. *Chem. Mater.* **2013**, *25*, 77-84.

(35) Yilmaz, E.; Yogi, C.; Yamanaka, K.; Ohta, T.; Byon, H. R. Promoting Formation of Noncrystalline Li_2O_2 in the Li-O_2 Battery with RuO_2 Nanoparticles. *Nano Lett.* **2013**, *13*, 4679-4684.

(36) Zhai, D.; Wang, H.-H.; Yang, J.; Lau, K. C.; Li, K.; Amine, K.; Curtiss, L. A. Disproportionation in Li-O_2 Batteries Based on a Large Surface Area Carbon Cathode. *J. Am. Chem. Soc.* **2013**, *135*, 15364-15372.

Chapter 5 Protected 3DOm Carbon for Lithium Oxygen Batteries

This chapter is adapted from: Xie, J.; Yao, X.; Cheng, Q.; Madden, I. P.; Dornath, P.; Chang, C.-C.; Fan, W.; Wang, D. Three Dimensionally Ordered Mesoporous Carbon as a Stable, High-Performance Li-O_2 Battery Cathode. *Angew. Chem. Int. Ed.* **2015**, *127*, 4373-4377.

Enabled by the reversible conversion between Li_2O_2 and O_2, Li-O_2 batteries promise theoretical gravimetric capacities significantly greater than Li-ion ones. The poor cycling performance, however, has greatly hindered the development of this technology. At the heart of the problem is the reactivity exhibited by carbon cathode support under cell operation conditions. One strategy is to conceal the carbon surface from reactive intermediates. Here we show that long cyclability can indeed be achieved on three-dimensionally ordered mesoporous (3DOm) carbon by growing a thin layer of FeO_x using atomic layer deposition (ALD). 3DOm carbon distinguishes itself from other carbon materials with well-defined pore structures, providing a unique material platform for fundamental understandings of processes important to Li-O_2 battery operations. When decorated with Pd nanoparticle catalysts, also prepared by ALD, the new cathode exhibits a capacity >6000 mAh/g_{carbon} and cyclability >68 cycles.

5.1 Experimental Details

Material synthesis: 3DOm carbons were made by following the method reported in literature.[1, 2] A precursor solution made of furfuryl alcohol and oxalic acid with a weight ratio of 200:1 was

impregnated within silica colloidal crystal templates composed of highly monodisperse 12 or 35 nm silica nanoparticles (SNPs). The resulting samples were heated to 70 ^{o}C for 2 days to polymerize furfuryl alcohol, followed by heating at 200 ^{o}C in flowing N_2 for 3 h to cure the polymer, and then heated at 900 ^{o}C for an additional 2 h to carbonize the samples. The SNPs were dissolved in 6 M KOH solution at 150 ^{o}C for 2 days to yield 3DOm carbon replica. The resulting carbon material was then thoroughly washed with 70 °C deionized water until the resulting solution was near neutral. Finally, the 3DOm carbon was dried at 70 ^{o}C for 24 h.

Carbon and polytetrafluoroethylene (PTFE) were mixed in isopropyl alcohol (IPA) with a mass ratio of 8:2. The mixture was dispersed by sonication and coated on the Ni foam (1.6mm in thickness originally, MTI Corp.). The electrode was further dried in vacuum oven overnight to remove the residual solvent.

The growth of FeO_x has been reported by us previously.[3-5] The as-prepared carbon electrodes were placed in the ALD (Savannah S100, Ultratech/CambridgeNanoTech) chamber and heated to 180 °C. Iron *tert*-butoxide ($Fe_2(^{t}BuO)_6$) and water were employed as precursors at 120 °C and 25 °C, respectively. Each cycle of the growth followed the repeated sequence of 3 s Fe precursor pulse, 60 s Fe precursor diffusion/adsorption/reaction, 90 s N_2 purging; 0.05 s water pulse, 60 s water precursor diffusion/adsorption/reaction, and another 90s N_2 purging. A typical growth lasts 50 cycles to yield desired coating of FeO_x of ca. 1.4 nm in thickness.

Pd nanoparticles were deposited using ALD as well. The growth temperature was 250 °C, with $Pd(hfac)_2$ (Palladium(II) hexafluoroacetylacetonate, 60 °C) and formalin (37 wt% in H_2O, 25 °C)

as precursors. Each cycle consisted of 5 repeated pulse/purge sub-cycles of $Pd(hfac)_2$ and formalin for sufficient surface adsorption in the high aspect ratio 3DOm carbon.

The loading quantity was examined by microbalance (Sartorius, CPA2P). The resulting loading of carbon on Ni foam (15-30mg per piece) varied between 0.5mg/cm^2 to 1mg/cm^2. The weight ratio of FeO_x:C and Pd:C was measured as 1:5 and 1:10, respectively.

Electrochemical characterization: $LiClO_4$ in dimethoxyethane (0.1 M) was used as purchased from Novolyte (BASF) with water level <10 ppm. Tetraethylene glycol dimethyl ether (TEGDME, ≥ 99%, Sigma-Aldrich) was first stored over freshly activated 4 Å molecular sieves and then distilled. The distilled TEGDME was stored over molecular sieves before usage. $LiClO_4$ (99.99%, Battery grade, Sigma-Aldrich) was baked at 130 °C in a vacuum oven within the glove box and mixed with TEGDME to generate the 1 M electrolyte solution. Customized Swagelok^{TM} type cells were assembled in the glove box (H_2O and O_2 levels < 0.1 ppm, MBraun) with Li metal(380μm in thickness, Sigma-Aldrich) as the anode, Celgard 2400 films as the separator, 100 to 200μL 0.1 M $LiClO_4$ in DME or 1.0 M $LiClO_4$ in TEGDME as the electrolyte. Batteries were studied using potentiostats (VMP3, Bio-Logic).

For DEMS characterization, the cell was first discharged in TEGDME under pure O_2 to a given capacity. The discharged cell was then evacuated for 5 h to remove remaining O_2. For *in situ* analysis, the cell was connected to the mass spectrometer with a dry rotary pump (nXDS 10i, Edwards) as the differential pump. The cell was wired to a potentiostat (609D, CH Instruments) for galvanostatic recharging, while gas content was analyzed using a customized mass spectrometer

with quadrupole mass analyzer (Microvision 2, MKS). Each scan was collected from 28 to 44 amu within 3 s to give desired time resolution and accuracy.

Material characterization: Scanning electron microscopy (SEM) images were taken on a JEOL 6340F microscope and TEM were performed on a JEOL 2010F microscope operated at 200 kV. X-ray diffraction (XRD) measurements were performed on PANalytical X'Pert Pro diffractometer with Cu Kα radiation. The cell was first transferred to an O_2-toleranted Ar-filled glove box (H_2O level < 0.1 ppm, MBraun) and disassembled inside to extract the cathode, which was then rinsed with pure anhydrous DME (Sigma-Aldrich) for 3 times to remove remaining salts. An airtight sample holder with an X-ray transparent Kapton film window was used to transfer the sample and carry out XRD characterizations without exposing the sample to the ambient air. Raman spectra and mapping were acquired using a micro-Raman system (XploRA, Horiba) with a 532nm laser excitation. The N_2 adsorption/desorption experiments were carried out on an automatic gas sorption analyzer (Autosorb iQ, Quantachrome) at 77 K. The pore size distribution and cumulative pore volume were obtained by applying a built-in quenched state density functional theory (QSDFT) adsorption model with cylindrical/spherical configuration for carbon (ASiQwin v3.0, Quantachrome). Surface analysis was carried out using a K-Alpha XPS (Thermo Scientific). The sample was also washed by DME with the same procedure as described above and mounted on the sample stage with a short exposure to the ambient air (typically <5 min) before entering the load lock. XPS data was calibrated by adventitious carbon at 284.8eV and fitted using XPS Peak 4.1 software. For example, for oxygen species, linear background was subtracted and mixed Lorentzian-Gaussian shape peaks were adopted, peak positions for different oxygen species were adopted from previous literature reports.

5.2 Results and Discussions

Metal-air battery has been studied for decades, with the interest in Li-O_2 battery intensified recently for its potentially high gravimetric capacities.[6-9] The key to successful operation of a Li-O_2 battery is the control over Li_2O_2 formation and its decomposition. Many of the observed failing mechanisms are connected to these two processes.[10, 11] For instance, discharge products other than Li_2O_2 are often found difficult to decompose upon recharge, leading to fast capacity fading. Side reactions other than Li_2O_2 formation and decomposition degrade the electrode or the electrolyte or both.[12, 13] Synergistic effects between carbon support and the electrolyte have been recently recognized to contribute to these side reactions.[14] Existing reports on details of Li_2O_2 formation concerning, for example, their sizes, morphologies, and crystallinity vary, making it difficult to draw a unified understanding of the key processes involved in Li-O_2 battery operations.[15-18] The issue is compounded in part by the poorly defined pore structures and surfaces of carbon support reported to date. It becomes clear that detailed studies of Li_2O_2 formation and decomposition on a cathode support of well-defined structures and surfaces should be of great value.[19-22] Within this context, 3DOm carbon, an inverse replica of face-centered-cubic (FCC) close-packed structures (Figure 5.1a), presents a unique opportunity to understand Li-O_2 battery operations.[23, 24]

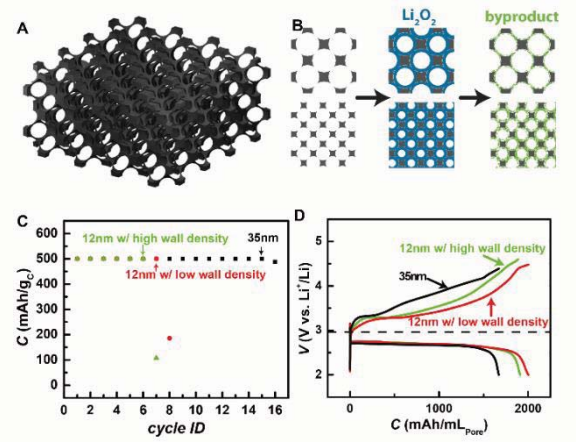

(**Figure 5.1** Structure and cycling performance of 3DOm carbon with well-defined pore sizes. A. The structure is represented by a three-dimensional model, where only the large pores are shown. B. In a simplified two-dimensional representation, the formation and accumulation of by-products are shown here. Undesired byproducts accumulate faster on 3DOm carbon with small pores (bottom panels) than large ones (top panels). Left: pristine carbon; middle: with discharge product (Li_2O_2); right: after recharge, where green deposits represent byproducts that cannot be easily decomposed. C. Cycling performance of bare 3DOm carbon of different pore sizes. The capacity is limited to 500 mAh/g_{carbon}; rate: 100 mA/g_{carbon}. Data legend: 3DOm carbon of 35 nm pores in black square; 12 nm pores with high wall density in green triangle; 12 nm pores with low wall density in red circle. D. Discharge/charge behaviors normalized to pore volumes. The only constraint set during test was the discharge potential, ≥2 V (vs. Li^+/Li).)

The size of pores and windows connecting the pores in the 3DOm carbon can be independently tailored as has been reported previously.[23] This feature makes 3DOm carbon distinctly different from other carbon support (e.g., super P or Vulcan carbon) where well-defined pores in the range of tens of nanomaterials are not available.[25, 26] In this regard, 3DOm carbon also distinguishes itself from carbon nanotubes whose sidewalls are essentially open spaces.[27] Similarly, spaces between randomly arranged graphene (and other graphene derivatives including reduced graphene oxides) are also less than uniform.[28] To demonstrate what the well-defined pores enable, we next study how the cyclability depends on the pore sizes. Our understanding as depicted in Figure 5.1b is based on the following assumptions. First, side-reactions other than Li_2O_2 formation and decomposition on the surfaces of carbon are inevitable during Li-O_2 battery operations.[29] Second, these reactions result in accumulation of by-products that will eventually clog the pores of 3DOm carbon.[10, 12, 30] Third, once the pores are clogged, the volume accessible for Li_2O_2 deposition drops

dramatically to result in cell failure. Since smaller pores correspond to greater surface-to-volume ratios, they will be clogged more easily than bigger pores. We therefore expect poorer cyclability on 3DOm carbon of smaller pores. The expectation was indeed verified in Figure 5.1c. Even by limiting the discharge capacity to a modest 500 mAh/g_{carbon}, less than 10% of the total achievable capacities, we observed severe capacity fading by the 15th cycle of recharge for 3DOm carbon of 35 nm pores. Poorer cycling performance was witnessed on 3DOm carbon of smaller pores (6th to 7th cycle for 12 nm pores, see Figure 5.1c and Figure 5.9).

As far as capacity is concerned, we expect it only depends on the accessible mesopores (i.e., pores defined by the silica beads) but not the micropores in the carbon walls (d≤2 nm). This is because the micropores are too small to support Li_2O_2 deposition. Indeed, upon deep discharge, the capacities normalized to the volumes specific to the large pores as shown in Figure 5.1d are comparable (1700 mAh/mL_{pore} for 35 nm and 2000 mAh/mL_{pore} for 12 nm 3DOm carbon; see Figure 5.5, 5.6 and Table 5.1). Most strikingly, we see negligible difference between the capacities measured on 3DOm carbon of similar pore sizes (ca. 12 nm) but different micropore volumes (green and red traces in Figure 5.1d), strongly supporting that micropores do not contribute to the capacities.

Next, we seek to address an important concern in using carbon support for Li-O_2 battery operations – the reactivity of carbon.[31] Increasing evidence suggests that carbon is unstable against O_2^- during discharge.[29] Carbon is also reactive under high recharge potentials.[14, 30] Our strategy to address the issue is to physically separate carbon surface from Li_2O_2, any reaction intermediates, as well as the electrolyte. The goal is achieved by growing a thin, uniform layer of metal oxides on 3DOm carbon (Figure 5.2a). Thanks to the synthesis procedures of 3DOm carbon, its surface is inherently

hydrophilic, ideal for growing oxides by atomic layer deposition (ALD). ALD growth has the benefit of affording complete coverage with minimum defects. In this study, we demonstrate that amorphous FeO_x as an effective protection layer. The uniformity of the FeO_x growth is confirmed by the following experiments. First, Brunauer-Emmett-Teller (BET) pore size measurements as shown in Figure 5.2b clearly verify that the average pore sizes have been reduced from 33.0 nm to 30.2 nm, corresponding to a wall thickness of 1.4 nm for FeO_x, consistent with what is expected from a 50-cycle ALD growth. Second, the bright field transmission electron micrographs (TEM) before and after the ALD treatment (Figure 5.2c) unambiguously confirm the deposition of FeO_x. Lastly, the existence and distribution of FeO_x can be visualized by Raman mapping (supporting information, Figure 5.7). Taken as a whole, the BET measurements, TEM micrographs, and Raman mapping confirm that the coverage of FeO_x on carbon is uniform. The uniform FeO_x coating is expected to provide a desired protection to minimize side reactions inherent to bare carbon surfaces.

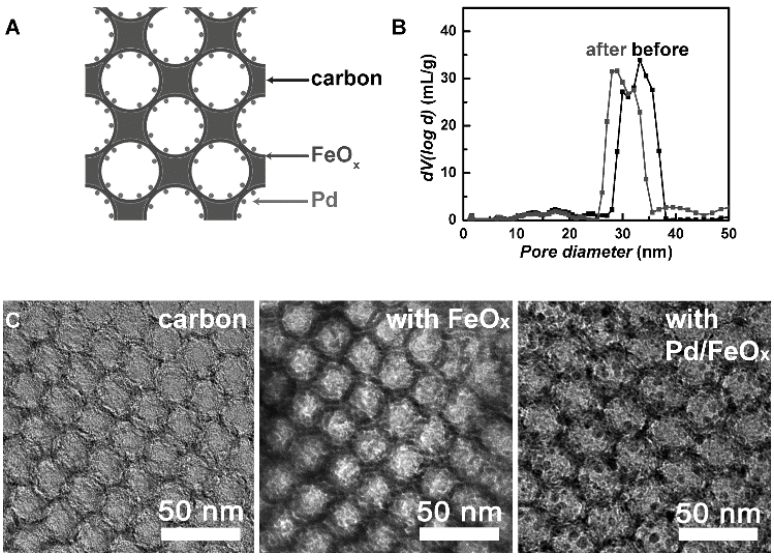

(**Figure 5.2** Protection of 3DOm carbon by FeO_x and decoration with Pd nanoparticle catalysts. A. The design is schematically shown. B. Pore volume measurements confirm a uniformly pore

diameter reduction from 33.0 nm to 30.2 nm. C. The deposition is clearly seen from the transmission electron micrographs. Left: bare 3DOm carbon; middle: after FeO_x deposition; right: after Pd deposition.)

The separation of carbon surface from reaction intermediates serves another important purpose. It hinders the well-recognized oxygen reduction reactions (ORR) activities of carbon. At the first glance, this may seem counterintuitive. After all, the first step of Li-O_2 battery discharge is to reduce oxygen. As such, the ORR activity of carbon would be a beneficial property. However, as shown in Figure 5.3a (upper panel), the ORR activity of carbon promotes Li_2O_2 formation randomly on the surface of carbon, at or away from oxygen evolution reactions (OER) sites. Note that OER catalysts are necessary to decompose Li_2O_2 at relatively low recharge overpotentials.[32] Li_2O_2 reside far away from OER sites are difficult to decompose, increasing the need for overpotentials and driving up the recharge potentials. Even worse, they may remain during the following cycles, accumulate, and eventually lead to capacity fading. The FeO_x coating is a known OER catalyst in aqueous systems.[3] We are therefore interested to examine whether they serve to decompose Li_2O_2 in nonaqueous electrolytes. As will be discussed next (also see Figure 5.3b), the OER activity of FeO_x in DME is indeed obvious. As such, their uniform presence on the carbon surface ensures complete decomposition of Li_2O_2 at relatively low overpotentials (Figure 5.3a, lower panel). To compensate for the loss of ORR activity, we resolve to grow Pd nanoparticles, one of the best-known ORR catalysts in both aqueous and nonaqueous electrolytes (Figure 5.2a),[20, 33] by ALD after the deposition of FeO_x. The success in growing uniform Pd nanoparticles within 3DOm carbon pores is confirmed by TEM in Figure 5.2c (far right panel).

The efficacy of the above-outlined material design and preparation strategy is obvious. We see in Figure 5.3b that the average discharge potential measured on bare 3DOm carbon was 2.76 V (vs Li^+/Li), representing an overpotential of 0.20 V. The overpotential increased to 0.26 V when carbon was covered by FeO_x, but dropped back to 0.23 V with Pd decorations. Similarly, bare 3DOm carbon exhibited high recharge overpotentials (0.82 V). Adding Pd led to a reduction to 0.68 V because Pd is a moderately effective OER catalyst as well. The presence of FeO_x enabled the greatest overpotential reduction, with or without Pd (0.48 V and 0.51 V, respectively). The result strongly supports that OER were primarily catalyzed by FeO_x but not Pd, a desired feature of the material design principle as shown in Figure 5.3a.

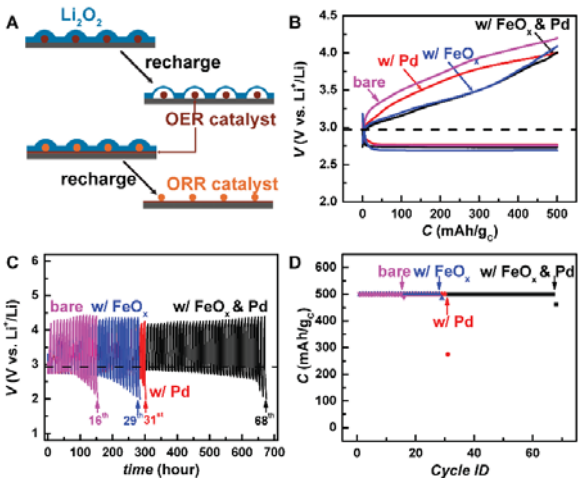

(**Figure 5.3** Effect of FeO_x and Pd decoration on 3DOm carbon. A. Without FeO_x, carbon inherently promotes ORR, producing Li_2O_2 far away from OER sites that are difficult to decompose. FeO_x coating serves as OER catalyst. When combined with ORR catalysts such as Pd, the decomposition of Li_2O_2 can be more complete. B. The understanding as shown in (A) is supported by the 1st cycle discharge/recharge characteristics. (Current density: $100mA/g_C$) C & D. More

complete decomposition of Li_2O_2 corresponds to better cyclability in the deep discharge/recharge cycles.)

The most important goal we hope to meet by adding FeO_x and Pd is to increase cyclabilities of Li-O_2 battery operations, because better controls over Li_2O_2 formation and decomposition are expected to correspond to better cyclability. To evaluate the cathode performance and in accordance with practices most commonly reported in the literature, we limited the capacity at 500 mAh/g and recorded the voltage-capacity behaviors as shown in Figure 5.3c. When the discharge potential dropped below 2.0 V, we considered the cell to have failed. It is seen in Figure 5.3c & 5.3d that bare 35nm 3DOm carbon cathode failed after the 16th cycle; addition of Pd improved the cyclability to the 31st cycle, presumably through the OER properties of Pd; the presence of FeO_x significantly stabilized the cathode, and the cell did not fail until the 68th cycle, which is the highest cycling numbers obtained on carbon-based cathode support in DME-based electrolyte, to the best of our knowledge. Because the decomposition of all known and tested electrolyte systems is a recognized issue, the eventual degradation of the cell performance is expected. Within this context, we are excited to see that the lifetime of a carbon cathode is extended by more than 4-fold by a simple FeO_x coating and Pd decoration.

Our next task is to confirm that the measured performance indeed represents the formation and decomposition of Li_2O_2. . First, X-ray diffraction (XRD, Figure 5.4a) unambiguously confirmed the formation of Li_2O_2 upon discharge. The peaks at 32.9°, 35.0° and 40.7° agreed well with documented diffraction peaks of Li_2O_2 (JCPDS 74-0115). Notably, no peaks corresponding to Li_2CO_3, an important undesired by-product of Li-O_2 operation, were found in the XRD pattern. Upon recharge, the Li_2O_2 diffraction peaks disappeared. Significantly, at the 61st cycles, the

diffraction peaks of Li_2O_2 were still prominent while no Li_2CO_3 peaks were observed. Next, X-ray photoelectron spectroscopy (XPS) was used to confirm the existence of Li_2O_2 from O 1s spectra. Before discharge, only species corresponding to iron oxide were identified: the peak located at 529.9 eV is attributed to O^{2-} in the lattice of Fe_2O_3 and the peak at 531.7eV to surface hydroxide terminal groups on Fe_2O_3. A third, much less prominent broad peak at 534.2 eV was assigned to Pd $3p_{3/2}$ of oxides on Pd nanoparticle surfaces. After discharge, three distinct peaks were obtained. Among them, the peak at 529.9 eV (from iron oxide) remained unchanged. At 531.9 eV was a new, most significant peak corresponding to Li_2O_2. The peak at 533.4 eV increased in intensity. It can be assigned to O in Li_2CO_3 due to the short exposure of sample to the ambient air before loading into the XPS instrument. Upon recharge, the spectrum was nearly identical to before discharge.

Third, differential electrochemical mass spectrometry (DEMS) was used to quantify the gaseous recharge product. For this set of experiments, tetraethylene glycol dimethyl ether (TEGDME) was chosen as the electrolyte solvent for its relatively low vapor pressures. During the 1st cycle recharge, O_2 accounted for 96.6% of the total gas evolved. Despite the protection, CO_2 was detected (3.4% of the total amount). It is noted that O_2 diffusion coefficient in TEGDME (2.17×10^{-6} cm^2/s) is lower than in dimethoxyethane (DME; 1.22×10^{-5} cm^2/s),[34] which was the primary solvent used for all characterizations other than DEMS. Consequently, the average recharge potentials in TEGDME (3.69 V) was greater than in DME (3.44 V). We therefore expect more severe side reactions when TEGDME is used. The Li_2O_2 formation and decomposition on protected 3DOm carbon electrode was also visualized by SEM (Figure 5.14). It is noted that the morphology and sizes of Li_2O_2 as reported in the literature vary depending on the cathode materials and the detailed discharge conditions. For instance, recent studies reported the formation of toroid Li_2O_2 in water contaminated ether electrolytes and other electrolytes with high donor numbers.[35, 36] In the present

study, toroid was not observed in 3DOm carbon electrode (see supporting information for test conditions and cell design in Figure 5.17).

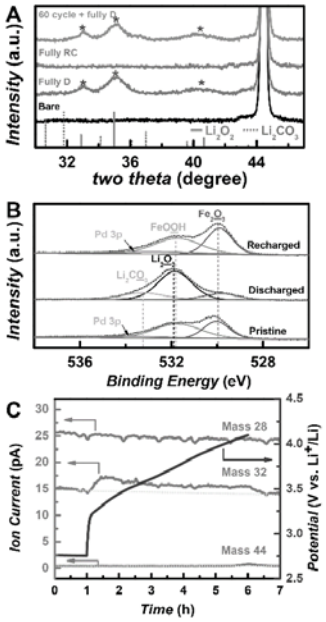

(**Figure 5.4** Product detection. A. X-ray diffraction peaks before discharge (black), after the 1st cycle discharge (green), the 1st cycle recharge (red), and fully discharged after 60 cycles of operations (purple). B. X-ray photoelectron spectra before discharge (bottom), after discharge (middle), and after recharge (top). The assignment of deconvoluted peaks are color-coded and labelled in the viewgraph, with the element of interest underlined (e.g., O peaks in Li_2O_2 labelled as $Li_2\underline{O}_2$). C. Mass-spectrometry detection of N_2 as a control (mass 28), O_2 (mass 32), and CO_2 (mass 44). The corresponding voltages were plotted against the right axis.)

5.3 Supplementary Information

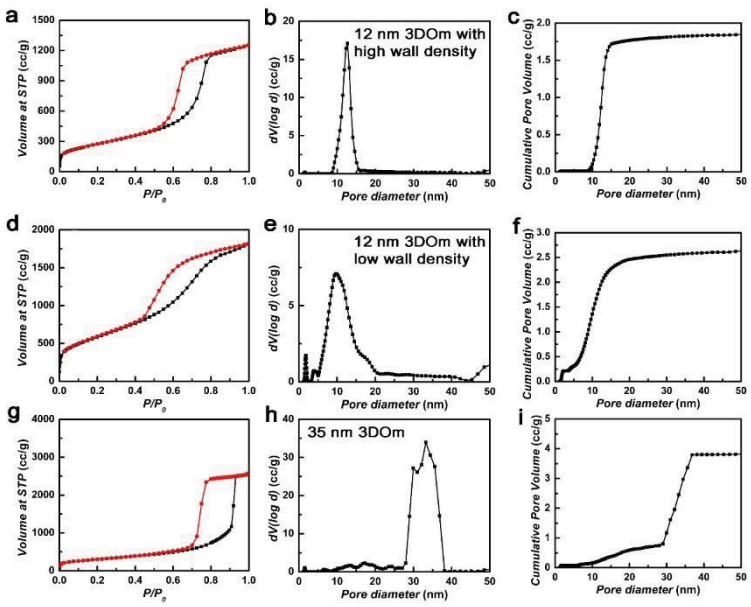

(**Figure 5.5** N_2 sorption isotherm, pore size distribution, and cumulative pore volume of as-prepared 12nm 3DOm carbon with high wall density (a, b, c), 12nm 3Dom carbon with low wall density (d, e, f) and 35nm 3DOm carbon (g, h, i).)

The N_2 adsorption/desorption experiments were carried out on an automatic gas sorption analyzer (Autosorb iQ, Quantachrome) at 77 K. Prior to the measurement, the samples were degassed at 25 °C for 24 h in vacuum. The pore size distribution and cumulative pore volume were obtained by applying a built-in QSDFT (quenched state density functional theory) adsorption model with cylindrical/spherical configuration for carbon (ASiQwin v3.0, Quantachrome).

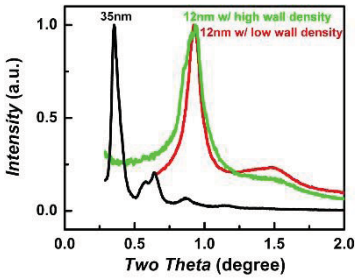

(**Figure 5.6** Small angle X-ray diffraction of the 3DOm carbon samples used in the study.)

XRD patterns at small angle were collected on a pinhole small-angle X-ray scattering system (S-Max3000, Rigaku) using monochromatic Cu Kα radiation with a diameter of ~0.4 mm. The SAXS intensity was measured by a two-dimensional gas filled wire array detector at a distance of ~1.5 m from the sample.

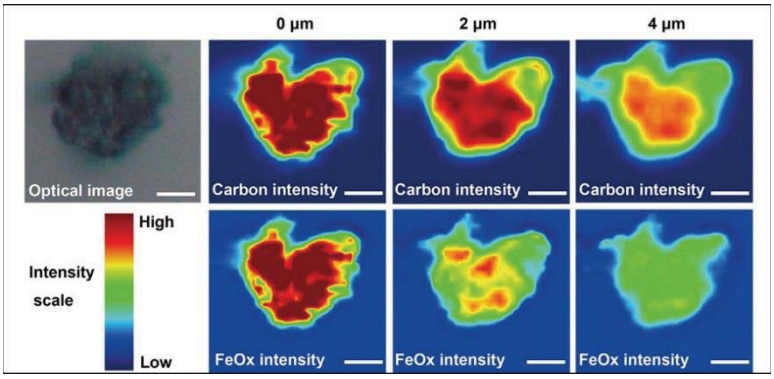

(**Figure 5.7** Raman mapping of FeO_x coated 3DOm carbon. Top left: optical image of the carbon particle studied. Top right panels: carbon signal mapping at 0, 2.0 µm, and 4.0 µm focal depth, respectively; bottom right panels: FeO_x signal mapping at the same depths. Scale bars: 5 µm.)

The uniformity of FeO_x within 3DOm carbon is also confirmed by Raman mapping. The existence and distribution of FeO_x can be visualized by Raman mapping, in which one can use one or multiple signature Raman shift peaks to observe how FeO_x is distributed. As shown in Figure 5.7, the Raman maps of FeO_x at different focal depths track those of carbon.

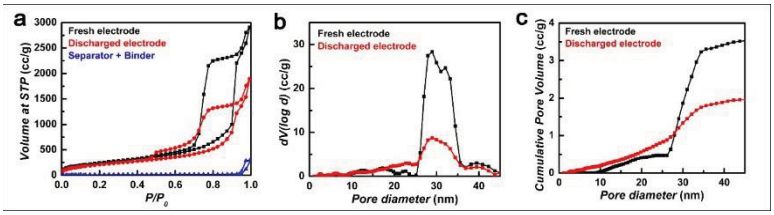

(**Figure 5.8** pore size distribution of fresh and discharged 35nm 3DOm carbon electrode.)

For a fully discharged 35nm 3DOm carbon electrode, not all pores would be occupied. Specifically, the pores on the surface would be filled up at a faster rate than pores deep underneath the electrode/electrolyte interface (see calculation in figure 5.16). This is because oxygen concentration on the top is the highest and will produce Li_2O_2 at a faster rate. We indeed see from Figure 5.8 that the pore size distribution is broadened upon discharge.

	Total pore volume [a] (cc/g)	surface area [a] (m^2/g)	Micropore volume [b] (cc/g)
12 nm 3DOm carbon with high wall density	1.85	901	0.012
12 nm 3DOm carbon with low wall density	2.64	1902	0.19
35 nm 3DOm carbon	3.82	1028	0.078
Fresh electrode	3.76	809	~0
Discharged electrode	2.17	657	~0
35 nm 3DOm carbon with 50 cycle ALD FeO_x	3.94	1045	0.071

(**Table 5.1** Textural data from N_2 sorption measurement for the carbons and electrodes.)

[a] From QSDFT model

[b] From the cumulative pore volume calculated from the QSDFT analysis when the pore size is smaller than 2 nm.

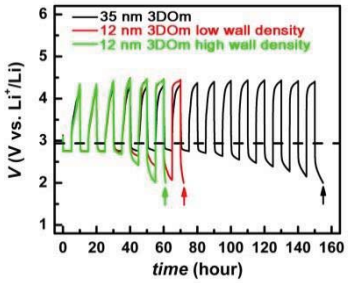

(**Figure 5.9** full data set of cycle performance of bare 12nm, 20nm and 35nm 3DOm carbon.)

Full data set of cycle performance of 12nm, 20nm and 35nm 3DOm carbon electrode. The discharge and recharge overpotentials for all three types of samples increased with increasing cycle numbers, indicating byproduct building up during cycling. The cut off potential for discharging was set at 2.0V vs. Li^+/Li. Cycling was stopped when a cell failed to deliver the 500mAh/g_c set point.

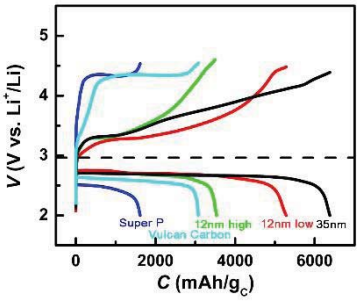

(**Figure 5.10** First cycle performance of Super P carbon, Vulcan carbon and 3DOm carbon. Tests were performed at 200mA/g_c.)

The specific capacity of pristine 35nm 3DOm carbon electrode reaches more than 6000mAh/g_c.

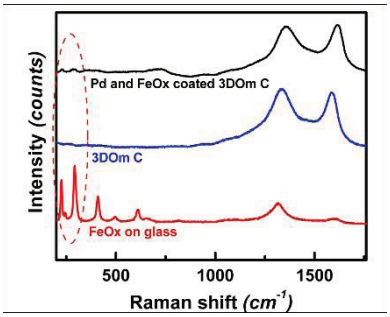

(**Figure 5.11** Raman characterization of Pd and FeO_x modified 3DOm carbon electrode.)

Raman characterization was carried out to confirm the coating uniformity of FeO_x. According to control experiment on glass (red trace in figure 5.11), FeO_x gave a series of characteristic peaks at low Raman shift region. Such characteristic peaks also existed at different depths of FeO_x coated electrodes, indicating the ALD growth of FeO_x was able to penetrate into the pores to produce coatings of high uniformity.

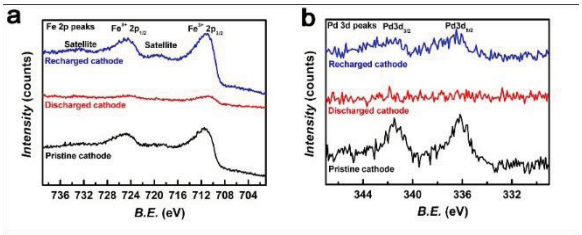

(**Figure 5.12** XPS characterization of (a) Fe 2p peaks and (b) Pd 3d peaks of pristine, discharged and recharged cathodes respectively.)

For fresh FeO_x and Pd modified electrodes, they showed characteristic Fe^{3+} $2p_{1/2}$ and Fe^{3+} $2p_{3/2}$ peaks. The peaks were diminished after discharging, which possibly due to a high Li_2O_2 coverage on top of FeO_x. After recharging, both peaks restored. Similar phenomena were also observed for Pd $3d_{3/2}$ and Pd $3d_{5/2}$ peaks.

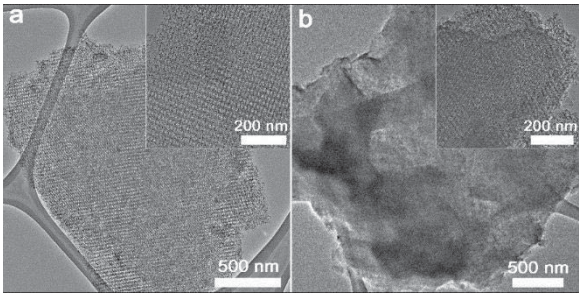

(**Figure 5.13** TEM characterizations of (a) pristine Pd/FeO_x modified 35nm 3DOm carbon and (b) fully discharged Pd/FeO_x modified 35nm 3DOm carbon samples.)

The ordered porous carbon networks were still distinct after FeO_x and Pd decoration (before discharge). After discharge, the mesopores within each micrometers size carbon particles were filled with Li_2O_2. Most products formed inside the pores as shown in the inset of Figure 5.13b. Few large particles were observed outside the pores.

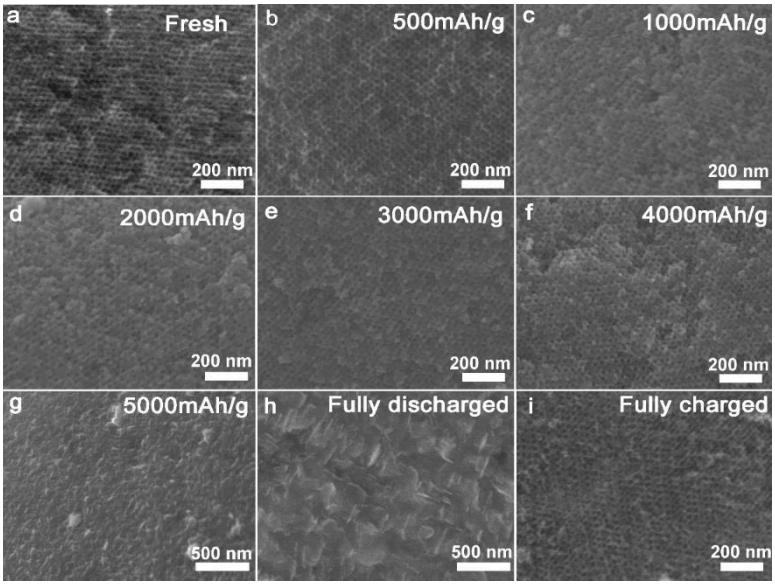

(**Figure 5.14** Scanning electron micrographs of 3DOm carbon surfaces at different stage of discharge and recharge.)

To directly observe the product morphology and distribution, we employed SEM to characterize 3DOm carbon at different stages of discharge/recharge. As is seen in Figure 5.14, the porous nature of the surfaces remained intact up to 4000 mAh/g, >67% of the full state of discharge (SOD, ca. 6000 mAh/g). The evidence strongly supports that majority of the Li_2O_2 products deposit within the large pores of 3DOm carbon. The growth of Li_2O_2 within the pores of 3DOm carbon was also confirmed by TEM characterizations (Figure 5.13). As the Li_2O_2 particle sizes are not expected to exceed the dimensions of the hosting pores, for the first time we obtained complete control over the site and size of Li_2O_2 growth in Li-O_2 operations. The relatively small pore sizes are considered advantageous because they minimize impact of electronic and ionic polarizations within Li_2O_2 on the discharge/recharge overpotentials.[37, 38] Toward the end of discharge, starting at 5000 mAh/g, we started to observe particulate Li_2O_2 appearance on the exterior of 3DOm carbon (Figure 5.14g). Presumably due to the uniform distributions of ORR catalysts (Pd nanoparticles) on 3DOm carbon,

only small (<500 nm) plates of Li_2O_2 were observed. The porous surface of 3DOm was fully exposed with no visible residues upon recharge (Figure 5.14i).

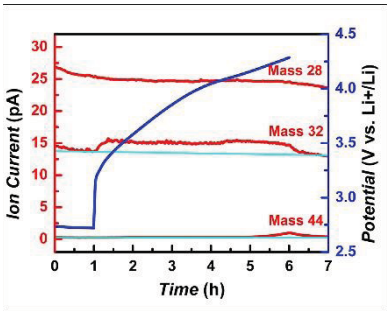

(**Figure 5.15** DEMS result of 1st charge cycle of pristine 35nm 3DOm carbon electrode.)

DEMS result of 1st charge cycle of pristine 35nm 3DOm carbon electrode in TEGDME electrolyte. It supports that CO_2 only evolves at the end of the charging cycle when potential is high (>4.0 V). The generation of CO_2 in this case may come from two sources: (a) the decomposition of TEGDME electrolyte; (b) carbon corrosion.

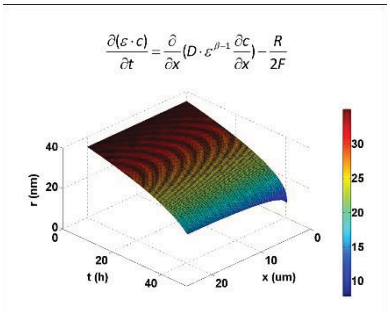

(**Figure 5.16** Pore size distribution at different depths and discharge times.)

Calculations of pore filling by Li_2O_2 within a 35nm 3DOm electrode based on an oxygen diffusion model was performed. The calculations were based on the following assumptions. First, the

deposition rate of Li_2O_2 is first order to O_2 concentration. Second, the diffusion of O_2 follows the Fick's law. Third, O_2 is saturated in the electrolyte at the beginning of the discharge reactions. Fourth, the only source of O_2 supply comes from the electrolyte/gas surface.

We see from Figure 5.16 that the Li_2O_2 distribution becomes less uniform (more Li_2O_2 close to the electrode/electrolyte interface) at a deeper level of DOD. The reason is that O_2 concentration is higher at locations closer to the electrolyte/gas interfaces. At the end of the discharge, the surface pores are completely filled by Li_2O_2. At the stage, no additional O_2 will be supplied, and discharge overpotential will increase sharply. Pores far away from the electrode/electrolyte interface are not yet filled, leading to broadening of pore size distribution by BET measurements.

Our calculations further reveal that the pore filling percentage (which directly corresponds to achievable capacities) also depends on: (1) the type of electrolyte (through influencing O_2 diffusion coefficient and solubility); (2) loading density of carbon materials (through changing the overall normalized specific capacities); (3) discharge current densities (by dictating reaction kinetics).

Simulation based on oxygen diffusion model: Pore filling by discharge product during discharging was simulated based on a simplified oxygen diffusion model using MATLAB. Briefly, we assume (1) The diffusion of O_2 follows Fick's law with porosity consideration.[39]

$$\frac{\partial(\varepsilon \cdot c)}{\partial t} = \frac{\partial}{\partial x}(D \cdot \varepsilon^{\beta-1} \frac{\partial c}{\partial x}) - \frac{R}{2F} \quad (1)$$

(2) The reaction rate is first order proportional to (a) oxygen concentration and (b) electrode/electrolyte interface area.

$$R(x,t) \propto c(x,t) \cdot s(x,t) \quad (2)$$

$$\int_0^L R(x,t)dx = j \tag{3}$$

$$s(x,t) \propto (\frac{\varepsilon}{\varepsilon_0})^{2/3} \tag{4}$$

(3) The reaction product (Li_2O_2) form a thin film to coat the inner pores and cause the local porosity to decrease.

$$\frac{\partial \varepsilon(x,t)}{\partial t} = -\frac{R(x,t)}{2F} \cdot \frac{M}{\rho} \tag{5}$$

$$\varepsilon(x,0) = \varepsilon_0 \tag{6}$$

(4) At the oxygen/electrolyte interface, the oxygen concentration in the electrolyte always equals to saturation concentration due to fast dissolution. At the electrode/separator interface, oxygen does not pass the boundary.

$$c(x,0) = c_0 \tag{7}$$

$$c(0,t) = c_0 \tag{8}$$

$$\frac{dc(L,t)}{dx} = 0 \tag{9}$$

Symbols	Meaning	Value	Unit
ε	Local porosity of carbon		
c	Local oxygen concentration		mol/cm^3
t	Elapsed time since discharging started		s
x	Distance from oxygen/electrode interface		cm

D	Diffusion coefficient of oxygen in the electrolyte[34]	1.22×10^{-5}	cm^2/s
β	Bruggeman coefficients	3	
R	Oxygen consumption rate per unit distance		A
F	Faraday constant	96485	As/mol
S	Surface area		cm^2
L	The overall thickness of carbon electrode		cm
j	Cell discharge current		A
ε_0	Initial porosity	0.74	
M	Molar mass of Li_2O_2	46	g/mol
ρ	Density of Li_2O_2	2.3	g/cm^3
c_0	Maximum oxygen solubility in the electrolyte[40]	9.57×10^{-6}	mol/cm^3

(**Table 5.2** Definition of all symbols.)

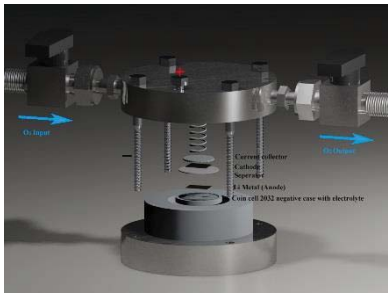

(**Figure 5.17** A Swagelok™ cell design.)

The design of our cell was modified from literature reports.[41]

5.4 Conclusions

Before the full potentials of Li-O_2 can be materialized, significant advances in many areas, including the discovery of stable electrolytes and anodes, are necessary. Among them, controls over the product (Li_2O_2 in the case of Li-O_2 battery) formation and decomposition are critical. Availability of material platforms that can enable detailed studies of the processes will contribute significantly to this field. Within this context, 3DOm carbon offers unprecedented opportunities. The demonstrated high capacity and preferred deposition within the large pores of 3DOm carbon build a foundation for high performance Li-O_2 battery operations. A facile FeO_x ALD growth, in conjunction with ORR catalyst decorations of ligand-free Pd nanoparticles, readily addresses the inherent reactivity of carbon and extends the cyclability from 16 to 68. Importantly, the 3DOm carbon platform allows for control over the size and location of Li_2O_2 deposition. We anticipate 3DOm carbon to play an increasingly more important role in the field energy storage.

5.5 References

(1) Yokoi, T.; Sakamoto, Y.; Terasaki, O.; Kubota, Y.; Okubo, T.; Tatsumi, T. Periodic Arrangement of Silica Nanospheres Assisted by Amino Acids. *J. Am. Chem. Soc.* **2006**, *128*, 13664-13665.

(2) Younesi, R.; Hahlin, M.; Bjorefors, F.; Johansson, P.; Edstrom, K. Li-O_2 Battery Degradation by Lithium Peroxide (Li_2O_2): A Model Study. *Chem. Mater.* **2013**, *25*, 77-84.

(3) Lin, Y.; Zhou, S.; Sheehan, S. W.; Wang, D. Nanonet-Based Hematite Heteronanostructures for Efficient Solar Water Splitting. *J. Am. Chem. Soc.* **2011**, *133*, 2398-2401.

(4) Lin, Y.; Xu, Y.; Mayer, M. T.; Simpson, Z. I.; McMahon, G.; Zhou, S.; Wang, D. Growth of P-Type Hematite by Atomic Layer Deposition and Its Utilization for Improved Solar Water Splitting. *J. Am. Chem. Soc.* **2012**, *134*, 5508-5511.

(5) Du, C.; Yang, X.; Mayer, M. T.; Hoyt, H.; Xie, J.; McMahon, G.; Bischoping, G.; Wang, D. Hematite-Based Water Splitting with Low Turn-On Voltages. *Angew. Chem. Int. Ed.* **2013**, *52*, 12692-12695.

(6) Abraham, K. M.; Jiang, Z. A Polymer Electrolyte-Based Rechargeable Lithium/Oxygen Battery. *J. Electrochem. Soc.* **1996**, *143*, 1-5.

(7) Hartmann, P.; Bender, C. L.; Vracar, M.; Duerr, A. K.; Garsuch, A.; Janek, J.; Adelhelm, P. A Rechargeable Room-Temperature Sodium Superoxide (NaO_2) Battery. *Nature Mater.* **2013**, *12*, 228-232.

(8) Ren, X.; Wu, Y. A Low-Overpotential Potassium-Oxygen Battery Based on Potassium Superoxide. *J. Am. Chem. Soc.* **2013**, *135*, 2923-2926.

(9) Li, Y.; Dai, H. Recent Advances in Zinc-Air Batteries. *Chem. Soc. Rev.* **2014**, *43*, 5257-5275.

(10) McCloskey, B. D.; Bethune, D. S.; Shelby, R. M.; Girishkumar, G.; Luntz, A. C. Solvents' Critical Role in Nonaqueous Lithium-Oxygen Battery Electrochemistry. *J. Phys. Chem. Lett.* **2011**, *2*, 1161-1166.

(11) Lu, Y. C.; Gallant, B. M.; Kwabi, D. G.; Harding, J. R.; Mitchell, R. R.; Whittingham, M. S.; Shao-Horn, Y. Lithium-Oxygen Batteries: Bridging Mechanistic Understanding and Battery Performance. *Energy Environ. Sci.* **2013**, *6*, 750-768.

(12) McCloskey, B. D.; Speidel, A.; Scheffler, R.; Miller, D. C.; Viswanathan, V.; Hummelshoej, J. S.; Noerskov, J. K.; Luntz, A. C. Twin Problems of Interfacial Carbonate Formation in Nonaqueous Li-O_2 Batteries. *J. Phys. Chem. Lett.* **2012**, *3*, 997-1001.

(13) McCloskey, B. D.; Bethune, D. S.; Shelby, R. M.; Mori, T.; Scheffler, R.; Speidel, A.; Sherwood, M.; Luntz, A. C. Limitations in Rechargeability of Li-O_2 Batteries and Possible Origins. *J. Phys. Chem. Lett.* **2012**, *3*, 3043-3047.

(14) Ottakam Thotiyl, M. M.; Freunberger, S. A.; Peng, Z.; Bruce, P. G. The Carbon Electrode in Nonaqueous Li-O_2 Cells. *J. Am. Chem. Soc.* **2013**, *135*, 494-500.

(15) Gallant, B. M.; Kwabi, D. G.; Mitchell, R. R.; Zhou, J.; Thompson, C. V.; Shao-Horn, Y. Influence of Li_2O_2 Morphology on Oxygen Reduction and Evolution Kinetics in Li-O_2 Batteries. *Energy Environ. Sci.* **2013**, *6*, 2518-2528.

(16) Xu, J. J.; Wang, Z. L.; Xu, D.; Zhang, L. L.; Zhang, X. B. Tailoring Deposition and Morphology of Discharge Products Towards High-Rate and Long-Life Lithium-Oxygen Batteries. *Nat. Commun.* **2013**, *4*, 2438.

(17) Yilmaz, E.; Yogi, C.; Yamanaka, K.; Ohta, T.; Byon, H. R. Promoting Formation of Noncrystalline Li_2O_2 in the Li-O_2 Battery with RuO_2 Nanoparticles. *Nano Lett.* **2013**, *13*, 4679-4684.

(18) Adams, B. D.; Radtke, C.; Black, R.; Trudeau, M. L.; Zaghib, K.; Nazar, L. F. Current Density Dependence of Peroxide Formation in the Li-O_2 Battery and Its Effect on Charge. *Energy Environ. Sci.* **2013**, *6*, 1772-1778.

(19) Peng, Z.; Freunberger, S. A.; Chen, Y.; Bruce, P. G. A Reversible and Higher-Rate Li-O_2 Battery. *Science* **2012**, *337*, 563-566.

(20) Lu, J.; Lei, Y.; Lau, K. C.; Luo, X. Y.; Du, P.; Wen, J. G.; Assary, R. S.; Das, U.; Miller, D. J.; Elam, J. W.; Albishri, H. M.; Abd El-Hady, D.; Sun, Y. K.; Curtiss, L. A.; Amine, K. A Nanostructured Cathode Architecture for Low Charge Overpotential in Lithium-Oxygen Batteries. *Nat. Commun.* **2013**, *4*, 2383.

(21) Xie, J.; Yao, X.; Madden, I. P.; Jiang, D.-E.; Chou, L.-Y.; Tsung, C.-K.; Wang, D. Selective Deposition of Ru Nanoparticles on $TiSi_2$ Nanonet and Its Utilization for Li_2O_2 Formation and Decomposition. *J. Am. Chem. Soc.* **2014**, *136*, 8903-8906.

(22) Kang, S. J.; Mori, T.; Narizuka, S.; Wilcke, W.; Kim, H.-C. Deactivation of Carbon Electrode for Elimination of Carbon Dioxide Evolution from Rechargeable Lithium-Oxygen Cells. *Nat. Commun.* **2014**, *5*, 3937.

(23) Fan, W.; Snyder, M. A.; Kumar, S.; Lee, P.-S.; Yoo, W. C.; McCormick, A. V.; Lee Penn, R.; Stein, A.; Tsapatsis, M. Hierarchical Nanofabrication of Microporous Crystals with Ordered Mesoporosity. *Nature Mater.* **2008**, *7*, 984-991.

(24) Cychosz, K. A.; Guo, X.; Fan, W.; Cimino, R.; Gor, G. Y.; Tsapatsis, M.; Neimark, A. V.; Thommes, M. Characterization of the Pore Structure of Three-Dimensionally Ordered Mesoporous Carbons Using High Resolution Gas Sorption. *Langmuir* **2012**, *28*, 12647-12654.

(25) Guo, Z.; Zhou, D.; Dong, X.; Qiu, Z.; Wang, Y.; Xia, Y. Ordered Hierarchical Mesoporous/Macroporous Carbon: A High Performance Catalyst for Rechargeable Li-O_2 batteries. *Adv. Mater.* **2013**, *25*, 5668-5672.

(26) Ding, N.; Chien, S. W.; Hor, T. S. A.; Lum, R.; Zong, Y.; Liu, Z. Influence of Carbon Pore Size on the Discharge Capacity of Li-O_2 Batteries. *J. Mater. Chem. A* **2014**, *2*, 12433-12441.

(27) Jian, Z.; Liu, P.; Li, F.; He, P.; Guo, X.; Chen, M.; Zhou, H. Core-Shell-Structured CNT@RuO_2 Composite as a High-Performance Cathode Catalyst for Rechargeable Li-O_2 Batteries. *Angew. Chem. Int. Ed.* **2014**, *53*, 442-446.

(28) Sun, B.; Huang, X.; Chen, S.; Munroe, P.; Wang, G. Porous Graphene Nanoarchitectures: An Efficient Catalyst for Low Charge-Overpotential, Long Life, and High Capacity Lithium-Oxygen Batteries. *Nano Lett.* **2014**, *14*, 3145-3152.

(29) Itkis, D. M.; Semenenko, D. A.; Kataev, E. Y.; Belova, A. I.; Neudachina, V. S.; Sirotina, A. P.; Havecker, M.; Teschner, D.; Knop-Gericke, A.; Dudin, P.; Barinov, A.; Goodilin, E. A.; Shao-Horn, Y.; Yashina, L. V. Reactivity of Carbon in Lithium-Oxygen Battery Positive Electrodes. *Nano Lett.* **2013**, *13*, 4697-4701.

(30) McCloskey, B. D.; Valery, A.; Luntz, A. C.; Gowda, S. R.; Wallraff, G. M.; Garcia, J. M.; Mori, T.; Krupp, L. E. Combining Accurate O_2 and Li_2O_2 Assays to Separate Discharge and Charge Stability Limitations in Nonaqueous Li-O_2 Batteries. *J. Phys. Chem. Lett.* **2013**, *4*, 2989-2993.

(31) Ottakam Thotiyl, M. M.; Freunberger, S. A.; Peng, Z.; Chen, Y.; Liu, Z.; Bruce, P. G. A Stable Cathode for the Aprotic Li-O_2 Battery. *Nature Mater.* **2013**, *12*, 1050-1056.

(32) Black, R.; Lee, J.-H.; Adams, B.; Mims, C. A.; Nazar, L. F. The Role of Catalysts and Peroxide Oxidation in Lithium-Oxygen Batteries. *Angew. Chem. Int. Ed.* **2013**, *52*, 392-396.

(33) Lu, Y.-C.; Gasteiger, H. A.; Shao-Horn, Y. Catalytic Activity Trends of Oxygen Reduction Reaction for Nonaqueous Li-Air Batteries. *J. Am. Chem. Soc.* **2011**, *133*, 19048-19051.

(34) Laoire, C. O.; Mukerjee, S.; Abraham, K. M.; Plichta, E. J.; Hendrickson, M. A. Influence of Nonaqueous Solvents on the Electrochemistry of Oxygen in the Rechargeable Lithium-Air Battery. *J. Phys. Chem. C* **2010**, *114*, 9178-9186.

(35) Johnson, L.; Li, C.; Liu, Z.; Chen, Y.; Freunberger, S. A.; Ashok, P. C.; Praveen, B. B.; Dholakia, K.; Tarascon, J.-M.; Bruce, P. G. The Role of LiO_2 Solubility in O_2 Reduction in Aprotic Solvents and Its Consequences for Li-O_2 Batteries. *Nature Chem.* **2014**, *6*, 1091-1099.

(36) Aetukuri, N. B.; McCloskey, B. D.; Garcia, J. M.; Krupp, L. E.; Viswanathan, V.; Luntz, A. C. Solvating Additives Drive Solution-Mediated Electrochemistry and Enhance Toroid Growth in Non-Aqueous Li-O_2 Batteries. *Nature Chem.* **2015**, *7*, 50-56.

(37) Gerbig, O.; Merkle, R.; Maier, J. Electron and Ion Transport in Li_2O_2. *Adv. Mater.* **2013**, *25*, 3129-3133.

(38) Geng, W. T.; He, B. L.; Ohno, T. Grain Boundary Induced Conductivity in Li_2O_2. *J. Phys. Chem. C* **2013**, *117*, 25222-25228.

(39) Andrei, P.; Zheng, J. P.; Hendrickson, M.; Plichta, E. J. Some Possible Approaches for Improving the Energy Density of Li-Air Batteries. *J. Electrochem. Soc.* **2010**, *157*, A1287-A1295.

(40) Read, J.; Mutolo, K.; Ervin, M.; Behl, W.; Wolfenstine, J.; Driedger, A.; Foster, D. Oxygen Transport Properties of Organic Electrolytes and Performance of Lithium/Oxygen Battery. *J. Electrochem. Soc.* **2003**, *150*, A1351-A1356.

(41) Lu, Y.-C.; Gasteiger, H. A.; Parent, M. C.; Chiloyan, V.; Shao-Horn, Y. The Influence of Catalysts on Discharge and Charge Voltages of Rechargeable Li-Oxygen Batteries. *Electrochem. Solid-State Lett.* **2010**, *13*, A69-A72.